รายงานวิจัยฉบับสมบูรณ์

โครงการผลของโลหะทรานซิชันที่แตกต่างกันกับสมบัติเชิงอิเล็กทรอนิกส์และสมบัติเชิงกลของวัสดุกลุ่มโลหะทรานซิชันเตตระโบไรด์ภายใต้ความดันสูง

โดย ดร. คมศิลป์ โคตมูล

วันที่ 30 เมษายน พ.ศ. 2563

สัญญาเลขที่ TRG6080014

รายงานวิจัยฉบับสมบูรณ์

โครงการผลของโลหะทรานซิชันที่แตกต่างกันกับสมบัติเชิงอิเล็กทรอนิกส์และสมบัติเชิงกลของวัสดุกลุ่มโลหะทรานซิชันเตตระโบไรด์ภายใต้ความดันสูง

คมศิลป์ โคตมูล
โรงเรียนมหิดลวิทยานุสรณ์

สนับสนุนโดยสำนักงานกองทุนสนับสนุนการวิจัยและต้นสังกัด
(ความเห็นในรายงานนี้เป็นของผู้วิจัย
สกว.และต้นสังกัดไม่จำเป็นต้องเห็นด้วยเสมอไป)

บทคัดย่อ

รหัสโครงการ : TRG6080014

ชื่อโครงการ : ผลของโลหะทรานซิชันที่แตกต่างกันกับสมบัติเชิงอิเล็กทรอนิกส์และสมบัติเชิงกลของวัสดุกลุ่มโลหะทรานซิชันเตตระโบไรด์ภายใต้ความดันสูง

ชื่อนักวิจัย : ดร. คมศิลป์ โคตมูล โรงเรียนมหิดลวิทยานุสรณ์

ที่อยู่อีเมลล์ : komsilpkotmool@gmail.com, komsilp.ko@kmitl.ac.th

ระยะเวลาโครงการ : 2 ปี

ในโครงการวิจัยนี้ ได้ใช้ทฤษฎีความหนาแน่นเชิงฟังก์ชัน (Density fucntional theory, DFT) และระเบียบวิธีทางวิวัฒนาการ (Evolutionary algorithms) เพื่อพยากรณ์โครงสร้างของวัสดุกลุ่มโลหะโบไรด์ที่อยู่ภายใต้ความดันสูง พบว่า ในวัสดุ RuB_4 ได้พบโครงสร้างใหม่ภายใต้ความดันสูง ได้แก่ โครงสร้างผลึกแบบ *C2/c* และ *Immm* เสถียรที่ความดัน 198 – 388 GPa และสูงกว่า 388 GPa ตามลำดับ เมื่อเปรียบเทียบกับวัสดุ FeB_4 และ OsB_4 ซึ่งเป็นวัสดุที่มีโลหะหมู่เดียวกันและมีโครงสร้างภายใต้ความดันสูงเป็นสารกึ่งตัวนำ แต่ทั้งนี้ พบว่า โครงสร้างผลึกแบบ *C2/c* และ *Immm* ของวัสดุ RuB_4 มีสมบัติเป็นสารกึ่งโลหะและโลหะ ตามลำดับ ทำให้ลำดับการเปลี่ยนวัฏภาคเชิงโครงสร้างภายใต้ความดันสูงของ RuB_4 แตกต่างไปจากวัสดุ FeB_4 และ OsB_4 นอกจากนี้ ยังพบว่า ค่าความแข็งที่คำนวณตามโมเดลของ Chen ของวัสดุ RuB_4 ยังมีค่าน้อยกว่าความแข็งของวัสดุ FeB_4 และ OsB_4 อีกด้วย ความแข็งของโครงสร้างผลึกที่ความดันบรรยากาศของวัสดุ RuB_4 (*P6$_3$/mmc*) มีค่าประมาณ 18 GPa การคำนวน Electron localization function (ELF), Mulliken population analysis (MPA) และ projected crystal orbital Hamilton populations (pCOHP) เปิดเผยว่า ลักษณะการจัดเรียงตัวของอะตอมและความแข็งของพันธะโควาเลนซ์ ส่งผลโดยตรงกับความแข็งของวัสดุกลุ่มนี้ ผลที่ได้จากงานวิจัยนี้สามารถนำมาเป็นพื้นฐานสำคัญในการออกแบบวัสดุที่มีความแข็งพิเศษ (superhard materials) ในวัสดุกลุ่มโลหะโบไรด์ นอกจากวัสดุ RuB_4 แล้ว ยังได้พยากรณ์โครงสร้างผลึกของวัสดุ Li_2O_2 ที่ความดัน 75 GPa ได้พบโครงสร้างผลึกแบบใหม่ คือ $P2_1$ ที่แตกต่างเล็กน้อยจากโครงสร้างผลึกแบบเดิมที่เคย $P2_1/c$ ที่เคยเสนอมาในงานวิจัยก่อนหน้า ทั้งนี้ ได้ศึกษาและอธิบายอย่างละเอียดของการบิดเบี้ยวในโครงสร้างผลึกที่ความดันบรรยากาศ *P6$_3$/mmc* ของวัสดุ Li_2O_2 ซึ่งส่งผลโดยตรงต่อช่องว่างแถบพลังงาน (Ennergy gap) ค่าสัดส่วน c/a

คำหลัก : ความแข็ง; ความดันสูง; การเปลี่ยนวัฏภาค; วัสดุโลหะโบไรด์; ลิเทียมเปอร์ออกไซด์

Abstract

Project Code : TRG6080014

Project Title : Effects of transition metals on electronic and mechanical properties of transition- metal tetraborides under high pressure

Investigator : Komsilp Kotmool, Mahidol Wittayanusorn School

E-mail Address : komsilpkotmool@gmail.com, komsilp.ko@kmitl.ac.th

Project Period : 2 years

Employing a systematic first-principles investigation with crystal structure searching based on an evolutionary algorithm, the novel high-pressure phases of RuB_4 -- *C2/c* and *Immm* phases have been uncovered at 198 and 388 GPa, respectively. Interestingly, in comparison with FeB_4 and OsB_4, which have an analogous electronic and chemical structure with RuB_4, and have predicted high-pressure structures exhibiting a semiconducting phase, it is found that both the *C2/c* and *Immm* phases of RuB_4 are likely to be the metallic materials. The hardness of predicted phases of RuB_4 has also been calculated by using the empirical model of Chen. It is found that the hardness of ambient phase, $P6_3/mmc$, is about 18 GPa, which is relatively low comparing to those of FeB_4 and OsB_4. The nature of chemical bonding investigated by electron localization function (ELF), Mulliken population analysis (MPA) and projected crystal orbital Hamilton populations (pCOHP) calculations reveals that the atomic configurations and the degree of covalent bonding of the predicted phases are responsible for lower hardness compared to those of FeB_4 and OsB_4. The results of this work provide more understanding of the family of metal tetraboride for designing metal-boride based hard/superhard materials. For Li_2O_2, $P2_1$ structure, which is slightly different from the previous reported $P2_1/c$ structure, has been proposed. The distortion in the ambient phase ($P6_3/mmc$ structure) of Li_2O_2 reported in previous experiment has been investigated. The finding shows that the pressure dependences of band gap, c/a ratio, ELF and phonon dispersion reflect to the structural distortion.

Keywords : hardness; high pressure; phase transition; ruthenium tetraboride; lithium peroxide

1. Introduction to the research problem and its significance

Diamond is known as the hardest material which has bulk modulus (B_0) 443 GPa and Vickers hardness (H_v) 90 – 120 GPa [1]. It is well known that covalent bond of sp^3 hybridization between carbon atoms results of that hardest state. Therefore, not diamond is only used in gems and jewelry industry but it is also utilized in hard industries such as hard material coating, cutting and drilling tools, and other advanced optical technologies. Due to high demand of diamond use in recent year, the alternative hard/superhard materials are finding for this purpose.

Transition-metal boride compound (TM–B) is a kind of materials exhibiting a hard/superhard material ($H_v \geq 40$ GPa) [2] because of a degree of directional covalent bonding of three dimensional (3D) boron network. Both experimental and theoretical studies on TMB_2 และ TMB_4 revealed that these materials potentially are the hard or superhard materials with having high bulk modulus and hardness. For instance, OsB_2 has B_0 = 395 GPa and H_v = 37 GPa, [3-4] WB_4 has B_0 = 339 GPa and H_v = 43 GPa [5-6]. Notably, iron tetraboride (FeB_4) has been proposed its ambient pressure phase (e.g. Pnnm) exhibits a superhard superconducting material [7-8]. By using first-principles investigations, it has been revealed the high pressure phases, which belong the tetragonal structures with space groups of $I4_1/acd$ and $P4_2/nmc$ [9]. These two tetragonal phases cloud possess the semiconducting and hard/superhard materials. Recently, osmium tetraboride (OsB_4) has been presented the transitions sequence up to 300 GPa [10]. At 11 GPa, the $P4_2/nmc$ phase emerges in OsB_4 similarly corresponding to FeB_4 [9]. Those findings suggested both FeB_4 and OsB_4 process a metal-to-semiconductor phase transition. The semiconducting FeB_4 and OsB_4 phases combining of semiconductive and potential hard properties are contributed to be the strong directional covalent bondings of three-dimension (3D) boron network and the significant covalence of TM-B pairs. While theoretically compressing CrB_4 which starts by the identical Pnnm phase with FeB_4, but it did not encounter the high-pressure semiconducting phase [11]. It is important to remark that Fe and Os are in the same group of 8B element in periodic table that share the similar electronic configuration, as a result of the related transformation pathway under high pressure of FeB_4 and OsB4. However, still, there are some questions and controversies raised by previous investigations for the TM-B compounds. Those issues open to the gaps of research, for example; (i) CrB_4 has the same ambient phase with FeB_4 but why does it has different high-pressure pathways with FeB_4? And what is about the RuB_4? (ii) What are the

effects of number and energy level of *d* electrons of transition metals on the crystal structures and relating properties of TMB_4 under high pressure? Therefore, it can be addressed to require more investigations in this material family being still needed to fulfill and make deeper understandings.

This project aims at theoretically investigating in high-pressure behaviors of the TMB_4 by considering effects of different transition metals (i.e. Fe, Ru, and Os) on crystal structures, mechanical properties, electronic properties, and high-pressure phase transitions. It would be expectedly guiding the high-pressure behavior and revealing possible applications by this material family.

2. Objectives

1. To investigate the atomic mechanism of different transition metals in the TMB_4s (TM = Fe Ru and Os) which influences to their crystal structures, mechanical properties, electronic properties and structural phase transition under high pressure.

2. To calculate and evaluate the crystal structures, mechanical properties, electronic properties and structural phase transition under high pressure that may suggest to the further applications of the TMB_4s.

3. Methodology

This project mainly employed density functional theory (DFT) within some platforms consisting of VASP [12] and CASTEP [13] codes. The standard functional GGA-PBE [14] will be used to perform the most calculations in this project. Moreover, the hybrid functions such as HSE06 [15] was also implemented for calculating some appropriate properties, i.e., electronic band structure. Convergences of energy cutoff and k-point meshes and other input values was carefully used in the calculations to ensure and verify the accuracy of the computational results, as well as, the findings will be compared with the available experimental results. The more detail of methodology in this study is following;

1. Reviewing the literatures relating to the TMB_4 materials, to find the research gaps leading to the question of; what is the influences of different transition metals on crystal structure, high pressure phase transition, and relative properties of the TMB_4s?
2. Searching the crystal structures as a function of pressure of the novel TMB_4 materials using evolutionary algorithm, which is a searching method inspired

by biological evolution, for instance, randomness, mutation, selection, recombination, and reproduction. The candidates from searches are given from the optimization problem. The method performing in this project was based on USPEX code (Universal Structure Predictor: Evolutionary Xtalloraphy) [16] which is interfacing with VASP codes. To predict the crystal structures of a material under high pressure using evolutionary algorithm, only atomic recipe is an initial input of a process. Varying number of atoms is necessary to ensure that the obtained structure is the most stable or global structure at that pressure. The procedure of evolutionary algorithm is shown as Figure 1.

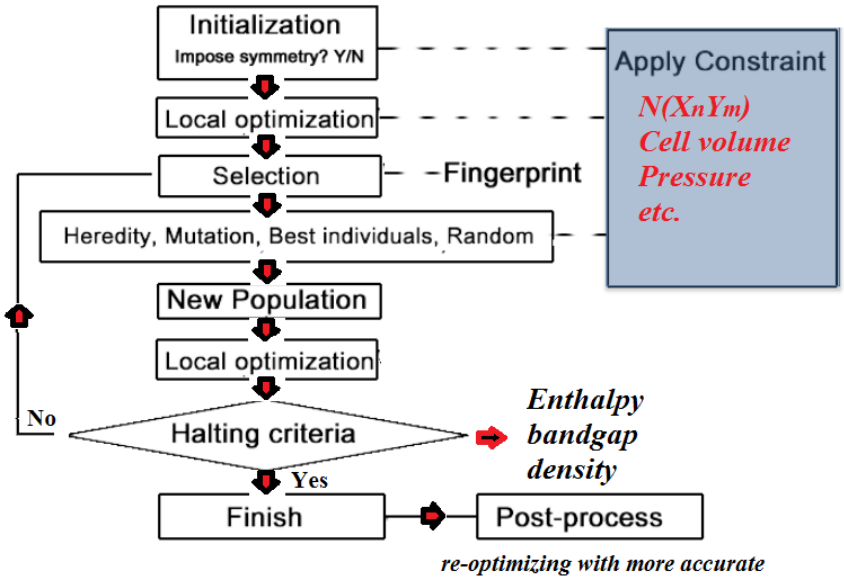

Figure 1: Flowchart of predicting crystal structure at certain condition by using evolutionary algorithm.

3. Calculating the stabilities of the crystal structures of the TMB_4s which consist of:

3.1 Thermodynamic stability: Gibbs free energy is a value verifying that which structure is the most stable one comparing to others under a certain condition (Pressure and Temperature). For standard DFT calculation, the environment is constrained at zero Kelvin, therefore, Gibbs free energy reduces to enthalpy by this condition. To evaluate the stability of a material at above zero temperature, the phonon spectral energies (from 3.4) can be directly added into the enthalpy

part, then, it will construct the Gibbs free energy at given temperature of the material.

3.2 Formation energy: it can confirm that whether a given crystal structure is preferable existence than forming alloy of TM and boron or not.

3.3 Elastic stability: by considering elastic stiffness tensors, they can interpret to the stability of a material under loading according to Born stability criteria [15].

3.4 Dynamic stability: phonon dispersion indicates to the stability of a material resulting of atomic vibration though symmetry paths. A negative phonon frequency of a predicted crystal structure of material insists the instability of that crystal structure. Moreover, phonon dispersion also brings to accounting temperature effect in materials.

4. Calculating/evaluating the applicable properties of the TMB_4s such as elastic property, Vickers hardness, electron-phonon coupling, etc.

Vickers hardness: is a kind of hardness defining how resistant a solid is to various kinds of shape deformations under applying external stresses. In experimental method, the Vickers hardness of a material is measured by using diamond indenter. In theoretical method, Vickers hardness can be accessible by various methods. However, a conventional one proposed by Chen *et al*, (*Intermetallics*, **19** (2011) 1275) [17] where the Vickers hardness can be calculated from bulk (B) and shear (G) modulus of a crystal structure ($H_v = 2(k^2G)^{0.585} - 3$, where k = G/B is Pugh's modulus ratio). This model has been verified by comparing the calculated values with experiments of various materials, it showed that they were in good agreement with experimental results.

Electron-phonon coupling: is the value indicating the degree of interaction between lattice vibrations and electrons. This interaction is important not only in creating the phonon scattering of the electrons but also in the formation of Cooper pairs which is the cause of the superconductivity in material. The electron-phonon coupling is implemented within some DFT calculation platforms (such as Quantum Espresso). Critical temperature (T_c) can be computed by the Allen and Dynes formula [18] (the modified McMillan formula)

$$T_C = \frac{\omega_{\log}}{1.2}\exp\left[-\frac{1.04(1+\lambda)}{\lambda-\mu^*(1+0.62\lambda)}\right]$$

where $\omega_{\log}$, λ, and μ^* are logarithmic average frequency, electron-phonon coupling constant, and effective Coulomb interaction, respectively.

5. Calculating/analyzing to find the evidence that indicates what are the effects of transition metals in the TMB_4s under high pressure. The electronic structures of compounds by mean *d*-states of TM and *s-p* hybridization of boron will be investigated.
6. Summarizing and preparing manuscripts

4. Results and discussion

Part 1: Ruthenium tetraboride (RuB_4)

Firstly, the energetics of crystal structures of RuB_4 obtained from the crystal search and the analogous structures with other metal tetraborides are presented. It is found that, at low pressure, the three lowest enthalpy structures consisting of $P6_3/mmc$ (MoB_4-type), Cmcm (OsB_4-type) and $Cmc2_1$ structures are carefully considered. After accurately optimizing these three structures, the $P6_3/mmc$ structure exhibits the most stable phase at ambient pressure with as higher enthalpy respecting to that of the Cmcm structure. This result also insists that our prediction is reliable because it agrees with the previous prediction [19]. By increasing pressure up to 500 GPa, the relative enthalpies versus pressure of calculated phases are depicted in Figure 1. For high-pressure phases, a monoclinic structure, C2/c, is more stable than the ambient phase at pressure between 198 to 388 GPa, and then an orthorhombic phase, Immm, energetically prefers to be the high-pressure phase of RuB_4 under further compression up to 500 GPa.

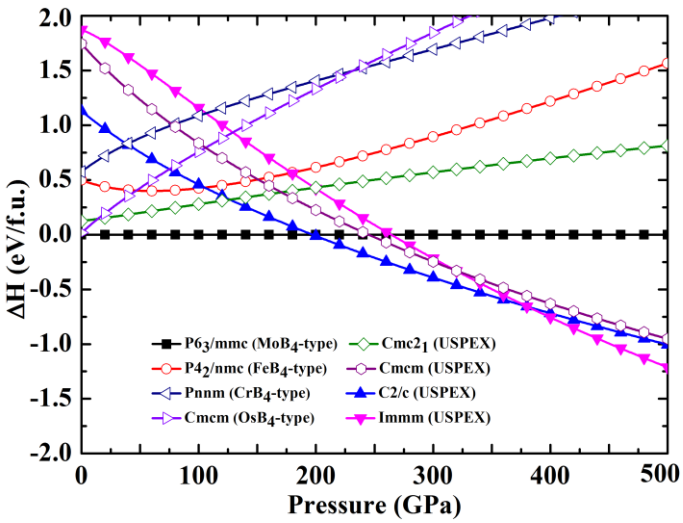

Figure1: Relative enthalpy of the calculated phases as a function of pressure with referenced to the $P6_3/mmc$ phase.

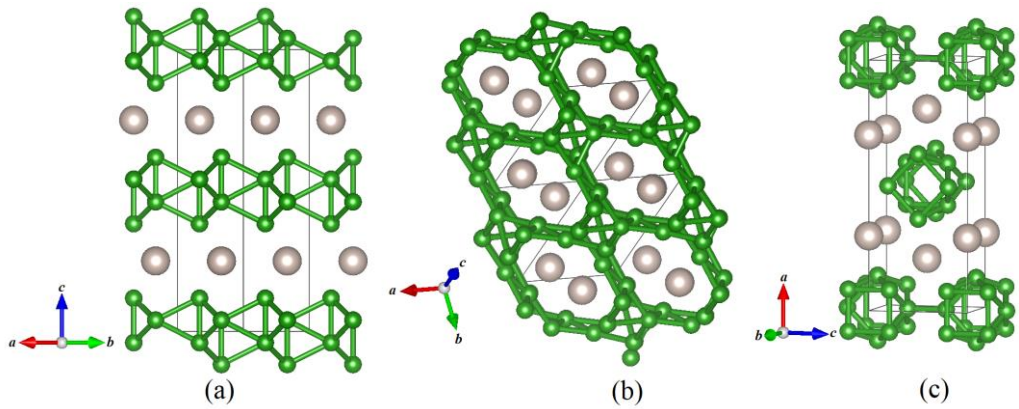

Figure 2: The atomic configurations of the predicted RuB_4 phases of (a) $P6_3/mmc$ phase at 0 GPa (a = 2.945 Å and c = 10.578 Å with the Wyckoff positions of Ru: 2d(0.667, 0.333, 0.250) and B: 4f(0.667, 0.333, 0.040)), (b)C2/c phase at 200 GPa (a = 5.863 Å, b = 5.597 Å, c = 9.086 Å and β=158.85° with the Wyckoff positions of Ru: 4e(0, 0.381, 0.250) and B1: 8f(0.476,0.355,0.356) and B2: 8f(0.105, 0.604, 0.124)) and (c) the Immm phase at 0 GPa (a = 9.326 Å, b = 2.527 Å and c = 3.818 Å with the Wyckoff positions of Ru: 4e(0.2, 0.5, 0.5), B1: 8m(0.084, 0 ,0.206), B2: 4j(0, 0.5, 0.307) and B3: 4f(0.132, 0.5, 0)) .

After applying pressure, the characterization of B atoms has evolved. In other words, the networks of B atoms of the three phases surrounding the Ru atoms, transform into the different features. The atomic configurations of the AB stack of the $P6_3/mmc$ phase, the honeycomb-like boron of the C2/c phase and the B_{12} cluster of the Immm phase are demonstrated in Figure2(a-c). In summary, the B atoms in RuB_4 prefer to form the stack or cluster rather than to interact with the Ru atoms. This result implies to the low hardness of this material. The volume (V_0), bulk modulus (B_0) and pressure derivative of bulk modulus at zero pressure (B'_0) fitted by Birch-Murnaghan EOS [20] of ambient and high-pressure phases of RuB_4, FeB_4 and OsB_4 are demonstrated in Table 2. The V_0s of the predicted phases of RuB_4 are larger than those of FeB_4 but smaller than those of OsB_4, reflecting the fact that the V_0 of theTMB_4 depends on the size of transition metal. The B_0, which indicates the compressibility of materials, of the ambient phase of RuB_4 is approximately same with that of FeB_4 (Pnnm), but significantly lower than that of OsB_4 (Pmmn). However, the bulk moduli (B) of these three materials computing from the VRH approximation aline in the same trend of bulk moduli of their metal elements (B_{Fe}< B_{Ru}<B_{Os}). The difference between the bulk moduli of FeB_4 obtained by both methods is a main reason of contradict result. In this scenario, it is found that the bulk modulus of

FeB_4 using VRH approximation is more reasonable because its value is closer to experimental value (252.5 GPa) [8] than that of EOS-fitting value.

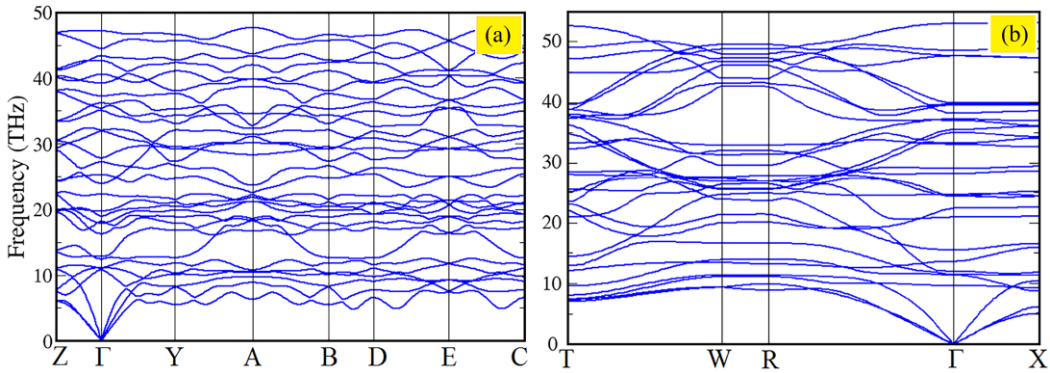

Figure 3: Phonon dispersion of the novel phases of RuB_4 consisting of (a) the C2/c at 200 GPa and (b) the Immm phase at 400 GPa.

Here the dynamical stability of novel phases, e.g. the C2/c and the Immm phases are examined, by performing phonon dispersion calculations. The results indicate that the C2/c and Immm phases at pressure 200 and 400 GPa, respectively, are the dynamically stable phases of RuB_4 as the absence of imaginary frequency (Figure 3(a,b)). Once the phonon dispersions of the $P6_3/mmc$ phase was verified by the previous study.5 The established structural stability of the P63/mmc, the C2/c and the Immm phases provides us a guidance for investigating electronic structures. It is found that all the calculated phases exhibit the metallic phase with, nearly the Fermi level, the valence bands mainly dominated by 2p-B and 4d-Ru states but additional 2s-B state contributing the conduction bands as shown in Figure 4(a-c). Intriguingly, in contrast to the isoeletronic materials, FeB_4 and OsB_4, belonging a metal-to-semiconductor phase transition, RuB_4 has predicted nonsemiconducting phases. Although the semiconducting $P4_2/nmc$ phase, which has been predicted in both FeB_4 and OsB_4, is calculated, it has higher enthalpy comparing to those of other candidates in RuB_4 (Figure 1). However the band structure of the C2/c phase which probably closes to the semiconductive feature is carefully considered. It has the double nodes at the Fermi level and across the M and Z points (Figure 4b). This band structure corresponds to a semimetal feature obviously supported by the node of total DOS at the Fermi level. The band structure calculated by using a hybrid HSE06 functional35 is also performed to verify this issue as shown in the inset of Figure 4b. The energy gap does not open in the HSE06 band structure and it confirms that the C2/c phase seems to be a semimetal as well.

Table 1: Calculated elastic constants (C_{ij}) of the predicted phases of RuB_4 at the stable pressures.

TMB_4-Phase	P(GPa)	elastic constants (GPa)												
		C_{11}	C_{12}	C_{13}	C_{15}	C_{22}	C_{23}	C_{25}	C_{33}	C_{35}	C_{44}	C_{46}	C_{55}	C_{66}
RuB_4-$P6_3/mmc$	0	438	146	172					803		160			
RuB_4-$P6_3/mmc$	150	1,077	520	600					1,632		398			
RuB_4-$C2/c$	200	1,416	637	857	81	1,443	726	20	1,264	-44	444	-109	413	249
RuB_4-$Immm$	400	2,284	1,250	1,184		2,192	1,244		2,037		540		491	483

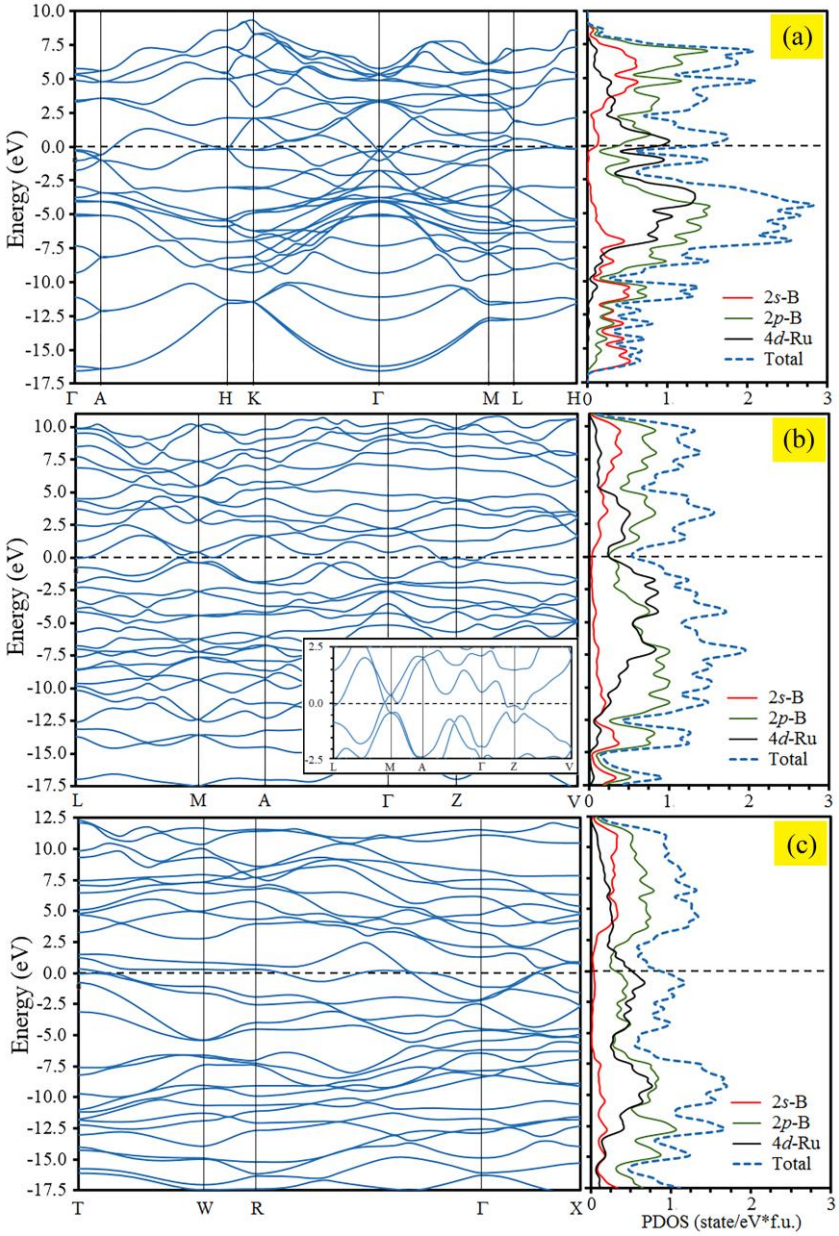

Figure 4: Band structure and partial density of state (PDOS) provided by using GGE-PBE with ultrasoft pseudopotential of (a) the $P6_3$/mmc phase at 0 GPa, (b) the C2/c phase at 200 GPa (the inset is its band structure of around the Fermi energy using HSE06 calculation), (c) the Immm phase at 400 GPa.

Table 2: Illustration of calculated bulk modulus (B), shear modulus (G), Young′s modulus (E), the Vickers hardness (H_v), and volume (V_0), bulk modulus (B_0) and pressure derivative of bulk modulus at zero pressure (B'_0) fitted by Birch-Murnaghan EOS.

	P	Moduli(GPa)				H_v	EOS fitting parameters		
TMB_4-Phase	(GPa)	B	G	E	G/B	(GPa)	V_0(Å^3)	B_0(GPa)	B'_0
RuB_4-$P6_3/mmc$	0	284	168	421	0.59	18.7	39.7	271	3.84
RuB_4-$P6_3/mmc$	150	785	345	903	0.44				
RuB_4-$C2/c$	0	281	111	294	0.40	7.6	38.3	286	3.86
RuB_4-$C2/c$	200	950	325	875	0.34				
RuB_4-$Immm$	0	188	131	319	0.70	19.7	39.0	223	4.24
RuB_4-$Immm$	400	1536	488	1323	0.32				
FeB_4-$Pnnm$	0	261	207	491	0.79	31.5	35.8	270	3.64
FeB_4-$P4_2/nmc$	0	316	253	599	0.80	36.3	33.8	307	3.95
FeB_4-$I4_1/acd$	0	314	272	633	0.87	41.9	33.8	312	3.87
OsB_4-$Pmmn$	0	293	217	522	0.74	29.7	41.1	296	3.95
OsB_4-$P4_2/nmc$	0	330	242	593	0.73	31.5	39.9	331	3.92

The elastic constants C_{ij} of the predicted phases of RuB_4 are listed in Table 1. These constants can be used to indicate the elastic stability and mechanical properties of solids. By using elastic stability criterion of Born the necessary and sufficient conditions of each crystal system were listed in the literatures [21,22]. It is found that all calculated phases of RuB_4 are elastically stable under their own conditions at stable pressures. In Table 2, in order to calculate the H_v of the predicted phases, the bulk modulus (B), shear modulus (G) and Young's modulus (E) are estimated by using the VRH approximation. Based on the Chen's model, the H_v would dominantly depend on the magnitudes of G/B and G. It is found that most of G/B and G of RuB_4 phases are much lower than those of the selected phases of FeB_4 and OsB_4, reflecting the lower H_v of RuB_4 comparing to the isoelectronic materials as well. At 0 GPa, the H_vs of the P63/mmc, C2/c and the Immm phases are calculated to be 18.7, 7.6 and 19.7 GPa, respectively, mentioning that the predicted phases of RuB_4 are not the hard material which has the minimal criteria of 20 GPa. As previous mentioning, the preference of forming boron stacking and clustering structures which have the lower G/B and G than those of the 3D networking metal-boron structures of FeB_4 and OsB_4 [9,10]. This finding could be directly explained by the atomic configurations of its individual structure which lead to the nature of chemical bonding.

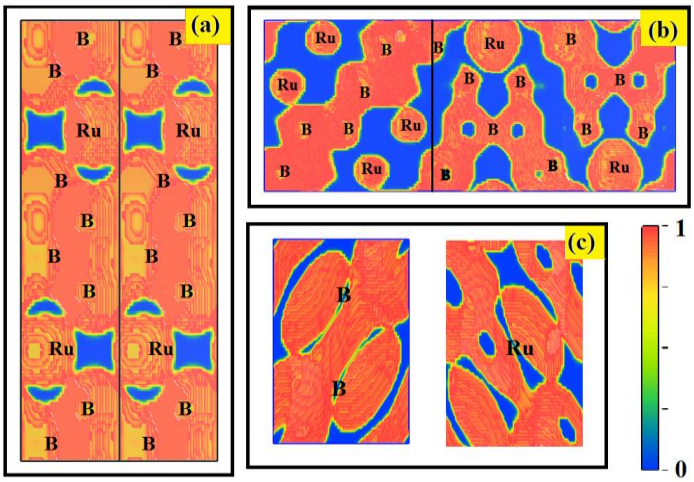

Figure 5: Visualizations of electron localization function (ELF) of (a) the P63/mmc phase at 0 GPa in the plane perpendicular to [100] direction, (b) C2/c phase at 200 in the plane perpendicular to [110] direction and (c) Immm phase at 400 in the planes perpendicular to [100] direction.

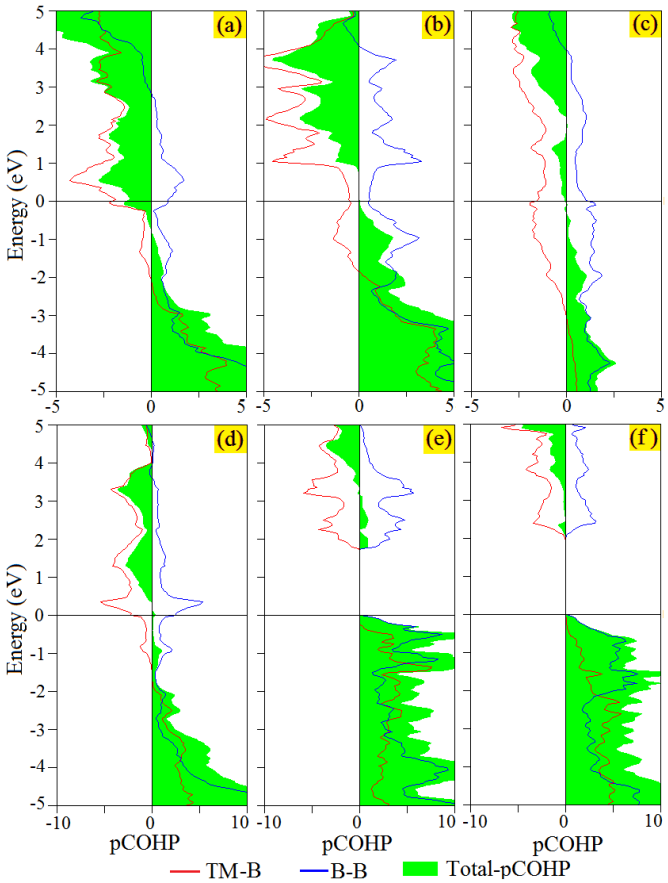

Figure 6: Plot of the projected crystal orbital Hamilton populations (pCOHP) versus energy of the predicted phases of RuB_4 and the selected phases of FeB_4 and OsB_4 consisting of (a) the RuB_4-$P6_3$/mmc phase at 0 GPa, (b) the RuB_4-C2/c phase at 200 GPa, (c) the RuB_4-Immm phase at 400, (d) the FeB_4-Pnnm, (e) the FeB_4-$P4_2$/nmc and (f) the OsB_4-$P4_2$/nmc.

The electron localization function (ELF) [23], Mulliken population analysis (MPA) [24] and projected crystal orbital hamilton populations (pCOHP) [25] which infer to the nature of chemical bonding of atoms, are calculated to elucidate the findings. In Figure 5 (a-c), the features of ELF of the P63/mmc, the C2/c and the Immm phases obviously show that the numbers of electrons prefer to localize at the interdistance of B atoms but they are very few at the ways connecting between Ru atoms to others. This finding points out the metallic state and the mechanical property of the calculated phases of RuB_4. By analyzing the MPA, it is found that the electron of 2s-B state is promoted into the 2p-B state about 1.0e as well as the donation of 5s-Ru state resulting of the different electronegativity of B and Ru atoms. Consequently, the increase of 2p-B and the electropositive charge of Ru atom are approximately 2.34e and +0.84e, 2.63e and +1.39e, 2.70e and +1.31e for the P63/mmc at 0 GPa, the C2/c at 200 GPa and the Immm at 400 GPa, respectively. These results indicate that there should be forming of sp^2 and sp^3 hybridizations within the electronic state of B atoms and forming ionic interaction between B and Ru atoms. The populations of B-B and Ru-B bondings are evaluated by using pCOHP calculation which interpret the calculated wavefunction into the covalent perspective, as obeyed in Figure6(a-c). It is found that, below the Fermi energy, all the populations of the B-B bondings are positive indicating there might be the high degrees of covalent bonds in the B-B pairs, but those of Ru-B bondings process the antibondings above -2 eV supporting the a few numbers of localized electron around the Ru atoms in ELF results. While magnifying at the Fermi level and above, the total of pCOHPs reveals that the population tails of antibondings of the P63/mmc and the Immm phases are over the Fermi level, which is a characteristic of metal, but, for the C2/c phase, there is a gap above the Fermi energy which implies to its semimetal state. The pCOHPs of the selected hard phases of FeB4 and OsB4 are illustrated in Figure 6(d-f), i.e., FeB_4-Pnnm (H_v=31.5 GPa), FeB_4-$P4_2$/nmc (H_v=36.3 GPa) and OsB_4-$P4_2$/nmc (H_v=31.5 GPa), to conceive what are the foundations of hardness for this material family. The metallic phase, FeB4-Pnnm, has the B-B bondings and Fe-B antibondings around the Fermi energy, while its Fe-B bondings are significantly stronger than those of B-B pairs at energy interval of -4 to -2 eV (Figure 6d) supporting the strong Fe-B covalent bonding in FeB_4-Pnnm.7 For the semiconducting phases, the $P4_2$/nmc phase of FeB_4 and OsB_4, have the high-density bondings for both B-B and Fe- or Os-B pairs at the occupied states (Figure 6(e-f)) indicating the strong and directional covalent bondings in these semiconducting phases. Based on the results of ELF, MPA

and pCOHP associating with atom configurations, band structures and PDOSs, it is worth mentioning that the predicted phases of RuB4 are formed by frameworks of the B-B covalent bondings and the interlayer B-Ru ionic bonding and antibonding. Meanwhile the hard/superhard phases of FeB_4 and OsB_4 have been suggested by forming the strong and directional covalent bondings of both B-B and TM-B pairs. These should be resulting in the difference of inexistent semiconducting phase of RuB_4 comparing the FeB_4 and OsB_4, as well as their disadvantages in mechanical properties comparing to its family.

Part 2: Lithium peroxide (Li_2O_2)

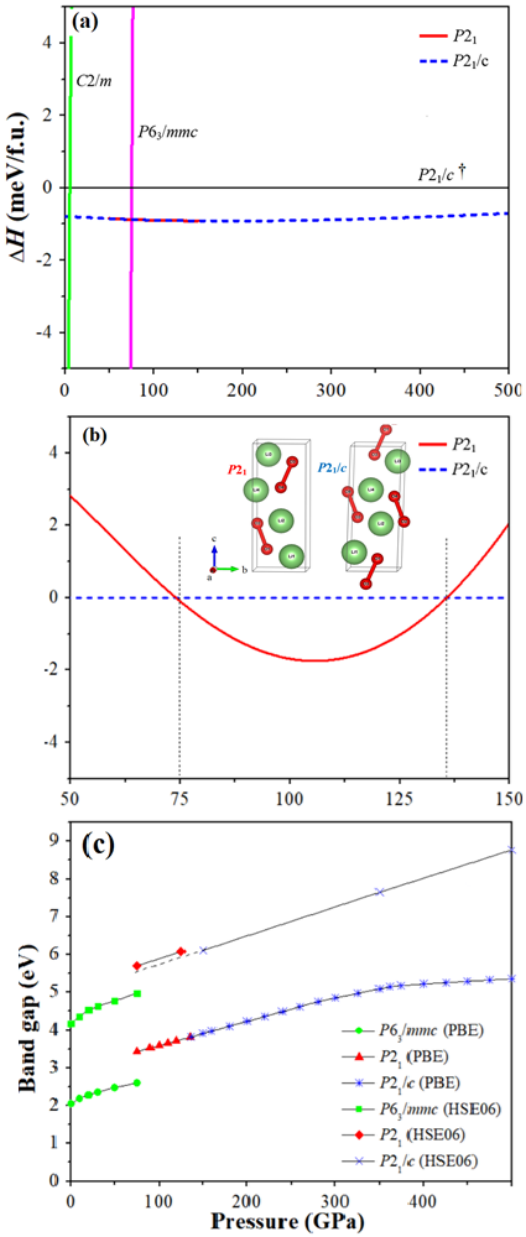

Figure 7: Pressure dependences of (a) relative enthalpies of the possible phases, (b) relative enthalpies of the *P2₁/c* and *P2₁* phases and (c) calculated band gaps by using PBE and HSE06 of the *P6₃/mmc*, *P2₁/c* and

From the structural searching results for Li_2O_2 up to 500 GPa, the lowest enthalpy structures at different pressures have been found. At 0 and 50 GPa, the $P6_3$/mmc structure with 2 and 4 f.u. per cell has a lower enthalpy than the P_1 structure (1 and 3 f.u.). This finding is in agreement with the previous experimental results revealing that the $P6_3$/mmc is stable up to 63 GPa [26,27]. Interestingly, the $P2_1$ (2 and 4 f.u.) structure has been found at 100 GPa, which has a lower enthalpy than the $P2_1$/c (2 and 4 f.u.) and C2/m (1 f.u.) structures at the same pressure. However, the $P2_1$ structure is not found at 200 GPa while the $P2_1$/c (2 f.u.) structure is still maintained up to 500 GPa. This result suggests that the $P2_1$ would probably be transformed to be the $P2_1$/c structure within a pressure range of 100–200 GPa. In Figure 7a and 7b, the transformation pathway based on the thermodynamic stability of Li_2O_2 under pressure up to 150 GPa is $P6_3$/mmc ⟶ $P2_1$ ⟶ $P2_1$/c with the transition pressures 75 and 136 GPa, respectively. The $P2_1$ and $P2_1$/c phases have the lower enthalpies than that of the $P2_1/c^{\dagger}$ which was predicted by previous study. Figure 8c directs the tendencies of the band gaps of the stable phases as increased by increasing pressure for both PBE and HSE06 calculations.

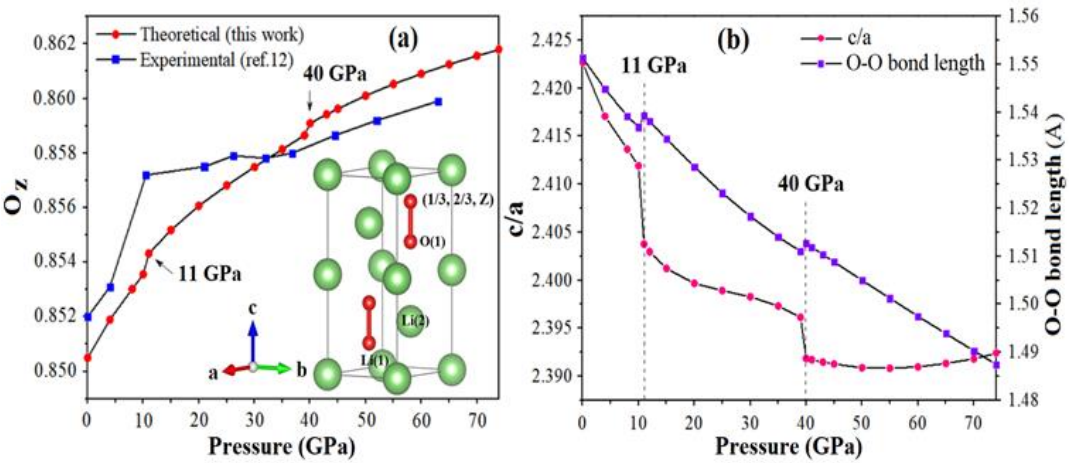

Figure 8: (a) The plot of the z-coordinate of the O atom (O_z) *versus* the pressure range of 0–74 GPa compared with the experimental results proposed by Dunuwille *et al*. [26] (b) The c/a ratio and O–O bond length in the *P6₃/mmc* structure *versus* the same pressure range.

By increasing the pressure, we found that the z-coordinate of the O atom (O_z) for the P63/mmc structure was displaced and the O–O bond length decreased with the increasing pressure, as shown in Figure 8a and 8b, respectively. Surprisingly, the O_z

and O–O bond length significantly changed at pressures around 11 and 40 GPa. The atomic displacement of O_z from 10 GPa to 11 GPa is about 0.0057 Å, which is double its displacement on the trend line at 11 GPa. Likewise, the displacement of the O_z from 39 GPa to 40 GPa is 0.0031 Å, which istwice its displacement on the trend line at 40 GPa, resulting in the O–O bond length increase of about 0.0024 Å at 11 GPa and 0.0017 Å at 40 GPa with respect to its bonds at 10 and 39 GPa, respectively. These results are in line with the experimental results at ambient temperature proposed by Dunuwille *et al.*12 To investigate this situation, we evaluated the length of *c*, *a*, and the *c/a* ratio versus pressure and then considered the change in the interatomic distances of Li(1)– O(1), Li(2)–O(1), and Li(1)–Li(2). We found that the *c/a* ratio is abnormally collapsed around 11 and 40 GPa (see Figure 8b) because the lattice constant *c* has a higher reduction rate than that of lattice constant *a* (Figure 9a). The lattice constant c at 11 GPa deviates from its constant at the same pressure on the trend line about 0.018 Å and 0.009 Å at 40 GPa. In the same way, the reduction of lattice constant *c* from 10 GPa to 11 GPa is twice its constant from 39 GPa to 40 GPa like the reduction of the lattice constant a. In order to investigate the drastic shortening of the *c*-axis and the increased O–O bond lengths at 11 and 40 GPa, the electron localization function (ELF) of the $P6_3/mmc$ structure has been calculated in the pressure range of 0–70 GPa. We found that the ELF isosurface values of the peroxide anion increase within the pressure ranges of 8–11 and 39–40 GPa (see Figure 9b) resulting in the softening of the O–O bond. When the O–O bonds along the c-axis soften, the *c*-axis weakens as well. Moreover, this collapses will have also significantly influenced the change in the interatomic distances of Li(1)-O(1), Li(2)-O(1), and Li(1)-Li(2) around 11 and 40 GPa.

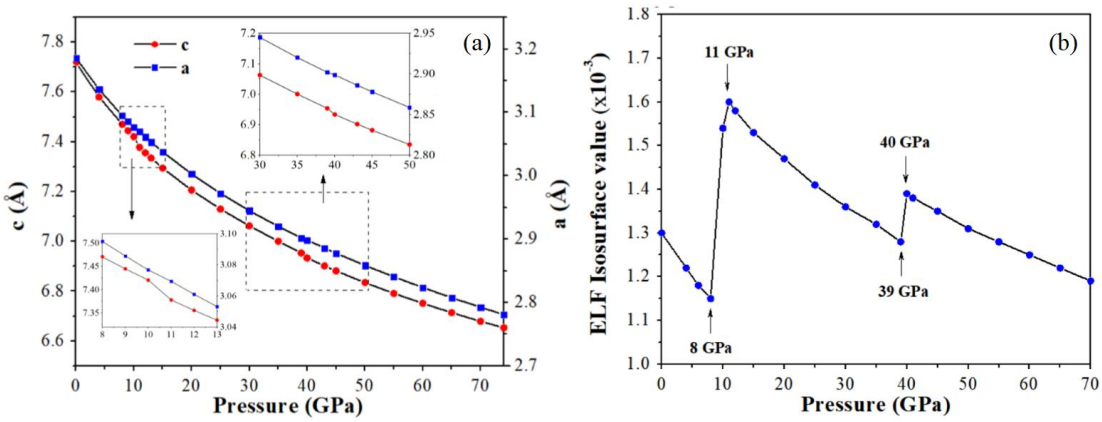

Figure 9: (a) Plot of the lattice constants (*a* and *c*) versus pressure (0-74 GPa). Insets represent the enlargement in the rectangular dashed lines. (b) Plot of the ELF isosurface value for the $P6_3/mmc$ structure in the pressure range of 0-70 GPa.

5. Conclusions

In this project, the structural phase transitions and relating physical properties of RuB_4 and Li_2O_2 under high pressure were investigated using a systematic first-principles study. In RuB_4, the two novel phases of the C2/c and the Immm symmetry have been predicted at 198 and 388 GPa, respectively. The C2/c phase is confirmed to be a semimetal rather than a semiconductor. Therefore, the transformation pathway of RuB_4 under high pressure deviates from that of the isoelectronic materials, FeB_4 and OsB_4, which process the metal-to-semiconductor phase transition. The calculated H_vs of the predicted phases are much lower than those of the selected phases of FeB_4 and OsB_4. This could be explained by the atomic configurations and nature of chemical bondings of the predicted phases of RuB_4 which formed by frameworks of the B-B covalent bondings and the interlayer B-Ru ionic bondings and antibonding around the Fermi level. However, the results of this work provide a more understanding in a family of metal tetraborides for designing metal-boride based hard/superhard materials. For Li_2O_2, $P2_1$ structure, which is slightly different from the previous reported $P2_1/c$ structure, has been proposed. The distortion in the ambient phase ($P6_3/mmc$ structure) of Li_2O_2 reported in previous experiment has been investigated. The finding show that the pressure dependences of band gap, c/a ratio, ELF and phonon dispersion reflect to the structural distortion.

References

[1] Brookes, C.A.; Brookes, E.J. Diamond in perspectiveda review of mechanical properties of natural diamond. *Diamond and Related Materials*, **1991** 1, 13–17.

[2] Wentorf, R.H.; Devries, R.C.; Bundy, F.P. Sintered superhard materials. *Science*, 1**980** 208 (4446), 873–880.

[3] Hebbache, M.; Stuparevic, L.; Zivkovic, D. A new superhard material: Osmium diboride OsB_2. *Solid State Commun.* **2006**, 139, 400227 −231.

[4] Chung, H.-Y.; Weinberger, M. B.; Yang, J.-M.; Tolbert, S. H.; Kaner, R. B. Correlation between hardness and elastic moduli of the ultraincompressible transition metal diborides RuB_2, OsB_2, and ReB_2. *Appl. Phys. Lett.* **2008**, 92, 261904.

[5] Romans, P.A.; Krug, M.P. Composition and crystallographic data for the highest boride of tungsten. *Acta Cryst*, **1966**, 20, 313–315.

[6] Mohammadi, R.; Lech, A.T.; Xie, M.; Weaver, B.E.; Yeung, M.T.; Tolbert, S.H., *et al*. Tungsten tetraboride, an inexpensive superhard material. *Proc. Natl. Acad. Soc. U.S.A.* **2001**, 108, 10958–10962.

[7] Kolmogorov, A.N., *et al*. (2010). New superconducting and semiconducting Fe-B compounds predicted with an ab initio evolutionary search. *Phys Rev Lett*, 105 (21), 217003.

[8] Gou, H., *et al*. (2013). Discovery of a superhard iron tetraboride superconductor. *Phys Rev Lett*, 111 (15), 157002–157005.

[9] Kotmool, K.; Kaewmaraya. T.; Chakraborty, S.; Anversa, J.; Bovornratanaraks, T.; *et al*. Revealing an unusual transparent phase of superhard iron tetraboride under high pressure. *Proc. Natl. Acad. Soc. U.S.A.* **2014**, 111 (48), 17050-17053.

[10] Kotmool, K.; Pinssok, U.; Bovornratanaraks, T.; Rajeev, A. Superhard semiconducting phase of osmium tetraboride stabilizing at 11 GPa. *J. Phys. Chem. C* **2016**, 120, 23165−23171.

[11] Zhang, Y., Wu, L., Wan, B., Zhao, Y., Gao, R., Li, Z., *et al*. Structural variety beyond appearance: high-pressure phases of CrB_4 in comparison with FeB_4. *Phys Chem Chem Phys*. **2006**, 18, 2361-2368.

[12] Kresse, G.; Furthmuller, J. Efficiency of ab-initio total energy calculations for metals and semiconductors using a plane-wave basis set. *Comput. Mater. Sci.* **1996**, 6, 15-50.

[13] Clark, S. J.; Segall, M. D.; Pickard, C. J.; Hasnip, P. J.; Probert, M. I. J.; Refson, K.; Payne, M. C. First principles methods using CASTEP. *Z. Kristallogr.* **2005**, 220, 567-570.

[14] Perdew, J. P.; Burke, K.; Ernzerhof, M. Generalized gradient approximation made simple. *Phys. Rev. Lett.* **1996**, 77, 3865.

[15] Heyd, J.; Scuseria, G. E.; Ernzehof, M. Hybrid functionals based on a screened Coulomb potential. *J. Chem. Phys.* **2003**, 118, 8207.

[16] Oganov, A. R.; Glass, C. W. Crystal structure prediction using ab initio evolutionary techniques: Principles and applications. *J. Chem. Phys.* **2006**, 124, 244704.

[17] Chen, X.-Q.; Niu, H. Y.; Li, D. Z.; Li, Y. Y. Intrinsic correlation between hardness and elasticity in polycrystalline materials and bulk metallic glasses. *Intermetallics* **2011**, 19, 1275-1281

[18] Allen P. B.; Dynes R. C. Transition temperature of strong-coupled superconductors reanalyzed. *Phys Rev B* **1975**, 12, 905–922.

[19] Wang, Y.; Yao, T.; Wang, L.-M.; Yao, J.; Li, H.; Zhang, J.; Gou, H. Structural and relative stabilities, electronic properties and possible reactive routing of osmium and ruthenium borides from first-principles calculations. *Dalton Trans.* **2013**, 42, 7041-7050.

[20] Birch, F. Finite elastic strain of cubic crystals. *Phys. Rev.* **1947**, 71, 809–824.

[21] Mouhat, F.; Coudert, F. -X. Necessary and sufficient elastic stability conditions in various crystal systems. *Phys. Rev. B* **2014**, 71, 224104.

[22] Wu, Z.J.; Zhao, E.J.; Xiang, H.P.; Hao, X.F.; Liu, X.J.; Meng, J. Crystal structures and elastic properties of superhard IrN2 and IrN3 from First Principles. *Phys. Rev. B* **2007**, 76, 054115.

[23] Becke, A. D.; Edgecombe, K. E. A simple measure of electron localization in atomic and molecular systems. J. Chem. Phys. 1990, 92, 5397-5403.

[24] Mulliken, R. S.. Electronic population analysis on LCAOMO molecular wave functions. I. *J. Chem. Phys.* **1955**, 23, 1833-1846.

[25] Deringer, V. L.; Tchougreeff, A. L.; Dronskowski R. Crystal orbital Hamilton population (COHP) analysis as projected from plane-wave basis sets. *J. Phys. Chem. A* **2011**, 115, 5461–5466.

[26] M. Dunuwille, M. Kim and C. S. Yoo, Pressure-induced phase and chemical transformations of lithium peroxide (Li_2O_2). *J. Chem. Phys.* **2016**, 145, 084701.

[27] Yang, W.; Kim, D. Y.; Yang, L.; Li, N.; Tang, L.; Amine, K.; Mao, H. -K.; Oxygen-Rich Lithium Oxide Phases Formed at High Pressure for Potential Lithium–Air Battery Electrode. *Adv. Sci.* **2017**, 4, 1600453.

Output จากโครงการวิจัยที่ได้รับทุนจาก สกว.

1. ผลงานตีพิมพ์ในวารสารวิชาการนานาชาติ (ระบุชื่อผู้แต่ง ชื่อเรื่อง ชื่อวารสาร ปี เล่มที่ เลขที่ และหน้า) หรือผลงานตามที่คาดไว้ในสัญญาโครงการ

1. **Komsilp Kotmool**, Prutthipong Tsuppayakorn-aek, Thanayut Kaewmaraya, Udomsilp Pinsook, Rajeev Ahuja and Thiti Bovornratanarak, **"Structural phase transitions, electronic properties and hardness of RuB_4 under high Pressure in comparison with FeB_4 and OsB_4"** submitted to *Journal of Physical Chemistry C* (Q1 journal with Impact factor of 4.309)

2. Pornmongkol Jimlim, **Komsilp Kotmool**, Udomsilp Pinsook, Suttichai Assabumrungrat, Rajeev Ahuja and Thiti Bovornratanaraks, **"Theoretical aspects in structural distortion and the electronic properties of lithium peroxide under high pressure"** *Phys. Chem. Chem. Phys.*, **2018**, 20, 9488. (Q1 journal with Impact factor of 3.567)

2. การนำผลงานวิจัยไปใช้ประโยชน์
   - เชิงพาณิชย์ (มีการนำไปผลิต/ขาย/ก่อให้เกิดรายได้ หรือมีการนำไปประยุกต์ใช้โดยภาคธุรกิจ/บุคคลทั่วไป)

     --
   - เชิงนโยบาย (มีการกำหนดนโยบายอิงงานวิจัย/เกิดมาตรการใหม่/เปลี่ยนแปลงระเบียบข้อบังคับหรือวิธีทำงาน)

     --
   - เชิงสาธารณะ (มีเครือข่ายความร่วมมือ/สร้างกระแสความสนใจในวงกว้าง)

     --
   - เชิงวิชาการ (มีการพัฒนาการเรียนการสอน/สร้างนักวิจัยใหม่)

     - สามารถนำงานวจิยัพื้นฐานไปใช้ในการประกอบการเรียนการสอนรายวิชา Many-body problem, Density functional theory and Solid-state physics

     - ในผลงานที่ 2 เป็นส่วนหนึ่งของวิทยานิพนธ์ในระดับปริญญาเอกของ ดร.พรมงคล จิ้มลิ้ม

3. อื่นๆ (เช่น ผลงานตีพิมพ์ในวารสารวิชาการในประเทศ การเสนอผลงานในที่ประชุมวิชาการ หนังสือ การจดสิทธิบัตร)

   --

ภาคผนวก

Structural phase transitions, electronic properties and hardness of RuB_4 under high pressure in comparison with FeB_4 and OsB_4

Komsilp Kotmool,[*,†,‡] Prutthipong Tsuppayakorn-aek,[¶] Thanayut Kaewmaraya,[§,‖] Udomsilp Pinsook,[¶] Rajeev Ahuja,[⊥] and Thiti Bovornratanaraks[¶]

†*College of Advanced Manufacturing Innovation, King Mongkut's Institute of Technology Ladkrabang, Bangkok, 10520, Thailand*

‡*Department of Physics, Mahidol Wittayanusorn School, Nakhon Pathom, 73170, Thailand*

¶*Extreme Conditions Physics Research Laboratory (ECPRL), Physics of Energy Materials Research Unit, Department of Physics, Faculty of Science, Chulalongkorn University, Bangkok, 10330, Thailand*

§*Department of Physics, Faculty of Science, Khon Kaen University, Khon Kaen 40002, Thailand*

‖*Institute of Nanomaterials Research and Innovation for Energy (IN-RIE), Research Network of NANOTEC- KKU (RNN), Khon Kaen University, Khon Kaen 40002, Thailand*

⊥*Condensed Matter Theory Group, Department of Physics and Astronomy, Uppsala University, Box 516, S-751 20, Uppsala, Sweden*

E-mail: komsilp.ko@kmitl.ac.th

Phone: +66 (0)2 329 8263. Fax: +66 (0)2 329 8263

Abstract

We have employed an evolutionary algorithm with first-principles calculations to investigate the pressure-induced structural evolution of RuB_4 up to 500 GPa. The ambient phase is predicted to be a hexagonal structure ($P6_3/mmc$). The novel phases consisting of monoclinic ($C2/c$) and orthorhombic ($Immm$) structures are proposed to be the high-pressure phases at the pressure intervals of 198 - 388 GPa and beyond 388 GPa, respectively. The stability of predicted phases is confirmed by both dynamic and elastic calculations. The electronic and mechanical properties of the predicted phases are evaluated and mainly discussed comparing to the isoelectronic metal tetraborides, i.e., FeB_4 and OsB_4. In contrast to FeB_4 and OsB_4, all the stable phases of RuB_4 are metal or semimetal, and any semiconducting phases do not emerge in the transformation pathway of RuB_4. The nature of chemical bonding investigated by ELF, MPA and pCOHP calculations reveals that the atomic configurations and the degree of covalent bonding of the predicted phases are responsible for lower hardness compared to those of FeB_4 and OsB_4. The results of this work provide more understanding of the family of metal tetraboride for designing metal-boride based hard/superhard materials.

Introduction

Transition-metal borides (TMBs) have drawn intensive attension because of superior hardness that could be utilized in high strength cutting and drilling tools.[1–9] Especially, TMB_4s, such as WB_4 and FeB_4, have been put to test and assert as the superhard materials with Vickers hardness (H_v) exceeding 40 GPa.[3,5] Moreover, their additional functionalities as superconductors[4–6] and semiconductors[4,6] have been reported.

For instance, iron tetraboride (FeB_4) exhibits a superhard and superconducting properties.[4,5] Its high pressure phases (the tetragonal structures with space groups of $I4_1/acd$ and $P4_2/nmc$) are the semiconducting and hard/superhard materials.[6,10] Recently, the structural transitions sequence of osmium tetraboride (OsB_4) has been presented up to 300 GPa.[11,12] At 11 GPa, the $P4_2/nmc$ phase emerges in OsB_4 similarly resembling FeB_4.[6] Both FeB_4

and OsB_4 undergo a metal-to-semiconductor phase transition. The semiconducting FeB_4 and OsB_4 phases offering potential hard properties are contributed by the strong directional covalent bondings of three-dimension (3D) boron networks and the significant covalency of TM-B pairs. While theoretically compressing CrB_4 which starts by the identical *Pnnm* phase with FeB_4, but it did not encounter the high-pressure semiconducting phase.[13] It is important to remark that Fe and Os are in the group of 8B element in periodic table that share the analogous electronic configuration, as a result of the related transformation pathway under high pressure of FeB_4 and OsB_4.

Ruthenium (Ru) is one of group 8B element which share a fact with Fe and Os that they should maintain the hexagonal close packed (hcp) structure at extreme pressure and temperature.[14–16] To enhance the advantage of mechanical property, increasing stoichiometry of B content has been concentrated on Ru-B binary compounds. It was reported that RuB_2 has the Vicker's hardness (H_v) of 23.4 GPa.[17] The ambient phase of RuB_4 was predicted as a hexagonal structure (s.g. $P6_3/mmc$) with having the H_v value of 23.5 GPa. This phase could be synthesized under associating high pressure and temperature because it has lower stability compared with its relative with lower B concentrations and α-B at ambient pressure.[17] However, it is important to further investigate the stability and physical properties of this material under high pressure, in order to fulfill the physical understanding of the TMB_4s where TM is the 8B transition metals, i.e., Fe, Ru and Os. Therefore, the present study aims at theoretically investigating the high-pressure behaviors of RuB_4 up to 500 GPa. The unexpected finding that the transformation pathway of RuB_4 deviates from its isoelectronic materials (TM = Fe and Os) is focused and discussed using available tools based on density functional theory method.

Computational Methods

The heuristic evolutionary algorithm (EA) as implemented in USPEX[18,19] interfacing with VASP code[20,21] was comprehensively used to predict the global structures of RuB_4 at pressure range 0 - 500 GPa. The searches were performed by varying the cell size up to 4 formula units per cell (f.u./cell) and operated at 0, 50, 100, 200, 300, 400 and 500 GPa. The crystal structures of other TMB_4s, including FeB_4[6] and OsB_4[11] and CrB_4[13] were also considered in the calculations for the comparative purposes. The CASTEP code[22] employing the generalized gradient approximation functional (GGA-PBE)[24] and the ultrasoft pseudopotential[23] with the electronic configurations of Ru: $4s^2 4p^6 4d^7 5s^1$ and B: $2s^2 2p^1$ was used for the structural optimization. The cutoff energy of 500 eV and dense k-point meshes (spacing between k-points of $0.03 \times 2\pi$ Å^{-1}) were verified for all calculations to attain the energy convergence within 1 meV/f.u.. The Birch–Murnaghan equation of state (BM-EOS)[25] was used to fit the energy-volume curves to determine the thermodynamic stability phases. Phonon dispersion based on supercell and finite displacement approaches as implemented in Phonopy code[26] was performed to confirm the dynamic stability. Furthermore, the elastic constants (C_{ij}) were calculated to evaluate the elastic stability according to Born criteria.[27,28] Afterwards, bulk moduli (B), shear moduli (G) and Young's moduli (E) were calculated using the Voigt-Reuss-Hill approximation.[29] The Vickers hardness (H_v) was estimated using the empirical Chen's model,[30] $H_\nu = 2.0(k^2G)^{0.585}$ - 3.0; k = G/B. The electron localization function (ELF),[31] Mulliken population analysis (MPA),[32] and projected crystal orbital Hamilton populations (pCOHP)[33] (using LOBSTER code[34]) were used to elucidate the nature of chemical bonding of the stable phases.

Results and Discussion

We begin by presenting the energetics of crystal structures of RuB_4 obtained from the crystal search and the prototypical structures of analogous transition metal tetraborides. As

shown in Figure 1, *P6*$_3$*/mmc* (MoB_4-type), *Cmcm* (OsB_4-type) and *Cmc2*$_1$ structures are energetically favorable at low pressure. After accurately optimizing these three structures, the *P6*$_3$*/mmc* structure is the most stable phase at ambient pressure compared with the *Cmcm* structure agreeing with the reported prediction.[17] Meanwhile, monoclinic *C2/c* becomes stable phase at pressure between 198 to 388 GPa beyond which orthorhombic *Immm* energetically emerges as the high-pressure phase of RuB_4.

Table 1 assembles the crystallographic information of the stable phases and Figure 2 shows their atomic structures. The B atoms in the *P6*$_3$*/mmc* phase are formed as separate layers stacked alternatively with Ru layers along the c-direction. On the other hands, the B atoms are forced to form connected networks and clusters in the *C2/c* and *Immm* phases because of the reduced atomic distances at high pressure. Moreover, the volume (V_0), bulk modulus (B_0) and pressure derivative of bulk modulus at zero pressure (B'_0) fitted by Birch-Murnaghan EOS of the ambient and high-pressure phases of RuB_4, FeB_4 and OsB_4 are demonstrated in Table 2. The V_0 values of the predicted phases of RuB_4 are greater than those of FeB_4, but smaller than those of OsB_4, reflecting the fact that the V_0 parameter of TMB_4 depends on the atomic size of transition metals. We also found that B_0 which accounts for the compressibility of materials of the ambient phase of RuB_4 is approximately resembles that of FeB_4 (*Pnnm*), but significantly lower than that of OsB_4 (*Pmmn*). However, the bulk moduli (B) of these TMB_4s evaluated by the VRH approximation show in the same trend as the bulk moduli of the metal elements (i.e., $B_{Fe} < B_{Ru} < B_{Os}$).[14–16] The difference between the bulk moduli of FeB_4 obtained by both the methods is responsible for contradictory result. In this scenario, the bulk modulus of FeB_4 using VRH approximation is more reasonable because its value is closer to the experimental value (252.5 GPa)[5] than that of the EOS-fitting value.

We here examined the dynamical stability of novel phases, e.g. the *C2/c* and the *Immm* phases, by performing phonon dispersion calculations. The results indicate that the *C2/c* and *Immm* phases at pressure 200 and 400 GPa, respectively, are the dynamically stable phases as the absence of imaginary frequency (Figure 3(a,b)). Once the phonon dispersions

of the *P6*$_3$*/mmc* phase was verified by the previous study.[5]

The established structural stability of the *P6*$_3$*/mmc*, *C2/c* and *Immm* phases leads us to further investigate electronic structures. It is found that all the phases exhibit the metallic feature as shown in Figure 4(a-c). At nearly the Fermi level, the valence bands are mainly dominated by 2p-B and 4d-Ru states but additional 2s-B state contributes the conduction bands. Intriguingly, all the predicted phases of RuB_4 are non-semiconductor, differing from the reported metal-to-semiconductor phase transition in the isoeletronic materials, i.e., FeB_4 and OsB_4. Although the semiconducting *P4*$_2$*/nmc* phase, which has been predicted in both FeB_4 and OsB_4, is considerably calculated, it processes higher enthalpy compared to those of other candidates in RuB_4 (see Figure 1). We, however, carefully consider the band structure of the *C2/c* phase which probably closes to the semiconductive feature. It has the double nodes at the Fermi level and across the M and Z points which corresponds to a semimetal feature (Figure 4b). The band structure by hybrid HSE06 functional[35] as shown in the inset of Figure 4b clarifies that the energy gap does not open.

Moreover, the elastic constants C_{ij} of the predicted phases of RuB_4 are listed in Table 1. These constants can be used to indicate the elastic stability and mechanical properties of solids. The elastic stability criteria of Born listed in the literatures[27,28] manifest that all the predicted phases of RuB_4 are elastically stable under their suitable pressure ranges. In Table 2, in order to estimate the H_v value of the predicted phases, the bulk modulus (B), shear modulus (G) and Young's modulus (E) are calculated by using the VRH approximation. Based on the Chen's model, a H_v value dominantly depends on the magnitudes of G/B and G. It is found that the most of G/B and G values of RuB_4 phases are much lower than those of the selected phases of FeB_4 and OsB_4, revealing that all the phases of RuB_4 are relatively softer than these of FeB_4 and OsB_4 as well. At 0 GPa, the H_v values of the *P6*$_3$*/mmc*, *C2/c* and the *Immm* phases are calculated to be 18.7, 7.6 and 19.7 GPa, respectively, indicating that the predicted phases of RuB_4 are not classified as a hard material according to the minimal criteria of 20 GPa of hardness.[36] The softness of this material is attributed to the

tendency of forming planar stacking or clustering of B atoms, unlikely the strong 3D boron networking in FeB_4 and OsB_4.[6,11]

Furthermore, the electron localization function (ELF), shown in Figure 5(a-c), indicates that electrons in the *P6*$_3$*/mmc*, *C2/c* and *Immm* phases are delocalized to render the metallic feature. In addition, the spatial electron distributions between B atoms are covanlent-like, whereas there is the absence of electron cloud in the interstitial regions among Ru and B atom. Hence the Ru-B bonds are characterized as ionic. In particular, the degree of delocalization in the *C2/c* phase (H_v=13.8 GPa at P = 200 GPa) is relatively less than the *P6*$_3$*/mmc* and *Immm* (H_v=16.6 GPa at P = 400 GPa) counterparts. This explains its lowest hardness as compared to others. Moreover, the ELFs of selected hard phases of FeB_4 and OsB_4 are comparatively illustrated in Figure 5(d-f), i.e., FeB_4-*Pnnm* (H_v=31.5 GPa), FeB_4-*P4*$_2$*/nmc* (H_v=36.3 GPa) and OsB_4-*P4*$_2$*/nmc* (H_v=31.5 GPa), to conceive what are the foundations of hardness of this material family. It is very obvious to conclude that the selected FeB_4 and OsB_4 phases are harder than those of RuB_4 because Fe and Os atoms have higher potential of forming stronger bondings with B atoms compared to Ru atom, as illustrated by the larger localized electrons around Fe and Os atoms. Mulliken population analysis (MPA) further reveals that the electron of 2s-B state is promoted into the 2p-B state about 1.0e as well as the donation of 5s-Ru state facilitating by the different electronegativity of B and Ru atoms. Consequently, the increase of 2p-B and the electropositively charged Ru atom are approximately 2.34e and +0.84e, 2.63e and +1.39e, 2.70e and +1.31e for the *P6*$_3$*/mmc* at 0 GPa, the *C2/c* at 200 GPa and the *Immm* at 400 GPa, respectively. These results indicate that there might be sp^2 and sp^3 hybridizations within the electronic states of B atoms and ionic interaction between B and Ru atoms. The populations of B-B and Ru-B bondings are evaluated by using pCOHP calculation which interpret the wave function into the covalent perspective, as shown in Figure 6(a-c). It is found that, below the Fermi energy, all the populations of the B-B bonds are positive indicating that there is the high degrees of covalent bonds in the B-B pairs, but those of Ru-B bonds process the antibondings above -2

eV supporting a few number of localized electrons around the Ru atoms in ELF results. The pCOHPs of the FeB_4 and OsB_4 are shown in Figure 6(d-f). The metallic phase FeB_4-*Pnnm* has the B-B bonds and Fe-B antibonds around the Fermi energy, while its Fe-B bonds are significantly stronger than those of B-B pairs at energy interval of -4 to -2 eV (Figure 6d) supporting the strong Fe-B covalent bonds in FeB_4-*Pnnm*.[6] For the semiconducting phases, the $P4_2/nmc$ phase of FeB_4 and OsB_4, have the high-density bonds for both B-B and Fe- or Os-B pairs at the occupied states (Figure 6(e-f)) indicating the strong and directional covalent bonds in these semiconducting phases. It is worth emphasizing that the predicted phases of RuB_4 are formed by frameworks of the B-B covalent bondings and the interlayer B-Ru ionic bonding and antibonding. Meanwhile, the hard/superhard phases of FeB_4 and OsB_4 are originated from the strong and directional covalent bonds of both B-B and TM-B pairs. The differences in intrinsic chemical bonds of RuB_4 compared with FeB_4 and OsB_4 are responsible its metallic feature with reduced hardness.

Conclusion

We have investigated structural phase transitions and relating physical properties of RuB_4 under high pressure using the combination of evolutionary structural searching and density functional theory. The two novel phases *C2/c* and *Immm* have been predicted at 198 and 388 GPa, respectively. The *C2/c* phase is a semimetal rather than a semiconductor. Therefore, the transformation pathway of RuB_4 under compression intriguingly deviates from that of the isoelectronic FeB_4 and OsB_4, which undergo the metal-to-semiconductor phase transition. The calculated hardnesses of the predicted phases are comparatively lower than those of FeB_4 and OsB_4. This is attributed to the atomic configurations and nature of chemical bondings of the predicted RuB_4 phases in which frameworks of the B-B covalent bonds and the interlayer B-Ru ionic bonds are formed. Our findings emphasize the significant messages that the atomic arrangements and chemical bonds of B atoms in metal tetraborides play a

decisive role in their hardness.

Acknowledgement

SNIC and SNAC of Sweden are acknowledged for providing part of the computing facilities. K.K. acknowledges support from the Thailand ResearchFund (TRF) contract number TRG6080014. K. K. also would like to thank Dr. Sarot Boonseng of MWIT for his generous and fruitful discussion in chemical aspects. P.T. acknowledges Ratchadapisek Somphot Fund for Postdoctoral Fellowship, Chulalongkorn University. T.B acknowledges Chulalongkorn University; Grant for Research. R.A. would like to thanks Swedish Research Council (VR) for financial support.

References

(1) Kaner, R. B.; Gilman, J. J.; Tolbert, S. H. Designing Superhard Materials. *Science* **2005** *308*, 1268-1269.

(2) Chen, X. Q.; Fu, C. L.; Krcmar, M.; Painter, G. S. Electronic and structural origin of ultraincompressibility of 5d transition-metal diborides MB_2 (M = W, Re, Os). *Phys. Rev. Lett.* **2008**, *100*, 196403.

(3) Mohammadi, R.; Lech, A.T.; Xie, M.; Weaver, B.E.; Yeung, M.T.; Tolbert, S.H.; Kaner, R. B. Tungsten tetraboride, an inexpensive superhard material. *Proc. Natl. Acad. Soc. U.S.A* **2011**, *108*, 10958–10962.

(4) Kolmogorov, A. N.; Shah, S.; Margine, E. R.; Bialon, A. F.; Hammerschmidt, T.; Drautz, R. New superconducting and semiconducting Fe-B compounds predicted with an *ab initio* evolutionary search. *Phys. Rev. Lett.* **2010**, *105*, 217003.

(5) Gou, H.; Dubrovinskaia, N.; Bykova, E.; Tsirlin, A. A.; Kasinathan, D.; Schnelle,

W.; Richter, A.; Merlini, M.; Hanfland, M.; Abakumov, A. M., *et al.* Discovery of a superhard iron tetraboride superconductor. *Phys. Rev. Lett.* **2013**, *111*, 157002-157005.

(6) Kotmool, K.; Kaewmaraya, T.; Chakraborty, S.; Anversa, J.; Bovornratanaraks, T.; Luo, W.; Gou, H.; Piquini, P. C.; Kang, T. W.; Mao, H.-K., Rajeev, A. Revealing an unusual transparent phase of superhard iron tetraboride under high pressure. *Proc. Natl. Acad. Soc. U.S.A* **2014**, *111*, 17050-17053.

(7) Wang, Y.; Wu L.; Lin, Y.; Hu, Q.; Li, Z.; Liu, H.; Zhang, Y.; Gou, H.; Yao, Y.; Zhang, J.; Gao, F. Mao, H.-K. Structures and stability of novel transition-metal (M=Co, Rh, Co and Ir) borides. *Phys. Rev. B* **2015** *92*, 174106.

(8) Kvashnin, A. G.; Zakaryan, H. A.; Zhao, C.; Duan, Y.; Kvashnina, Y. A.; Xie, C.; Dong, H.; Oganov A. R. New tungsten Borides, their stability and outstanding mechanical properties. *J. Phys. Chem. Lett.* **2018**, *9*, 3470-3477.

(9) Kvashnin, A. G.; Allahyari, Z.; Oganov A. R. Computational discovery of hard and superhard materials. *J. Appl. Phys. 126*, 040901.

(10) Jiang, X.; Zhao, J. Evolution of boron clusters in iron tetraborides under high pressure: semiconducting and ferromagnetic superhard materials. *RSC Adv.* **2015**, *5*, 48012-48023.

(11) Kotmool, K.; Pinsook, U.; Bovornratanaraks, T.; Rajeev, A. Superhard semiconducting phase of osmium tetraboride stabilizing at 11 GPa. *J. Phys. Chem. C* **2016**, *120*, 23165-23171.

(12) Zhang, M.; Yan, H.; Wei, Q.; Zheng, B. Reinvestigation of mechanical properties and shear-induced atomic deformation of tetragonal superhard semiconducting OsB_4. *J. Phys. Chem. C* **2017**, **121**, 6290-6299.

(13) Zhang, Y.; Wu, L.; Wan, B.; Zhao, Y.; Gao, R.; Li, Z.; Zhang, J.; Gou, H.; Mao, H.-K. Structural variety beyond appearance: high-pressure phases of CrB_4 in comparison with FeB_4. *Phys. Chem. Chem. Phys.* **2016**, *18*, 2361-2368.

(14) Dubrovinsky, L.; Dubrovinskaia, N.; Bykova, E.; Bykov, M.; Prakapenka, V.; Prescher, C.; Glazyrin, K.; Liermann, H.-P.; Hanfland, M.; Ekholm, M., *et al.* The most incompressible metal osmium at static pressures above 750 gigapascals. *Nature* **2015**, *525*, 226-229.

(15) Sha, X.; and Cohen, R. E. First-principles thermal equation of state and thermoelasticity of hcp Fe at high pressures. *Phys. Rev. B* **2010**, *81*, 094105.

(16) Lugovskoy, A. V.; Belov, M. P.; Krasilnikov, O. M.; Vekilov Y. K. Stability of the hcp Ruthenium at high pressures from first principles. *J. Appl. Phys.* **2014**, *116*, 103507.

(17) Wang, Y.; Yao, T.; Wang, L.-M.; Yao, J.; Li, H.; Zhang, J.; Gou, H. Structural and relative stabilities, electronic properties and possible reactive routing of osmium and ruthenium borides from first-principles calculations. *Dalton Trans.* **2013**, *42*, 7041-7050.

(18) Oganov, A. R.; Glass, C. W. Crystal structure prediction using ab initio evolutionary techniques: Principles and applications. *J. Chem. Phys.* **2006**, **124**, 244704.

(19) Glass, C. W.; Oganov, A. R.; Hansen, N. USPEX evolutionary crystal structure prediction. *Comput. Phys. Commun.* **2006**, *175*, 713-720.

(20) Kresse, G.; Furthmuller, J. Efficient iterative schemes for ab initio total-energy calculations using a plane-wave basis set. *Phys. Rev. B* **1996**, *54*, 11169.

(21) Kresse, G.; Furthmuller, J. Efficiency of ab-initio total energy calculations for metals and semiconductors using a plane-wave basis set. *Comput. Mater. Sci.* **1996**, *6*, 15-50.

(22) Clark, S. J.; Segall, M. D.; Pickard, C. J.; Hasnip, P. J.; Probert, M. I. J.; Refson,

K.; Payne, M. C. First principles methods using CASTEP. *Z. Kristallogr.* **2005**, *220*, 567-570.

(23) Vanderbilt, D. Soft self-consistent pseudopotentials in a generalized eigenvalue formalism. *Phys. Rev. B* **1990**, *41*, 7892.

(24) Perdew, J. P.; Burke, K.; Ernzerhof, M. Generalized gradient approximation made simple. *Phys. Rev. Lett.* **1996**, *77*, 3865.

(25) Birch, F. Finite elastic strain of cubic crystals. *Phys. Rev.* **1947**, *71*, 809–824.

(26) Togo, A.; Tanaka, I. First principles phonon calculations in materials science. *Scr. Mater.* **2015**, *108*, 1-5.

(27) Mouhat, F.; Coudert, F. -X. Necessary and sufficient elastic stability conditions in various crystal systems *Phys. Rev. B* **2014**, *71*, 224104.

(28) Wu, Z.J.; Zhao, E.J.; Xiang, H.P.; Hao, X.F.; Liu, X.J.; Meng, J. Crystal structures and elastic properties of superhard IrN_2 and IrN_3 from First Principles. *Phys. Rev. B* **2007**, *76*, 054115.

(29) Hill, R. The elastic behaviour of a crystalline aggregate. *Proc. Phys. Soc. London Sect. A* **1952**, *65*, 349.

(30) Chen, X.-Q.; Niu, H. Y.; Li, D. Z.; Li, Y. Y. Intrinsic correlation between hardness and elasticity in polycrystalline materials and bulk metallic glasses. *Intermetallics* **2011**, *19*, 1275-1281.

(31) Becke, A. D.; Edgecombe, K. E. A simple measure of electron localization in atomic and molecular systems. *J. Chem. Phys.* **1990**, *92*, 5397-5403.

(32) Mulliken, R. S. Electronic population analysis on LCAOMO molecular wave functions. I. *J. Chem. Phys.* **1955**, *23*, 1833-1846.

(33) Deringer, V. L.; Tchougréeff, A. L.; Dronskowski R. Crystal orbital Hamilton population (COHP) analysis as projected from plane-wave basis sets. *J. Phys. Chem. A* **2011**, *115*, 5461–5466.

(34) Maintz, S.; Deringer, V. L.; Tchougréeff, A. L.; Dronskowski, R. LOBSTER: A tool to extract chemical bonding from plane-wave based DFT. *J. Comput. Chem.* **2016**, *37*, 1030—1035.

(35) Heyd, J.; Scuseria, G. E.; Ernzehof, M. Hybrid functionals based on a screened Coulomb potential. *J. Chem. Phys.* **2003**, *118*, 8207.

(36) Vepřek, S. The search for novel, superhard materials. *J. Vac. Sci. Technol. A* **1999**, *17*, 2401-2420.

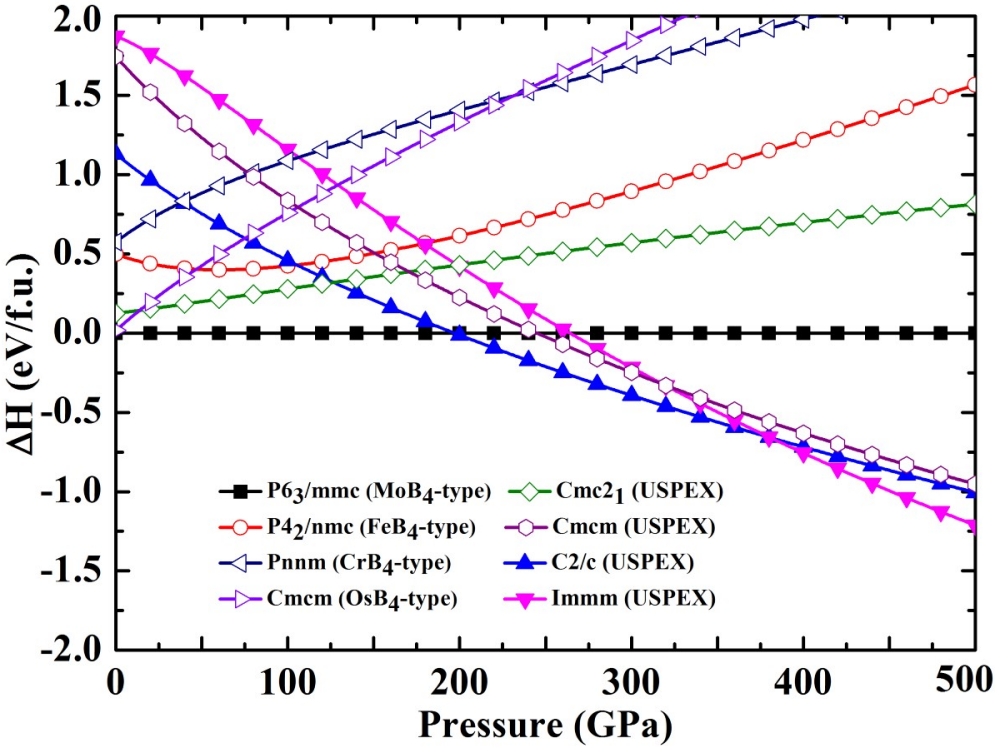

Figure 1: The relative enthalpy of the calculated phases as a function of pressure referenced to the *P6*$_3$*/mmc* phase.

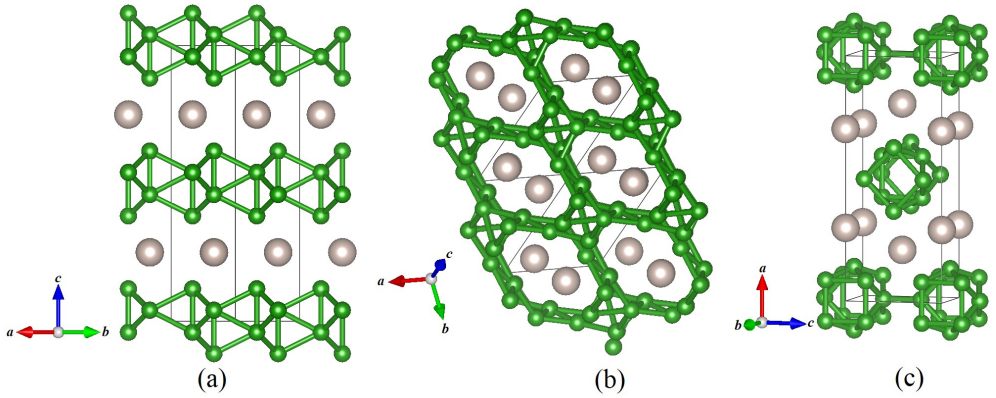

Figure 2: The atomic configurations of the predicted RuB_4 phases of (a) the *P6*$_3$*/mmc* phase at 0 GPa, (b) the *C2/c* phase at 200 GPa and (c) the *Immm* phase at 0 GPa. Gray and green balls represent Ru and B atoms, respectively.

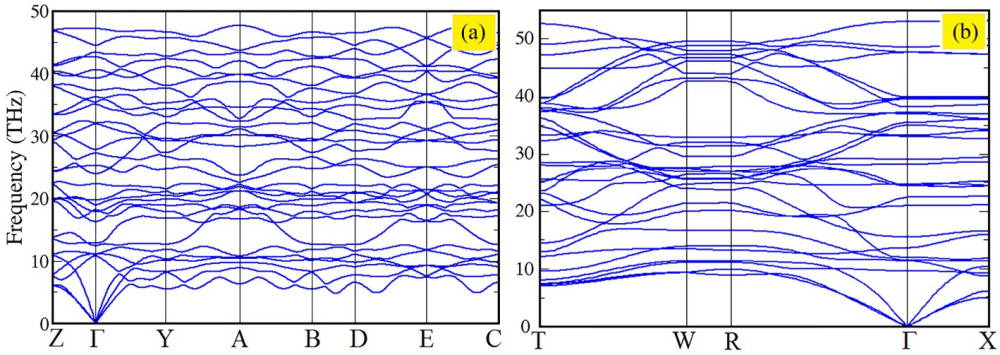

Figure 3: The phonon dispersion of the novel phases of RuB_4 consisting of (a) the *C2/c* at 200 GPa and (b) the *Immm* phase at 400 GPa.

Table 1: The lattice constants, atomic positions and elastic constants (C_{ij}) of the predicted phases of RuB_4 at the stable pressures.

Phase	P(GPa)	Lattice constants	Atomic positions	Elastic constants (GPa)												
				C_{11}	C_{12}	C_{13}	C_{15}	C_{22}	C_{23}	C_{25}	C_{33}	C_{35}	C_{44}	C_{46}	C_{55}	C_{66}
P6₃/mmc	0	a=2.945 Å	Ru:2d(2/3,1/3,1/4)	438	146	172					803		160			
		c=10.578 Å	B:4f(2/3,1/3,0.04)													
C2/c	200	a=5.863 Å	Ru:4e(0,0.381,1/4)	1,416	637	857	81	1,443	726	20	1,264	-44	444	-109	413	249
		b=5.597 Å	B1:8f(0.476,0.355,0.356)													
		c=9.086 Å	B2:8f(0.105,0.604,0.124)													
		β=158.85°														
Immm	400	a=9.326 Å	Ru:4e(0.2,0.5,0.5)	2,284	1,250	1,184		2,192	1,244		2,037		540		491	483
		b=2.527 Å	B1:8m(0.084,0,0.206)													
		c=3.818 Å	B2:4j(0,0.5,0.307)													
			B3:4f(0.132,0.5,0)													

Table 2: The calculated bulk modulus (B), shear modulus (G), Young′s modulus (E), the Vickers hardness (H_v), and volume (V_0), bulk modulus (B_0) and pressure derivative of bulk modulus at zero pressure (B'_0) fitted by Birch-Murnaghan EOS.

	P	Moduli(GPa)				H_v	EOS fitting parameters		
TMB_4-Phase	(GPa)	B	G	E	G/B	(GPa)	V_0(Å^3)	B_0(GPa)	B'_0
RuB_4-*P6₃/mmc*	0	284	168	421	0.59	18.7	39.7	271	3.84
RuB_4-*P6₃/mmc*	150	785	345	903	0.44	20.4			
RuB_4-*C2/c*	0	281	111	294	0.40	7.6	38.3	286	3.86
RuB_4-*C2/c*	200	950	325	875	0.34	13.8			
RuB_4-*Immm*	0	188	131	319	0.70	19.7	39.0	223	4.24
RuB_4-*Immm*	400	1536	488	1323	0.32	16.6			
FeB_4-*Pnnm*	0	261	207	491	0.79	31.5	35.8	270	3.64
FeB_4-*P4₂/nmc*	0	316	253	599	0.80	36.3	33.8	307	3.95
FeB_4-*I4₁/acd*	0	314	272	633	0.87	41.9	33.8	312	3.87
OsB_4-*Pmmn*	0	293	217	522	0.74	29.7	41.1	296	3.95
OsB_4-*P4₂/nmc*	0	330	242	593	0.73	31.5	39.9	331	3.92

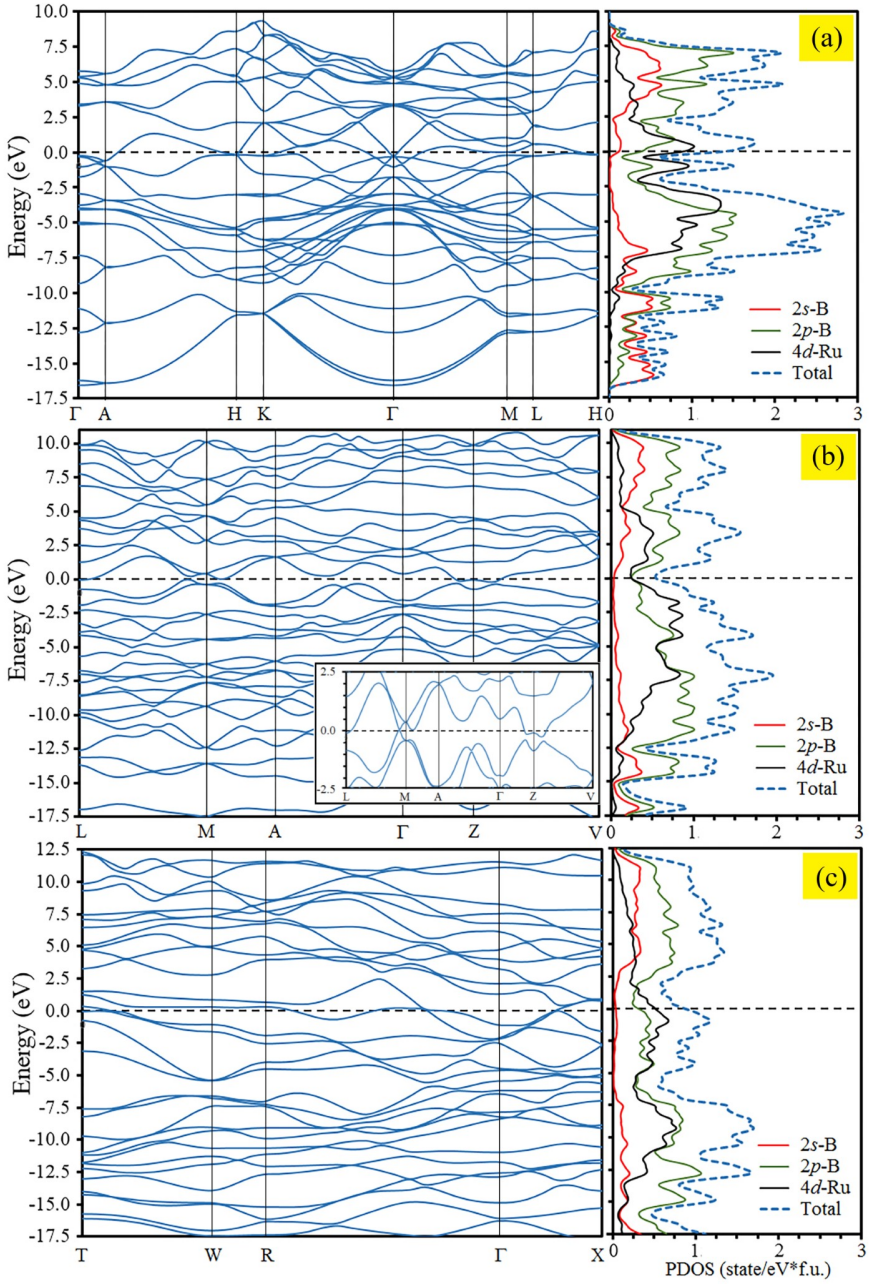

Figure 4: Band structure and partial density of state (PDOS) provided by using GGE-PBE with ultrasoft pseudopotential of (a) the $P6_3/mmc$ phase at 0 GPa, (b) the $C2/c$ phase at 200 GPa (the inset is its band structure of around the Fermi energy using HSE06 calculation), (c) the *Immm* phase at 400 GPa.

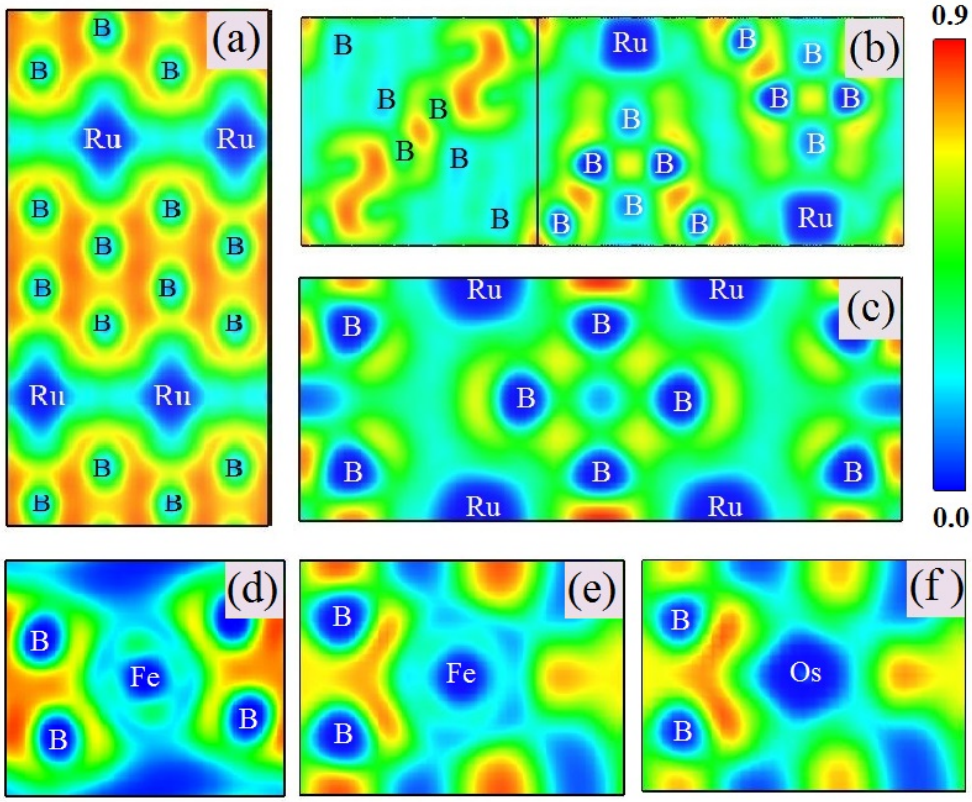

Figure 5: The electron localization function (ELF) of (a) the RuB_4-$P6_3/mmc$ phase at 0 GPa in (200) plane, (b) the $C2/c$ phase at 200 in (100) and (001) planes, (c) the RuB_4-$Immm$ phase at 400 in (001) plane, (d) the FeB_4-$Pnnm$ in (001) plane, (e) the FeB_4-$P4_2/nmc$ in (200) plane, and (f) the OsB_4-$P4_2/nmc$ in (200) plane.

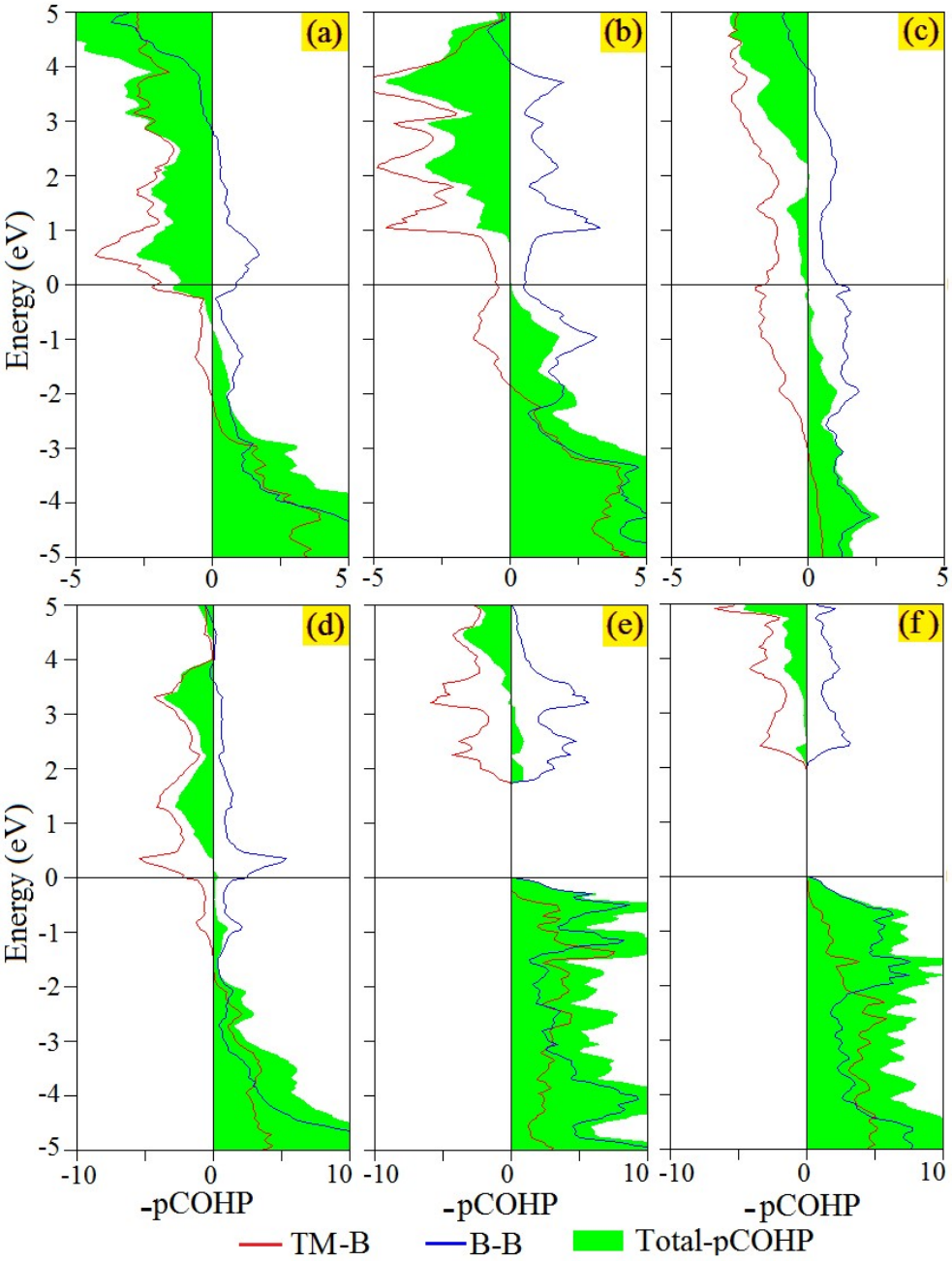

Figure 6: The projected crystal orbital Hamilton populations (pCOHP) of (a) the RuB_4-$P6_3/mmc$ phase at 0 GPa, (b) the RuB_4-$C2/c$ phase at 200 GPa, (c) the RuB_4-$Immm$ phase at 400, (d) the FeB_4-$Pnnm$, (e) the FeB_4-$P4_2/nmc$, and (f) the OsB_4-$P4_2/nmc$.

PCCP

PAPER

View Article Online
View Journal | View Issue

Check for updates

Cite this: *Phys. Chem. Chem. Phys.*, 2018, **20**, 9488

Theoretical aspects in structural distortion and the electronic properties of lithium peroxide under high pressure†

Pornmongkol Jimlim,[ab] Komsilp Kotmool,[b] Udomsilp Pinsook,[ac] Suttichai Assabumrungrat,[d] Rajeev Ahuja[ef] and Thiti Bovornratanaraks *[ac]

Received 27th October 2017,
Accepted 12th February 2018

DOI: 10.1039/c7cp07293g

rsc.li/pccp

The structural phase transition and electronic properties of Li_2O_2 under pressures up to 500 GPa have been investigated using first-principles calculations. Two new structural phase transitions have been proposed at pressures around 75 GPa from the $P6_3/mmc$ structure to the $P2_1$ structure and around 136 GPa from the $P2_1$ structure to the $P2_1/c$ structure. The calculated phonon spectra have confirmed the dynamical stability of these structures. The pressure dependence of the lattice dynamics, O–O bond length, and band gaps in Li_2O_2 have also been reported. The band gaps of the $P6_3/mmc$, $P2_1$, and $P2_1/c$ structures calculated by PBE and HSE06 have shown increasing trends with increasing pressure. Interestingly, the $P6_3/mmc$ band gap and c/a ratio have significantly decreased with the increasing O–O bond length and ELF value around 11 and 40 GPa. At these pressures, the phonon frequency of the O–O stretching modes has softened. This finding reveals the effects of structural distortion in three phases of Li_2O_2. Our study provides structural understanding and the electronic properties of Li_2O_2 under high pressure, which might be useful for investigating the charge transport through Li_2O_2 in lithium–air batteries and CO_2 capture.

1 Introduction

Lithium peroxide (Li_2O_2) is an oxygen-rich compound, which is used as an oxygen source for various applications.[1] It plays an important role in air purification applications in sealed spaces, such as submarines, breathing apparatuses, and space capsules.[2,3] Li_2O_2 can absorb CO_2 and release O_2 from its reaction.[2] It is initially decomposed into Li_2O and O_2 at the temperature range of 340–348 °C.[4] Importantly, Li_2O_2 is a discharged product of aprotic cells that is formed in the cathode of the lithium–air battery. This material has been studied in various contexts because the formation of Li_2O_2 blocks the recharging capability, which is responsible for the reduction in the lifetime and cyclability of the lithium–air battery.[5] At ambient conditions, Fehér *et al.*[6] and Föppl[7] proposed hexagonal structures of Li_2O_2 with the same space group ($P\bar{6}$), but the lattice parameters and atomic positions of both reports were different. Cota *et al.* have confirmed the stability of those structures and optimised them using density functional theory calculations.[8] They found that the optimised structure has lattice constants: a = 3.1830 Å and c = 7.7258 Å, which is a hexagonal structure with the $P6_3/mmc$ space group and corresponds to the structure proposed by Föppl. Moreover, Chan *et al.* have used the Rietveld refinement with the high-energy X-ray diffraction data and first-principles non-resonant inelastic X-ray scattering (NIXS) spectra to propose that $P6_3/mmc$ is the most compatible structure for Li_2O_2.[9] For previous high-pressure studies, Deng *et al.* have predicted the crystal structures of Li_2O_2 in the pressure range of 0–100 GPa using the particle swarm optimization algorithm (CALYPSO code). They used the Perdew–Burke–Ernzerhof (PBE) functional as implemented

[a] *Extreme Conditions Physics Research Laboratory (ECPRL), Physics of Energy Materials Research Unit, Department of Physics, Faculty of Science, Chulalongkorn University, Bangkok 10330, Thailand. E-mail: thiti.b@chula.ac.th; Fax: +66 (0)22531150; Tel: +66 (0)22187554*

[b] *Department of Physics, Mahidol Wittayanusorn School, Nakhon Pathom 73170, Thailand*

[c] *Thailand Center of Excellence in Physics, Commission on Higher Education, Bangkok 10400, Thailand*

[d] *Center of Excellence on Catalysis and Catalytic Reaction Engineering, Department of Chemical Engineering, Chulalongkorn University, Bangkok 10330, Thailand*

[e] *Condensed Matter Theory Group, Department of Physics and Astronomy, Uppsala University, Box 516, S-75120 Uppsala, Sweden*

[f] *Applied Materials Physics, Department of Materials and Engineering, Royal Institute of Technology (KTH), S-100 44 Stockholm, Sweden*

† Electronic supplementary information (ESI) available: The structural parameters of the various structures at different pressures; the Mulliken charges of the Li and O atoms at different pressures; the plot of the lattice parameters and interatomic distances *versus* pressure; the phonon dispersion curves and partial phonon density of states (PDOSs) for the $P2_1/c$ structure at pressures of 75, 150, 300, and 500 GPa; the phonon dispersion curves and PDOSs for the $P2_1/c$ and $P2_1/c^{\dagger}$ structure at 150 GPa; the plot of the ELF isosurface value for the $P6_3/mmc$ structure; the density of states of Li and O at 5, 8, 11, 14, 38, 39, 40, and 41 GPa; the electron density maps and ELF for the various structures of Li_2O_2; the crystal structures of Li_2O_2 for three phases at different pressures. See DOI: 10.1039/c7cp07293g

in the VASP (Vienna *Ab initio* simulation package) code to optimise the crystal structures and calculate electronic properties. They reported that the hexagonal structure ($P6_3/mmc$) of Li_2O_2 transforms to a monoclinic structure ($P2_1/c$) at a pressure around 84 GPa. The band gap of Li_2O_2 has also been reported, which increases with increasing pressure.[10] Furthermore, Radin *et al.* reported that the stable surfaces of Li_2O_2 are half-metallic, whereas bulk Li_2O_2 is an insulator.[11] Recently, Dunuwille *et al.* have studied the crystal structure of Li_2O_2 up to 63 GPa using confocal micro-Raman spectroscopy and synchrotron X-ray diffraction. They found that the $P6_3/mmc$ structure is maintained at 63 GPa.[12] Very recently, Yang *et al.* have also investigated the structural stability of pure Li_2O_2 under high pressure at room temperature using XRD measurement. They found that Li_2O_2 is robustly stable up to 57 GPa.[13] In addition, the formation of holes in Li_2O_2 has been proposed by previous studies.[14–16] Hummelshøj *et al.* found that the lithium vacancies induced the formation of holes in the valence band of Li_2O_2.[14] Similarly, Ong *et al.* have also reported that a hole is formed in the π^* antibonding molecular orbital of the peroxide anion and proposed that the trapped hole can induce the local lattice distortion.[15] Besides, Garcia-Lastra *et al.* have analyzed the partial density of states of Li_2O_2 using the G_0W_0-corrected PBE calculations. They also found that a hole was formed in the π^* (p_x and p_y antibonding orbitals) antibonding orbital of the peroxide anion, which formed narrow bands at the top of the valence band. Furthermore, the π^* and σ^* (p_z antibonding orbital) orbitals of the peroxide anion mainly contributed in the valence and conduction bands, respectively, with a small contribution of the Li states.[16] These results indicate the existence of local distortion in the Li_2O_2 lattice.

The previous studies suggested that understanding of the structure and thermodynamic stability for Li_2O_2, Li_2O, and LiO_2 are fundamental for improving the performance of the lithium–air battery.[13,17] However, there are some issues for Li_2O_2 under high pressure that would need more investigation. For example, the effect of the local lattice distortion on the chemical bonding and electronic properties is not clarified, and its high-pressure phase transition pathway beyond the valid pressure is still incomplete. Therefore, we have used *ab initio* calculations based on density functional theory (DFT) formalism to investigate the detail of the structural phase transitions of defect-free Li_2O_2 under high pressure. The related properties including electronic band structure, phonon dispersion, O–O bond length, and electron localization function (ELF) have also been calculated. In addition, an evolutionary algorithm has been used to search for the higher pressure structures of Li_2O_2 up to 500 GPa to extend its transformation pathway.

2 Computational methods

A systematic *ab initio* evolutionary crystal prediction implemented within the USPEX (Universal Structure Predictor: Evolutionary Xtallography) code,[18,19] which interfaces to the VASP code with the PAW method,[20,21] has been used to search the global structures of Li_2O_2 at given pressures up to 500 GPa (*i.e.*, 0, 50, 100, 200, 300, and 500 GPa). The searches have been performed by varying the cell size up to 4 formula units (f.u.) per cell (consisting of 8 Li and 8 O atoms). During the prediction, the number of initially randomized structures in the first generation was set at 30 structures. The next generation carried out 20 population structures using heredity and the mutations of the two lowest enthalpy structures of the previous generation by 60% and 20%, respectively, and the remaining 20% of the populations were obtained by randomisation. The searches would be done when the lowest enthalpy structure continuously survived within 25 generations. Then, the crystal structures obtained from the prediction at each pressure would be fully optimised by setting up a more accurate criterion. Structural optimisation was performed at pressures ranging from 0 to 500 GPa using an *ab initio* total energy calculations program, as implemented in the CASTEP (Cambridge Serial Total Energy Package) code.[22] All optimisation would employ the BFGS algorithms,[23] the PBE exchange–correlation functional,[24] and the ultrasoft pseudopotentials[25] for Li: $1s^2 2s^1$ and O: $2s^2 2p^4$, which is implemented in the CASTEP code.[22] The plane-wave kinetic energy cutoff of 700 eV and Monkhorst–Pack grid spacing of $0.04 \times 2\pi$ Å^{-1} were used. The tolerance of calculation was set to 1.0×10^{-6} eV per atom for energy and 1.0×10^{-4} eV Å^{-1} for maximum force. The electronic band structure and partial density of states have been calculated using the PBE[24] and HSE06[26] functionals. To obtain the equation of state parameters, the total energy (E) *versus* unit cell volume (V) relations of the various structures were fitted using the third-order Birch–Murnaghan equations of state.[27] Thus, the enthalpy (H) for the structure under pressure (P) can be calculated by the formula: $H = E + PV$. The dynamic stabilities of the calculated crystal structures, which are interpreted from the behaviour of phonon dispersion, have been performed using supercell and finite displacement approaches, as implemented in the Phonopy code.[28] VESTA software has been used for visualizing and analyzing the crystal structure.[29]

3 Results and discussion

3.1 Crystal structure prediction

From the structural searching results for Li_2O_2 up to 500 GPa, the lowest enthalpy structures at different pressures have been found. At 0 and 50 GPa, the $P6_3/mmc$ structure with 2 and 4 f.u. per cell has a lower enthalpy than the $P\bar{1}$ structure (1 and 3 f.u.). This finding is in agreement with the previous experimental results revealing that the $P6_3/mmc$ is stable up to 63 GPa.[12,13] Interestingly, the $P2_1$ (2 and 4 f.u.) structure has been found at 100 GPa, which has a lower enthalpy than the $P2_1/c$ (2 and 4 f.u.) and $C2/m$ (1 f.u.) structures at the same pressure. However, the $P2_1$ structure is not found at 200 GPa while the $P2_1/c$ (2 f.u.) structure is still maintained up to 500 GPa. This result suggests that the $P2_1$ would probably be transformed to be the $P2_1/c$ structure within a pressure range of 100–200 GPa.

3.2 Structural phase transitions

The structural searching results show that the hexagonal structure ($P6_3/mmc$) of Li_2O_2 with 2 f.u. at ambient pressure and zero

temperature is the lowest enthalpy. The relaxed lattice constants are a = 3.1858 Å and c = 7.7182 Å, which are in agreement with the experimental values of 3.1692 and 7.7140 Å[9] and the previous calculation values of 3.1830 and 7.7258 Å.[8] In order to investigate the structural phase transition of Li_2O_2 in the pressure range of 0–500 GPa, the enthalpy differences of the calculated structures *versus* pressure with respect to the $P2_1/c^\dagger$ structure predicted by Deng *et al.*[10] is shown in Fig. 1(a). The $C2/m$ structure appears at very low pressure, and it disappears at a higher pressure. This is because the $C2/m$ enthalpy is lower than that of the $P2_1/c^\dagger$ structure about 20 meV f.u.$^{-1}$ at ambient pressure, and its enthalpy becomes larger than that of the $P2_1/c^\dagger$ structure about 58 meV f.u.$^{-1}$ at 100 GPa (not shown). The first structural phase transition, which is that of the ambient phase, $P6_3/mmc$, is calculated at 75 GPa and transforms to another one as justified by the thermodynamic stability. The candidates at this pressure consist of the $P2_1$ and $P2_1/c$ structures with a small energy difference, which is due to the fact that they also have a very similar atomic configuration. According to the structure searching result, the $P2_1$ structure is not found at 200 GPa and the dynamical instability of the $P2_1$ structure occurs at 150 GPa due to the observation of a few negative phonon frequencies around the Γ-point (see Fig. 5(b)). Therefore, we refitted and plotted the enthalpy of the $P2_1$ structure with respect to the $P2_1/c$ structure *versus* the pressure range of 50–150 GPa, as shown in Fig. 1(b), to verify which structure is the more stable one. Around 75 and 135 GPa, the enthalpies of both structures are indistinguishable. However, at 100 GPa, the $P2_1$ structure is more stable than the $P2_1/c$ structure due to having a different enthalpy of 2 meV f.u.$^{-1}$. This finding corresponds to the structure searching result. In addition, the $P2_1$ enthalpy is initially higher than the $P2_1/c$ enthalpy around 136 GPa and increases to 2 meV f.u.$^{-1}$ at 150 GPa. These findings indicate that the $P2_1$ structure may exist in the pressure range of 75–135 GPa and transforms to the $P2_1/c$ structure at pressures beyond 136 GPa. Thus, it is possible to note that the first structural phase transition occurs at 75 GPa, $P6_3/mmc \rightarrow P2_1$, and the second transition pressure is above 136 GPa, $P2_1 \rightarrow P2_1/c$.

By increasing the pressure, we found that the z-coordinate of the O atom (O_z) for the $P6_3/mmc$ structure was displaced and the O–O bond length decreased with the increasing pressure, as shown in Fig. 2(a) and (b), respectively. Surprisingly, the O_z and O–O bond length significantly changed at pressures around 11 and 40 GPa. The atomic displacement of O_z from 10 GPa to 11 GPa is about 0.0057 Å, which is double its displacement on the trend line at 11 GPa. Likewise, the displacement of the O_z from 39 GPa to 40 GPa is 0.0031 Å, which is twice its displacement on the trend line at 40 GPa, resulting in the O–O bond length increase of about 0.0024 Å at 11 GPa and 0.0017 Å at 40 GPa with respect to its bonds at 10 and 39 GPa, respectively. These results are in line with the experimental results at ambient temperature proposed by Dunuwille *et al.*[12] To investigate this situation, we evaluated the length of c, a, and the c/a ratio *versus* pressure and then considered the change in the interatomic distances of Li(1)–O(1), Li(2)–O(1), and Li(1)–Li(2). We found that the c/a ratio is abnormally collapsed around 11 and 40 GPa (see Fig. 2(b)) because the lattice constant c has a higher reduction rate than that of lattice constant a (Fig. S1, ESI†). The lattice constant c at 11 GPa deviates from its constant at the same pressure on the trend line about 0.018 Å and 0.009 Å at 40 GPa. In the same way, the reduction of lattice constant c from 10 GPa to 11 GPa is twice its constant from 39 GPa to 40 GPa like the reduction of the lattice constant a. In order to investigate the drastic shortening of the c-axis and the increased O–O bond lengths at 11 and 40 GPa, the electron localization function (ELF) of the $P6_3/mmc$ structure has been calculated in the pressure range of 0–70 GPa. We found that the ELF isosurface values of the peroxide anion increase within the pressure ranges of 8–11 and 39–40 GPa (see Fig. S7(b), ESI†) resulting in the softening of the O–O bond. When the O–O bonds along the c-axis soften, the c-axis weakens as well. Moreover, this collapses will have also significantly influenced the change in the interatomic distances of Li(1)–O(1), Li(2)–O(1), and Li(1)–Li(2) around 11 and 40 GPa, as shown in Fig. S2 (ESI†). These results

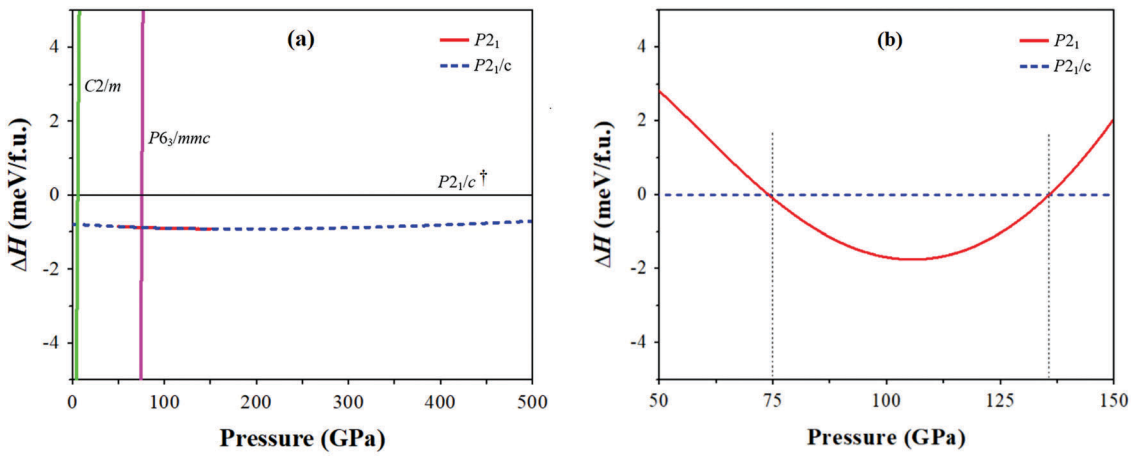

Fig. 1 (a) The enthalpy differences of the various structures with respect to the $P2_1/c$ structure predicted by Deng *et al.*[10] (denoted as $P2_1/c^\dagger$ hereafter) in the pressure range of 0–500 GPa. (b) The enthalpy difference of the $P2_1$ structure with respect to the $P2_1/c$ structure in pressures ranging from 50 to 150 GPa. The vertical dashed lines represent the pressures at 75 and 135 GPa, respectively.

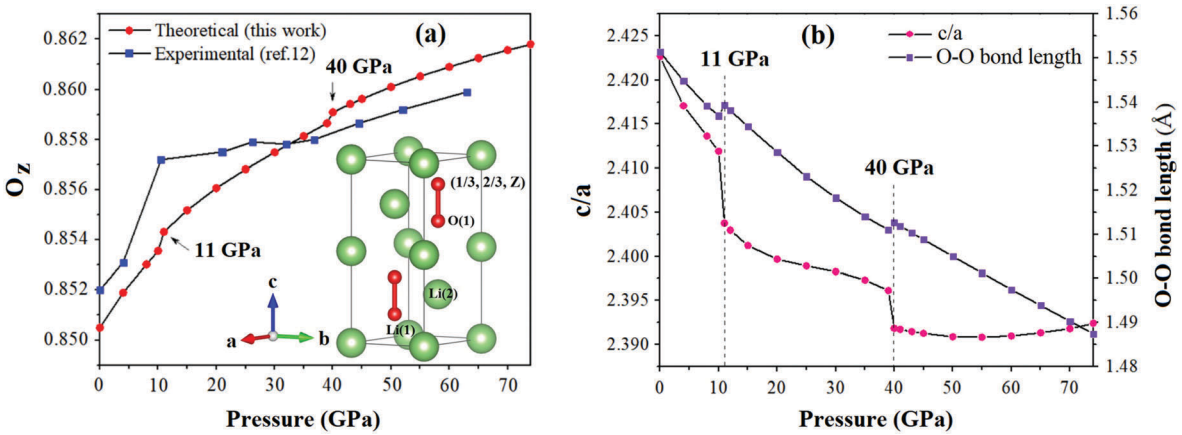

Fig. 2 (a) The plot of the z-coordinate of the O atom (O_z) *versus* the pressure range of 0–74 GPa compared with the experimental results proposed by Dunuwille *et al.*[12] (b) The c/a ratio and O–O bond length in the $P6_3/mmc$ structure *versus* the same pressure range.

show the existence of displacement in the O_z. Likewise, Wu *et al.* have also reported a small anisotropic compressibility in the $P6_3/mmc$ structure of Li_2O_2. It is found that the bulk modulus along the c-axis (B_c) is higher than that along the a-axis (B_a) at zero pressure ($B_a/B_c = 0.589$) and, for that reason, the O–O bond along the c-axis is stronger than the Li–Li and Li–O bonds.[30] However, our results suggest that the bulk modulus along the c-axis is lower than that along the a-axis in the pressure ranges of 10–11 GPa and 39–40 GPa. In addition, Dunuwille *et al.* have also reported the fluctuation in the c/a ratio,[12] but an unusual collapse in the c/a, like our result, is not proposed. Thus, these results exhibit that the displacement in the O_z causes the dramatic collapse in the c/a ratio of the $P6_3/mmc$ structure.

At the transition pressure of 75 GPa, the Li and O atoms in the $P6_3/mmc$ structure move to the new atomic positions in the $P2_1$ structure as shown in Fig. 3(b). The O–O bond length of 1.4592 Å and volume of the $P2_1$ structure are reduced by 1.85 and 2.87% from those of the $P6_3/mmc$ structure, respectively. The average of the six nearest-neighbour Li–O distances (1.8335 Å) in the $P2_1$ structure is longer than that of the distance (1.8080 Å) in the $P6_3/mmc$ structure. Therefore, the phase transition at 75 GPa demonstrates that the electrostatic interaction between the Li and O atoms was decreased. Correspondingly, the ionicity of the $P2_1$ structure is less than that of the $P6_3/mmc$ at 75 GPa (see Table S2, ESI†). Moreover, the alignment of the peroxide anions in the $P2_1$ structure is tilted from the c-axis in the $P6_3/mmc$ structure about 20 degrees. In addition, the first structural phase transition has a significant difference with the previous predicted structure, that is the $P6_3/mmc$ structure transforms to the monoclinic ($P2_1/c^{\dagger}$) structure at around 84 GPa. However, the $P2_1$ enthalpy is lower than that of the $P2_1/c^{\dagger}$ structure about 1 meV f.u.$^{-1}$ at 75 GPa, which might be significant at extremely low temperature. Consequently, the $P2_1$ structure should be a high-pressure phase of Li_2O_2 rather than the $P2_1/c^{\dagger}$ structure because the $P2_1$ structure has a lower enthalpy. The structural parameters of the $P6_3/mmc$, $P2_1$, $P2_1/c$, and $P2_1/c^{\dagger}$ structures are demonstrated in Table S1 (ESI†).

For the second structural phase transition, the Li and O atoms in the $P2_1$ structure move to the new atomic positions in

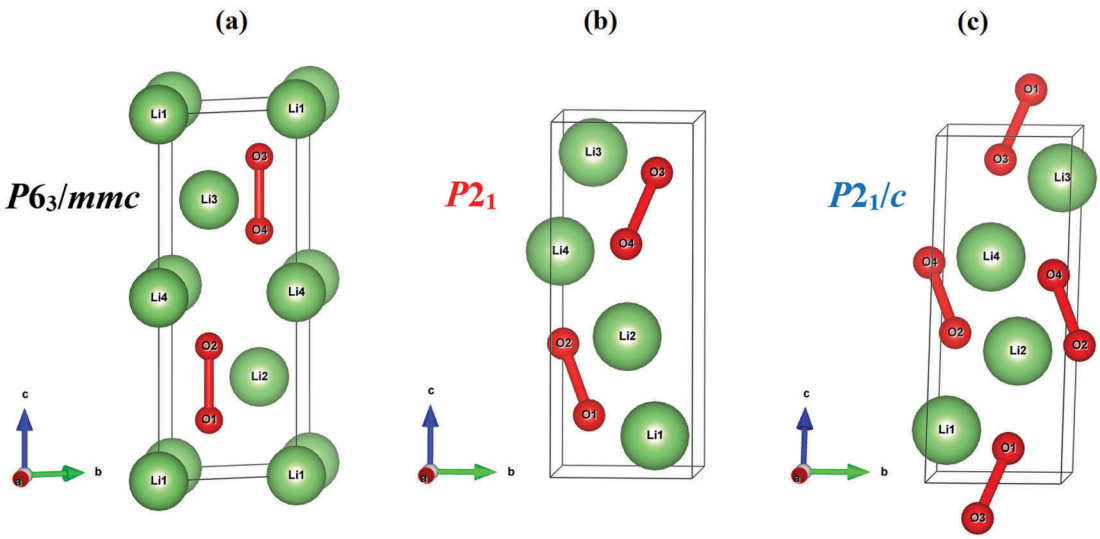

Fig. 3 The crystal structure of Li_2O_2 for the three phases: (a) $P6_3/mmc$ at 0 GPa, (b) $P2_1$ at 75 GPa, and (c) $P2_1/c$ at 136 GPa.

the $P2_1/c$ structure (see Fig. 3(c)). The O–O bond length and volume of the $P2_1/c$ and $P2_1$ structures at 136 GPa are insignificantly different. Similarly, the average of the six nearest-neighbour Li–O distances (1.7513 Å) in the $P2_1/c$ structure is insignificantly different to that of the distance (1.7512 Å) in the $P2_1$ structure. However, the peroxide anions are aligned on the (100) plane of the $P2_1/c$ structure, which tilted from the alignment in the $P2_1$ structure about 22 degrees. In addition, we found that the $P2_1/c$ enthalpy is slightly less than that of the $P2_1/c^{\dagger}$ structure about 1 meV f.u.$^{-1}$. In order to compare the structures, we have transformed the $P2_1/c$ structure to the most similar configuration of the $P2_1/c^{\dagger}$ structure using the COMPSTRU programme proposed by Flor *et al.*[38] The findings show that the $P2_1/c$ and $P2_1/c^{\dagger}$ structures at 150 GPa are different with the measurement of similarity (Δ) of 0.445.

In order to investigate the driving force for the structural transitions, we have plotted the normalized lattice constants, angle between the *a*- and *c*-axes (β), and interatomic distances *versus* pressure (0–500 GPa) for the $P6_3/mmc$, $P2_1$, and $P2_1/c$ structures, as shown in Fig. S3 (ESI†). The lattice constants a_0, b_0, and c_0 represent the lattice parameters of the $P6_3/mmc$ structure at ambient pressure. At the transition pressure of 75 GPa, the *a*- and *b*-axes are collapsed compared to the *c*-axis because the O–O bonds along the *c*-axis are stronger than the interactions of Li–Li in the *ab*-plane. Moreover, Fig. S3(c) (ESI†) demonstrates the dramatic reductions in the Li(1)–Li(2) and Li(2)–Li(2) distances upon the $P6_3/mmc$ to $P2_1$ phase transition, which links to the alignment of the Li atoms in the $P2_1$ phase compared to the alternate stacking of the Li atoms in the $P6_3/mmc$ phase. The arrangement of the atoms in the $P6_3/mmc$ phase can be described as AcBcAbCbA, where the capital and small letters represent the Li and O atoms, respectively.[8] Therefore, the driving force of the phase transition at 75 GPa is dictated by the alignment of the Li atoms in the $P6_3/mmc$ phase resulting in the changes in the lattice parameters. For the $P2_1$ to $P2_1/c$ phase transition at 136 GPa, the *a*- and *b*-axes continuously decrease, yet the *c*-axis dramatically increases like β. Furthermore, unusual changes occur in the Li(1)–Li(2) and Li(2)–Li(2) distances. These suggest that the driving force of the $P2_1$ to $P2_1/c$ transition is controlled by the alignment of the Li atoms in the $P2_1$ phase as well.

By considering the local distortion that occurred within the O–O units in the 75–500 GPa pressure range, the atomic displacement occurs in the *xyz* coordinates of the Li and O atoms (see Table S1, ESI†) and results in the O–O units tilting from the *c*-axis by angles of about 20, 22, 23, and 25 degrees at 75, 150, 300, and 500 GPa, respectively. For the evolution of the Li–O coordination, we found that the Li atom is coordinated to the six neighbouring O atoms at the same distance of 1.9962 Å, but the O atoms in the peroxide anion are coordinated to the six neighbouring Li atoms with distances of 2.1713 Å for O–Li(1) and 1.9962 Å for O–Li(2) at ambient pressure. At 74 GPa, these distances are changed to 1.8503 Å and 1.7695 Å, respectively. That is, the distances are reduced by 14.78% for O–Li(1) and 11.36% for O–Li(2). In addition, in the 75–500 GPa pressure range, the coordination numbers of the six Li and O atoms are the same with differences in the Li–O distances, such as 1.7769, 1.8481, 1.8224, 1.8629, 1.8374, 1.8533 Å at 75 GPa and 1.5609, 1.5487, 1.5539, 1.5541, 1.5593, 1.5735 Å at 500 GPa. These distances are reduced by 12.16, 16.20, 14.73, 16.58, 15.13, and 15.10%, respectively. It indicates that the Li–O coordination is strongly distorted with large variations of the individual Li–O distances within the same polyhedron and demonstrates the anisotropic distortion in the $P2_1$ and $P2_1/c$ phases of Li_2O_2.

3.3 Phonon dispersion and partial phonon density of states

To investigate the dramatic change of the O–O bond lengths at pressures of 11 and 40 GPa in the $P6_3/mmc$ structure, as reported before, we have analyzed the partial phonon density of states (PDOSs) at pressures of 10, 11, 12, 39, 40, and 41 GPa, respectively. These PDOSs are shown in Fig. 4. The highest frequency phonon modes at a maximum density of phonon states, which represent the O–O stretching modes, are 24.13, 24.00, 24.10, 26.63, 26.56, and 26.65 THz, respectively. That is, at 11 and 40 GPa, the frequency of the O–O stretching modes significantly decreases and then increases by compression.

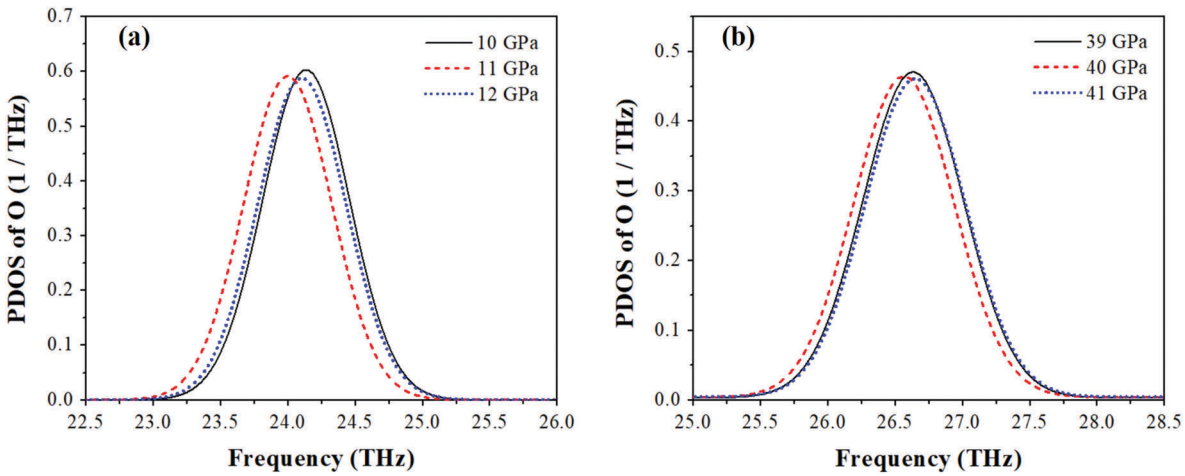

Fig. 4 The partial phonon density of states (PDOSs) of the O–O stretching modes for the $P6_3/mmc$ structure at: (a) 10–12 GPa and (b) 39–41 GPa.

This result confirms the existence of the abnormal changes in the O–O bond length of the $P6_3/mmc$ structure. Therefore, it is important to note that the pressures of 11 and 40 GPa soften the O–O bonds.

In order to verify the dynamic stability of the predicted structures ($P2_1$ and $P2_1/c$), we have calculated the phonon dispersion and PDOSs. We found that the phonon spectrum of the $P2_1$ has no imaginary phonon frequency at 75 GPa (Fig. 5(a)), but it has a few negative frequencies around the Γ-point at 150 GPa (Fig. 5(b)). This indicates that the $P2_1$ structure is dynamically stable at 75 GPa, but it is not stable at 150 GPa. For the $P2_1/c$ structure, we have also verified the dynamic stability at pressures of 75, 150, 300, and 500 GPa (see Fig. S4(a)–(d), ESI†), respectively. The phonon spectra of the high-pressure phases show the highest frequency phonon modes, which are mainly dominated by the O–O stretching modes. We found that the highest frequency phonon modes increase with increasing pressure from ~32 THz (1067 cm^{-1}) at 75 GPa to ~49 THz (1635 cm^{-1}) at 500 GPa. However, the Li_2O_2 stability has been confirmed with respect to the decomposition into Li_2O and O_2 in the pressure range of 0–100 GPa by Deng *et al.*[10] With the phonon dispersion and PDOSs in Fig. 5 and Fig. S4 (ESI†), a gap separating the low and high-frequency regimes appears at 75 GPa, and it is then decreased by further compression. The frequency gap that represents the characteristic decoupling of the peroxide anions from the rest of lattice[31] appears in the $P6_3/mmc$ and $P2_1$ phases. Lau *et al.*[17] reported that the frequency gap of the $P6_3/mmc$ phase at ambient pressure is about 16–23 THz. We believe that it also decreases by increasing pressures as appears in the $P2_1$ phase. Due to the pressure inducing increase in the electrostatic interaction of Li–O resulting in the Li–O phonon coupling, which contributes to a broader frequency range, the gaps could be decreased by compression.

To distinguish between the $P2_1/c$ and $P2_1/c^\dagger$ structures, we have compared their phonon spectra at the same pressure of 150 GPa (Fig. S5, ESI†). We have used an equivalent structure of the $P2_1/c^\dagger$ as the same Brillouin zone path in the calculations. The differences of phonon dispersion between the two structures are presented in the *Y–A* and *E–C* paths. The peak of the oxygen PDOSs of the $P2_1/c$ structure is slightly higher than the peak of the $P2_1/c^\dagger$ structure. Accordingly, it is sufficient to note that the $P2_1/c$ and $P2_1/c^\dagger$ structures are significantly different.

3.4 Electronic properties

To investigate the electronic band structure of Li_2O_2 under high pressure, we have calculated the band structures and partial density of states (PDOSs) using GGA-PBE as implemented in the CASTEP code. The band gaps have also been calculated using the hybrid functional, HSE06, implemented within the VASP code,[25] which is well-known to provide a more reliable quantity of band gap than that using the conventional functionals: GGA and LDA. Fig. 6(a) shows the PBE and HSE06 band gaps of various structures of Li_2O_2 in the pressure range of 0–500 GPa. At ambient pressure, the PBE band gap (2.05 eV) is lower than the band gap (4.18 eV, α = 0.25) calculated by the HSE06. Nevertheless, our result is in good agreement with other calculated band gaps predicted using the PBE, HSE06, G_0W_0, and scGW methods (1.99, 4.19, 5.15, 6.37 eV).[32] By increasing the pressure, the calculated band gaps of all three structures using both methods increase by the same trends. At the first transition pressure (75 GPa), the PBE band gap of $P2_1$ (3.43 eV) is higher than the $P6_3/mmc$ band gap (2.60 eV) of about 0.8 eV. Similarly, the HSE06 band gap of $P2_1$ (5.70 eV) is higher than the $P6_3/mmc$ band gap (4.98 eV) of about 0.7 eV. In the pressure range of 75–125 GPa, the maximum difference in the PBE band gap between the $P2_1$ and $P2_1/c$ structures is approximately 5 meV. It is a very small difference, but the trend line of the HSE06 band gap (dashed line in Fig. 6(a)) implies the significant difference between the $P2_1$ and $P2_1/c$ band gaps. These findings insist that the tendency of band gaps calculated by the PBE functional would be reliable as well. Therefore, henceforth, the electronic band structures calculated using the PBE functional would be mainly discussed and the effects of pressure on the structural evolutions in Li_2O_2 monitored. In addition, we have compared the HSE06 band gap between the $P2_1/c$ and $P2_1/c^\dagger$ structures at 150 GPa. It is found that the HSE06 band gap of the $P2_1/c$ is less than that of the $P2_1/c^\dagger$ structure about 0.18 eV. This confirms the difference between the $P2_1/c$ and $P2_1/c^\dagger$ structures. Intriguingly, in the $P6_3/mmc$ structure, we found that the band gap has been significantly reduced by increasing the pressure at around 11 and 40 GPa, as shown in Fig. 6(b). The PBE band gaps reduce about 0.01 and 0.02 eV at 11 and 40 GPa with respect to the band gap at 10 and 39 GPa, respectively. Expectedly, by observing the O–O bond length in the 0–75 GPa pressure range, we found that the band

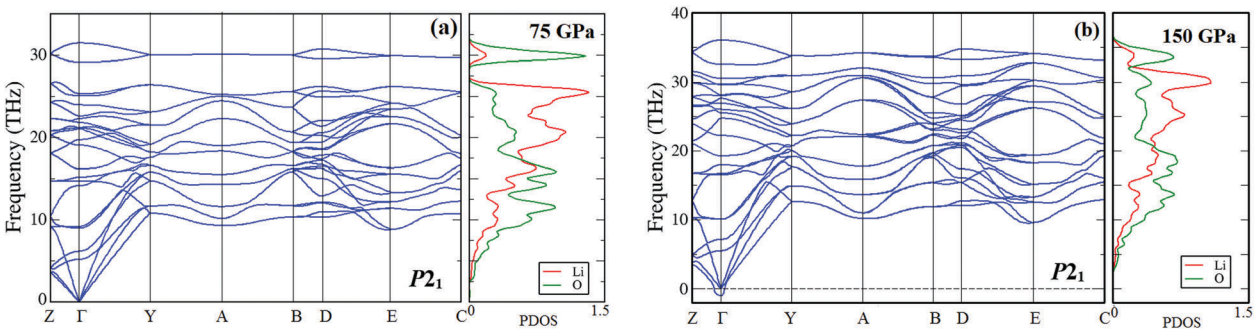

Fig. 5 The phonon dispersion curves and partial phonon density of states (PDOSs) for the $P2_1$ structure at: (a) 75 GPa, and (b) 150 GPa.

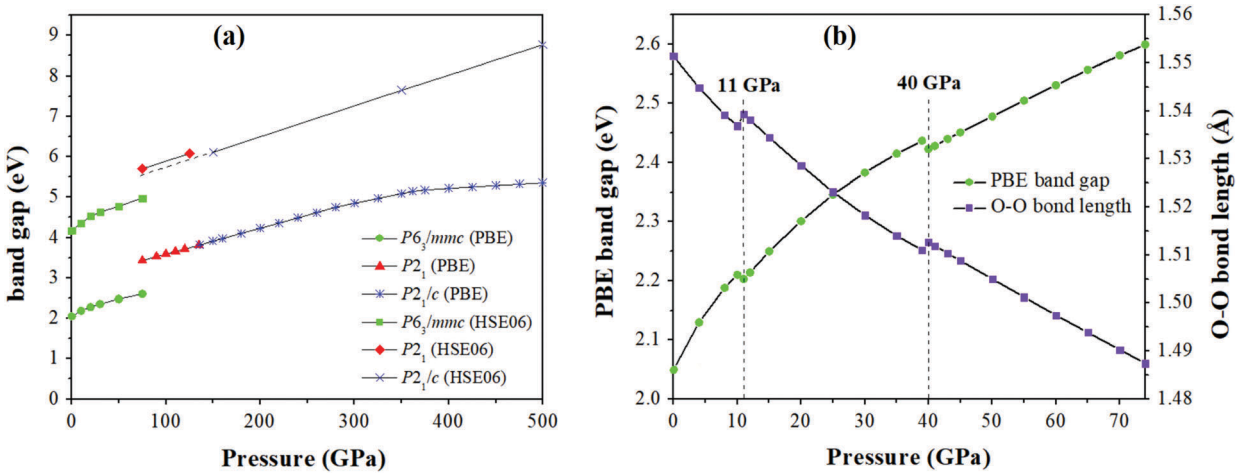

Fig. 6 (a) The PBE and HSE06 band gaps *versus* pressure for the $P6_3/mmc$, $P2_1$, and $P2_1/c$ structures. (b) The plot of the $P6_3/mmc$ band gap (PBE) and O–O bond length *versus* pressure (0–74 GPa).

gap increases with decreasing the O–O bond length. That is because the band gap exhibits the energy difference between the top of the valence band and the bottom of the conduction band. In the case of Li_2O_2, the O–O bond in the peroxide anion relates to the p-state of O, which mainly contributes in the valence and conduction bands. When the O–O bond in the peroxide anion is decreased by compression, the electrons are more tightly bound to the atom so that it requires more energy to remove. Therefore, the shorter O–O bond length provides the wider band gap. These indicate that the band gap of Li_2O_2 directly depends on the O–O bond length. Moreover, the band gap suddenly decreases together with increasing the O–O bond length at pressures from 10 GPa to 11 GPa and 39 GPa to 40 GPa. These effects occur at the same pressures with a dramatic change in the c/a ratio as discussed before. Thus, it is obvious that the displacement in the z-coordinate of the O atoms results in a dramatic change of the band gap in the $P6_3/mmc$ structure.

Fig. 7 illustrates the electronic band structure and partial density of states (PDOSs) for the three phases of Li_2O_2 at different pressures. By considering the PDOSs, it is seen that both the valence and conduction bands of the three phases are mainly contributed by the p-states of O and a few partial

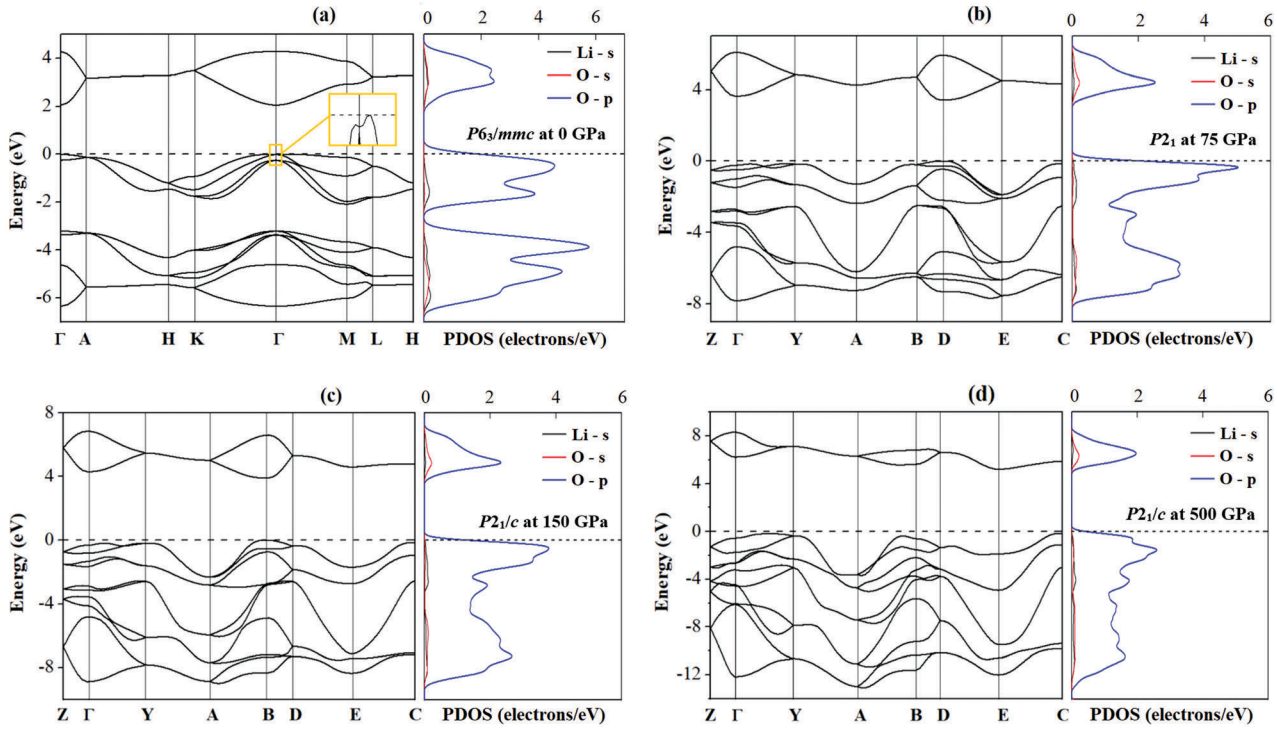

Fig. 7 The electronic band structure and partial density of states (PDOSs) for the structure of Li_2O_2: (a) the $P6_3/mmc$ structure at 0 GPa, (b) the $P2_1$ structure at 75 GPa, and (c and d) the $P2_1/c$ structure at 150 and 500 GPa, respectively. The dashed lines indicate the Fermi level, which is set to zero.

contributions of the s-state of Li are observed. The band structures of the $P6_3/mmc$ structure at ambient pressure (Fig. 7(a)) exhibit the direct band gap (2.05 eV) at the Γ-point of the Brillouin zone. Interestingly, by magnifying around the Γ-point, the valence band maximum (VBM) is not exactly at the k-point, yet it is a point within the Γ–M path with a distance of 0.660 beyond the Γ-point (see inset Fig. 7(a)). In the valence band of the high-pressure phases (see Fig. 7(b)–(d)), the conduction band has the main contribution in the p-states and small contribution in the s-state of O and a very small contribution in the s-states of Li. Furthermore, the band structures and PDOSs demonstrate that the valence band shifts to lower energy by increasing the pressure whereas the conduction band shifts to higher energy. That is why the band gaps increase with increasing pressure. In addition, the VBM of the $P2_1$ structure is at the D-point of the Brillouin zone until the transition pressure is reached, but the VBM of the $P2_1/c$ structure has changed from the B-point (~150–280 GPa) to the C-point (~280–500 GPa) of the Brillouin zone. These results obviously support the distortion of the Li_2O_2 lattice under high pressure, which corresponds to the changes in the atomic positions of Li_2O_2 under pressure (see Table S1, ESI†).

For the s-states of Li, the valence band energies decrease with increasing pressure, except at energy around −4.9 eV (see Fig. S6(a)–(e), ESI†). The DOSs in the band energies of −3 to 0 eV decrease while the band energies of −8 to −3 eV increase, except at energy of about −5.9 eV for 38–41 GPa (Fig. S6(e), ESI†). Unusually, the DOSs at energy around −4.2 eV decreases at 5–8 GPa, but it increases at 8–11 GPa, and the energy shifts down about 0.04 eV (Fig. S6(b), ESI†). Conversely, the DOSs at energy of about −4.9 eV at 39–40 GPa increases to double that of the change at 38–39 GPa, and the energy shifts up about 0.02 eV (Fig. S6(d), ESI†). In the same way, the DOSs at energy of about −5.9 eV at 39–40 GPa decreases to double that of the change at 38–39 GPa, and the energy shifts up about 0.01 eV (Fig. S6(e), ESI†). Due to the energy step in the DOSs being 0.01 eV, this energy change is significant. Similarly, the band energies of the s-states of O decrease with increasing pressure, except at energy around −4.9 eV (see Fig. S6(f)–(j), ESI†). The DOSs at energy around −4.2 eV increase with increasing pressure and the change of the DOSs at 8–11 GPa increases to double that of the change at 5–8 GPa, and the energy shifts down about 0.04 eV. (Fig. S6(g), ESI†). Moreover, the DOSs at energy of −4.9 eV at 39 GPa is less than that at 40 GPa about 0.03 eV, but the change in the DOSs is very small (Fig. S6(i), ESI†). In addition, the DOSs at energy around −5.8 eV at 39–40 GPa decreases to double that of the change at 38–39 GPa, but the energy change is insignificant (Fig. S6(j), ESI†). For the p-states of O, the energies in the valence bands and their DOSs decrease with increasing pressure (see Fig. S6(k)–(q), ESI†). Due to the valence and conduction bands of the s-state of Li and the s- and p-states of O almost entirely overlapping, forming the σ-bond in Li_2O_2, it is possible to transfer electrons between the states of Li and O at the same energy level. As a result, the significant changes of the DOSs suggest that the transfer of electrons between the states of Li and O likely occur at the pressure ranges of 8–11 GPa and 39–40 GPa because the increase and decrease in the DOSs of Li and O are similar, and it occurs at the same energy level.

In the case of the conduction bands (see Fig. S6(a), (c), (f), (h), (k)–(m) and (r), ESI†), the DOS energies of the s-states of Li and O and the p-states of O (except at 11 and 40 GPa) shift up with increasing pressure, but the DOS energies of the p-states of O at the bottom band shift down about 0.002 eV for 8–11 GPa and 0.01 eV for 39–40 GPa (Fig. S6(l) and (r), ESI†). Although the energy shifts are very small, the top valence bands shift to lower energies with increasing pressure as well. The result is the significant energy differences represented by the band gaps. Therefore, these lead to the decreasing band gaps at 11 and 40 GPa. Furthermore, the DOSs of the energies around 3.2 eV anomalously increase about 0.028 for 8–11 GPa as the DOSs around 3.4 eV increase about 0.014 for 39–40 GPa. This implies that the electrons occupied the conduction bands at 11 and 40 GPa more. The conduction band of Li_2O_2 represents the σ_p^* antibonding states of the peroxide anion.[16,39] Kang *et al.* have suggested that the molecular nature of the σ_p^* states brings about the characteristic electron lattice interaction in Li_2O_2, which conducts a delocalized electron in the σ_p^* states that is unstable against the formation of a small polaron. They found that the presence of an excess electron in Li_2O_2 leads to elongation of the O–O bond and results in it being less stable than that case with the polaron state.[39] Therefore, these support that if the delocalized electron occurs in the conduction band of the defect-free Li_2O_2, the σ_p^* antibonding of the peroxide anion is strengthened, resulting in weakening of the O–O bonds at 11 and 40 GPa.

In order to investigate the charge transfer in the $P6_3/mmc$ structure, we have performed the Mulliken population analysis as implemented in the CASTEP.[33,34] We found that the Mulliken charges of Li(1)–Li(2) are $0.99|e|$, $0.77|e|$ for Li(3)–Li(4) and $-0.88|e|$ for O(1)–O(4) at ambient pressure, as shown in Table S2 (ESI†). These values are the same as reported by Deng *et al.*[10] Moreover, the structure of Li_2O_2 is anisotropic, that is the O atoms in the peroxide anion is coordinated to six neighbouring Li atoms with distances of 2.1713 Å for O–Li(1)/Li(2) and 1.9962 Å for O–Li(3)/Li(4) (see Fig. S10(a), ESI†). Therefore, the electrostatic interactions between O and Li for the O–Li(1)/Li(2) is stronger than that of the O–Li(3)/Li(4). These suggest that the atomic charges on the Li(1) and Li(2) are equal, but it is different to that of Li(3) and Li(4). Furthermore, we know that the Li and O atoms in Li_2O_2 have oxidation states of +1 and −1, respectively. So, it possible to note that the formation of Li_2O_2 has anisotropic charge transfers from O to Li: $-0.48|e|$ to Li(1)–Li(4); $-0.02|e|$ to Li(1)–Li(2), and $-0.46|e|$ for Li(3)–Li(4).

By increasing the pressure from 0 GPa to 70 GPa, the Mulliken charges of the O(1)–O(4) and Li(1)–Li(2) increase from $-0.88|e|$ to $-0.93|e|$ and $0.99|e|$ to $1.10|e|$, respectively. Conversely, the charges of the Li(3) and Li(4) decrease from $0.77|e|$ to $0.75|e|$. Moreover, the O–Li(1)/Li(2) and O–Li(3)/Li(4) distances change from 2.1713 Å and 1.9962 Å at ambient pressure to 1.8587 Å and 1.7763 Å at 70 GPa, respectively. These demonstrate that the electrostatic interactions between O and

Li for the O–Li(1)/Li(2) increase more than that of the O–Li(3)/Li(4) with the increasing pressure. Consequently, the pressure induces the changes in the electrostatic interactions of the O–Li(1)/Li(2) and O–Li(3)/Li(4) resulting in the variation in the Mulliken charges with pressure, which suggests charge transfers in Li_2O_2 under pressure. The pressure-dependent evolution of these charge transfers suggests that the Li_2O_2 compound is becoming more ionic. In order to measure the ionicity, we have calculated the effective ionic valence as proposed by Segall *et al.*, which is defined as the difference between the formal ionic charge and the Mulliken charge on the anion species in the crystal.[34] We found that the effective ionic valence is reduced from $0.12|e|$ at 0 GPa to $0.07|e|$ at 70 GPa, which indicates the increasing levels of ionic character. Unfortunately, we found that the resolution of the Mulliken charges calculation was not sufficient to distinguish the discontinuities at 11 and 40 GPa. That is the changes of the electron number in the PDOSs are less than 0.01 whereas the resolution of the Mulliken charges calculation is $0.01e$. However, we have described the anomalies at 11 and 40 GPa using the PDOS evolution with pressure as discussed before.

In addition, we not only found the transfer of charges in the $P2_1$ and $P2_1/c$ structures, we also found that the magnitude of the Mulliken charges of the O and Li atoms are the same, and it increases from $0.90|e|$ at 75 GPa to $0.95|e|$ at 500 GPa. This suggests that the oxidation state of the O atoms in the high-pressure phases approaches -1, supporting the stability of the peroxide group in Li_2O_2 under pressures of up to 500 GPa.

To investigate the effect of pressure on the chemical bonding of the $P6_3/mmc$ structure in the pressure range of 0–70 GPa, we have calculated the electron localization function (ELF)[35,36] as implemented in the CASTEP,[22] which provides a useful qualitative description of chemical bonding.[37] We found that the ELF isosurface value has a zig-zag feature with increasing pressure that it suddenly increases at the same range of the dramatic change in the O–O bond length and band gaps 8–11 GPa and 39–40 GPa as shown in Fig. S7(b) (ESI†). It demonstrates that the pressure induces the increase of electron localization resulting in the increase of the O–O bond lengths in the pressure range of 10–11 GPa and 39–40 GPa, and the change of the ELF value is significantly related to changing the DOSs of Li and O as well.

In addition, we have also plotted the electron density maps and ELFs of the $P6_3/mmc$, $P2_1$, and $P2_1/c$ structures at the pressures of 0, 75, 150, and 500 GPa, as shown in Fig. S8 and S9 (ESI†). The maps exhibit the O–O and Li–O bonds at the different pressures. The ELFs reveal that the electron is highly localized in the covalent bonds of the O–O peroxide group, which corresponds to the DOS results that the electrons mainly contribute in the p-states of O. These results confirm the existence of the peroxide group up to 500 GPa and clearly exhibit the Li–O and O–O single bonds, which illustrates the bonds in the three phases of Li_2O_2 structures (see Fig. S10, ESI†).

4 Conclusions

In this work, we have predicted the new structural phase transition and electronic properties of Li_2O_2 under pressures up to 500 GPa using first-principles calculations. The $P6_3/mmc \rightarrow P2_1$ and $P2_1 \rightarrow P2_1/c$ phase transitions have been predicted at pressures around 75 and 136 GPa, respectively. These structures have been confirmed by the dynamical stability seen in the phonon calculations. The ELF values exhibit the existence of the peroxide group in Li_2O_2 up to 500 GPa. We have reported that the pressure induces the O–O bond length, lattice dynamics, band gaps, and transfer of charges in Li_2O_2. Interestingly, we found that the $P6_3/mmc$ band gap and c/a ratio have dramatically collapsed with increasing the O–O bond lengths and ELF isosurfaces values of the peroxide group around 11 and 40 GPa. In addition, the PDOSs and Mulliken charges of the O and Li atoms demonstrate the transfer of charges between the O and Li atoms of Li_2O_2 in the $P6_3/mmc$ phase. The pressure-dependent evolution of these charge transfers suggests that the Li_2O_2 compound is becoming more ionic. These results reveal the mechanism for maintaining the structural stability under pressure by the atomic displacements in Li_2O_2. Our results provide understanding about the behaviour of the peroxide group, structures and electronic properties of Li_2O_2 under high pressure, which might be useful for investigating the charge transport through Li_2O_2 in the lithium–air battery and CO_2 capture.

Conflicts of interest

There are no conflicts to declare.

Acknowledgements

This research was funded by the Ratchadapisek Sompoch Endowment Fund (2016), Chulalongkorn University (CU59-003-IC). K. K. acknowledges support from the Thailand Research Fund (TRF) contract number TRG6080014. The SNIC and UPPMAX are acknowledged for partly providing computing time.

References

1 M. V. Aleinikova, Y. N. Zhuravlev and D. V. Korabelnikov, *Russ. Phys. J.*, 2012, **55**, 495–500.
2 U. Wietelmann and M. Steinbild, *Ullmann's Encyclopedia of Industrial Chemistry*, 2014, pp. 1–38.
3 N. N. Greenwood and A. Earnshaw, *Chemistry of the Elements*, Butterworth-Heinemann, Oxford, UK, 2nd edn, 1997.
4 R. A. Nefedov, Y. A. Ferapontov and N. P. Kozlova, *IOP Conf. Ser.: Mater. Sci. Eng.*, 2016, **112**, 012027.
5 G. Girishkumar, B. McCloskey, A. C. Luntz, S. Swanson and W. Wilcke, *J. Phys. Chem. Lett.*, 2010, **1**, 2193–2203.
6 F. Fehér, I. V. Wilucki and G. Dost, *Chem. Ber.*, 1953, **86**, 1429–1437.
7 H. Föppl, *Z. Anorg. Allg. Chem.*, 1957, **291**, 12–50.
8 L. G. Cota and P. de la Mora, *Acta Crystallogr., Sect. B: Struct. Sci.*, 2005, **61**, 133–136.
9 M. K. Y. Chan, E. L. Shirley, N. K. Karan, M. Balasubramanian, Y. Ren, J. P. Greeley and T. T. Fister, *J. Phys. Chem. Lett.*, 2011, **2**, 2483–2486.

10 N. Deng, W. Wang, G. Yang and Y. Qiu, *RSC Adv.*, 2015, **5**, 104337–104342.
11 M. D. Radin, J. F. Rodriguez, F. Tian and D. J. Siegel, *J. Am. Chem. Soc.*, 2012, **134**, 1093–1103.
12 M. Dunuwille, M. Kim and C. S. Yoo, *J. Chem. Phys.*, 2016, **145**, 084701.
13 W. Yang, D. Y. Kim, L. Yang, N. Li, L. Tang, K. Amine and H. K. Mao, *Adv. Sci.*, 2017, **4**, 1600453.
14 J. S. Hummelshøj, J. Blomqvist, S. Datta, T. Vegge, J. Rossmeisl, K. S. Thygesen, A. C. Luntz, K. W. Jacobsen and J. K. Nørskov, *J. Chem. Phys.*, 2010, **132**, 071101.
15 S. P. Ong, Y. Mo and G. Ceder, *Phys. Rev. B: Condens. Matter Mater. Phys.*, 2012, **85**, 081105(R).
16 J. M. Garcia-Lastra, J. D. Bass and K. S. Thygesen, *J. Chem. Phys.*, 2011, **135**, 121101.
17 K. C. Lau and L. A. Curtiss, *J. Phys. Chem. C*, 2011, **115**, 23625–23633.
18 A. R. Oganov and C. W. Glass, *J. Chem. Phys.*, 2006, **124**, 244704.
19 C. W. Glass, A. R. Oganov and N. Hansen, *Comput. Phys. Commun.*, 2006, **175**, 713–720.
20 G. Kresse and J. Furthmüller, *Phys. Rev. B: Condens. Matter Mater. Phys.*, 1996, **54**, 11169.
21 G. Kresse and J. Furthmüller, *Comput. Mater. Sci.*, 1996, **6**, 15–50.
22 S. J. Clark, M. D. Segall, C. J. Pickard, P. J. Hasnip, M. I. J. Probert, K. Refson and M. C. Payne, *Z. Kristallogr.*, 2005, **220**, 567–570.
23 B. G. Pfrommer, M. Côté, S. G. Louie and M. L. Cohen, *J. Comput. Phys.*, 1997, **131**, 233–240.
24 J. P. Perdew, K. Burke and M. Ernzerhof, *Phys. Rev. Lett.*, 1996, **77**, 3865.
25 D. Vanderbilt, *Phys. Rev. B: Condens. Matter Mater. Phys.*, 1990, **41**, 7892(R).
26 J. Heyd, G. E. Scuseria and M. Ernzehof, *J. Chem. Phys.*, 2003, **118**, 8207.
27 F. Birch, *Phys. Rev.*, 1947, **71**, 809–824.
28 A. Togo and I. Tanaka, *Scr. Mater.*, 2015, **108**, 1–5.
29 K. Momma and F. Izumi, *J. Appl. Crystallogr.*, 2011, **44**, 1272–1276.
30 H. Wu, H. Zhang, X. Cheng and L. Cai, *Philos. Mag.*, 2007, **87**, 3373–3383.
31 K. C. Lau, D. Qiu, X. Luo, J. Greeley, L. A. Curtiss, J. Lu and K. Amine, *Energies*, 2015, **8**, 529–548.
32 M. D. Radin, F. Tian and D. J. Siegel, *J. Mater. Sci.*, 2012, **47**, 7564–7570.
33 M. D. Segall, C. J. Pickard, R. Shah and M. C. Payne, *Mol. Phys.*, 1996, **89**, 571–577.
34 M. D. Segall, R. Shah, C. J. Pickard and M. C. Payne, *Phys. Rev. B: Condens. Matter Mater. Phys.*, 1996, **54**, 16317.
35 A. D. Becke and K. E. Edgecombe, *J. Chem. Phys.*, 1990, **92**, 5397–5403.
36 A. Savin, O. Jepsen, J. Flad, O. K. Andersen, H. Preuss and H. G. von Schnering, *Angew. Chem., Int. Ed.*, 1992, **31**, 187–188.
37 http://www.tcm.phy.cam.ac.uk/castep/documentation/WebHelp/content/modules/castep/thcastepelf.htm, online; accessed 20-September-2017.
38 G. de la Flor, D. Orobengoa, E. Tasci, J. M. Perez-Mato and M. I. Aroyo, *J. Appl. Crystallogr.*, 2016, **49**, 653–664.
39 J. Kang, Y. S. Jung, S. H. Wei and A. C. Dillon, *Phys. Rev. B: Condens. Matter Mater. Phys.*, 2012, **85**, 035210.

Electronic Supplementary Information (ESI):

Theoretical aspects in structural distortion and the electronic properties of lithium peroxide under high pressure

Pornmongkol Jimlim,[ab] Komsilp Kotmool,[b] Udomsilp Pinsook,[ac]
Suttichai Assabumrungrat,[d] Rajeev Ahujak,[ef] and Thiti Bovornratanaraks*[ac]

[a] *Extreme Conditions Physics Research Laboratory (ECPRL), Physics of Energy Materials Research Unit, Department of Physics, Faculty of Science, Chulalongkorn University, Bangkok 10330, Thailand*
[b] *Department of Physics, Mahidol Wittayanusorn School, Nakhon Pathom 73170, Thailand*
[c] *Thailand Center of Excellence in Physics, Commission on Higher Education, Bangkok 10400, Thailand*
[d] *Center of Excellence on Catalysis and Catalytic Reaction Engineering, Department of Chemical Engineering, Chulalongkorn University, Bangkok 10330, Thailand*
[e] *Condensed Matter Theory Group, Department of Physics and Astronomy, Box 516, Uppsala University, S-75120 Uppsala, Sweden*
[f] *Applied Materials Physics, Department of Materials and Engineering, Royal Institute of Technology (KTH), S-100 44 Stockholm, Sweden*

E-mail: thiti.b@chula.ac.th
Phone: +66 (0)22187554. Fax: +66 (0)22531150

Table S1. Structural parameters of Li_2O_2 for the $P6_3/mmc$, $P2_1$, $P2_1/c$, and $P2_1/c$† structures at the different pressures.

Pressure (GPa)	Structure	Lattice parameter ($P6_3/mmc$: a = b ≠ c, α = β = 90⁰, γ = 120⁰) ($P2_1$, $P2_1$/c : a ≠ b ≠ c, α = γ = 90⁰, β ≠ 90⁰)				Atom	Site	Atomic coordinates		
		a (Å)	b (Å)	c (Å)	β (degree)			x	y	z
0	$P6_3/mmc$	3.1858	3.1858	7.7182	90.0000	Li(1)	2a	0.00000	0.00000	0.00000
						Li(2)	2c	0.33333	0.66667	0.25000
						O(1)	4f	0.33333	0.66667	0.64950
10	$P6_3/mmc$	3.0767	3.0767	7.4208	90.0000	Li(1)	2a	0.00000	0.00000	0.00000
						Li(2)	2c	0.33333	0.66667	0.25000
						O(1)	4f	0.33333	0.66667	0.64645
11	$P6_3/mmc$	3.0694	3.0694	7.3780	90.0000	Li(1)	2a	0.00000	0.00000	0.00000
						Li(2)	2c	0.33333	0.66667	0.25000
						O(1)	4f	0.33333	0.66667	0.64568
39	$P6_3/mmc$	2.9020	2.9020	6.9536	90.0000	Li(1)	2a	0.00000	0.00000	0.00000
						Li(2)	2c	0.33333	0.66667	0.25000
						O(1)	4f	0.33333	0.66667	0.64135
40	$P6_3/mmc$	2.8987	2.8987	6.9332	90.0000	Li(1)	2a	0.00000	0.00000	0.00000
						Li(2)	2c	0.33333	0.66667	0.25000
						O(1)	4f	0.33333	0.66667	0.64091
75	$P6_3/mmc$	2.7781	2.7781	6.6468	90.0000	Li(1)	2a	0.00000	0.00000	0.00000
						Li(2)	2c	0.33333	0.66667	0.25000
						O(1)	4f	0.33333	0.66667	0.63816
75	$P2_1$	2.5695	2.5942	6.4767	91.8505	Li(1)	2a	0.84403	0.72368	0.11400
						Li(2)	2a	0.65603	0.51017	0.38600
						O(1)	2a	0.34300	0.21666	0.15252
						O(2)	2a	0.15705	0.01719	0.34747
75	$P2_1/c$	2.5695	2.5941	7.0454	113.2454	Li	4e	0.45790	0.89333	-0.13599
						O	4e	-0.00463	0.40036	-0.09748
75	$P2_1/c$†	6.4771	2.5941	6.8903	158.1169	Li	4e	0.72995	0.60668	0.09399
						O	4e	0.19042	1.09963	-0.40707
136	$P2_1$	2.4424	2.4876	6.1569	89.7118	Li(1)	2a	0.85698	0.72372	0.11396
						Li(2)	2a	0.64303	0.51011	0.38604
						O(1)	2a	0.35399	0.22011	0.14973
						O(2)	2a	0.14603	0.01376	0.35026
136	$P2_1/c$	2.4423	2.4877	6.6119	111.3833	Li	4e	0.47094	0.89325	-0.13607
						O	4e	0.00379	0.39687	-0.10025
136	$P2_1/c$†	6.1570	2.4877	6.6353	158.4040	Li	4e	0.74306	0.60677	0.10702
						O	4e	0.20427	1.10314	-0.39600
150	$P2_1$	2.4197	2.4701	6.1009	89.2687	Li(1)	2a	0.85965	0.72409	0.11390
						Li(2)	2a	0.64037	0.50973	0.38611
						O(1)	2a	0.35608	0.22093	0.14924
						O(2)	2a	0.14394	0.01296	0.35076
150	$P2_1/c$	2.4194	2.4703	6.5333	110.9788	Li	4e	0.47361	0.89276	-0.13616
						O	4e	0.00547	0.39595	-0.10074
150	$P2_1/c$ (similar)‖	6.1008	2.4703	6.5333	158.2667	Li	4e	0.52639	0.60724	0.89023
						O	4e	0.99453	0.10405	0.39379
150	$P2_1/c$†	6.1009	2.4703	6.5926	158.4716	Li	4e	0.74587	0.60726	0.10975
						O	4e	0.20690	1.10404	-0.39386
300	$P2_1/c$	2.2464	2.3473	5.9562	107.5213	Li	4e	0.49472	0.88747	-0.13824
						O	4e	0.01976	0.38790	-0.10386
500	$P2_1/c$	2.1174	2.2416	5.5723	105.4396	Li	4e	0.49349	0.61747	1.14122
						O	4e	0.96991	0.11908	1.10491

†Reference 10

‖Structural parameters obtained by using COMPSTRU programme proposed by Flor *et al*[38].

Table S2. Mulliken charges of the Li and O atoms for the $P6_3/mmc$, $P2_1$, and $P2_1/c$ structures of Li_2O_2 at the different pressures. The charge spilling parameters for the $P6_3/mmc$, $P2_1$, and $P2_1/c$ structures are in the ranges of 0.80-0.83 %, 0.85-0.88 %, and 0.89-1.06 %, respectively. The effective ionic valences is calculated by using the difference between the formal ionic charge and the Mulliken charge on the anion species in the crystal proposed by Segall *et al.* [34]

Pressure (GPa)	Structure	Mulliken charge (*e*)								Effective ionic * valences ($\|e\|$)
		Li(1)	Li(2)	Li(3)	Li(4)	O(1)	O(2)	O(3)	O(4)	
0	$P6_3/mmc$	0.99	0.99	0.77	0.77	-0.88	-0.88	-0.88	-0.88	0.12
0†	$P6_3/mmc$†	0.99	0.99	0.77	0.77	-0.88	-0.88	-0.88	-0.88	0.12
4	$P6_3/mmc$	1.00	1.00	0.77	0.77	-0.88	-0.88	-0.88	-0.88	0.12
6	$P6_3/mmc$	1.00	1.00	0.77	0.77	-0.88	-0.88	-0.88	-0.88	0.12
8	$P6_3/mmc$	1.01	1.01	0.77	0.77	-0.89	-0.89	-0.89	-0.89	0.11
10	$P6_3/mmc$	1.01	1.01	0.77	0.77	-0.89	-0.89	-0.89	-0.89	0.11
11	$P6_3/mmc$	1.01	1.01	0.77	0.77	-0.89	-0.89	-0.89	-0.89	0.11
12	$P6_3/mmc$	1.02	1.02	0.77	0.77	-0.89	-0.89	-0.89	-0.89	0.11
15	$P6_3/mmc$	1.02	1.02	0.77	0.77	-0.89	-0.89	-0.89	-0.89	0.11
20	$P6_3/mmc$	1.03	1.03	0.77	0.77	-0.90	-0.90	-0.90	-0.90	0.10
25	$P6_3/mmc$	1.04	1.04	0.76	0.76	-0.90	-0.90	-0.90	-0.90	0.10
30	$P6_3/mmc$	1.05	1.05	0.76	0.76	-0.91	-0.91	-0.91	-0.91	0.09
35	$P6_3/mmc$	1.06	1.06	0.76	0.76	-0.91	-0.91	-0.91	-0.91	0.09
39	$P6_3/mmc$	1.06	1.06	0.76	0.76	-0.91	-0.91	-0.91	-0.91	0.09
40	$P6_3/mmc$	1.06	1.06	0.76	0.76	-0.91	-0.91	-0.91	-0.91	0.09
41	$P6_3/mmc$	1.07	1.07	0.76	0.76	-0.91	-0.91	-0.91	-0.91	0.09
45	$P6_3/mmc$	1.07	1.07	0.76	0.76	-0.92	-0.92	-0.92	-0.92	0.08
50	$P6_3/mmc$	1.08	1.08	0.76	0.76	-0.92	-0.92	-0.92	-0.92	0.08
55	$P6_3/mmc$	1.08	1.08	0.76	0.76	-0.92	-0.92	-0.92	-0.92	0.08
60	$P6_3/mmc$	1.09	1.09	0.76	0.76	-0.92	-0.92	-0.92	-0.92	0.08
65	$P6_3/mmc$	1.10	1.10	0.76	0.76	-0.93	-0.93	-0.93	-0.93	0.07
70	$P6_3/mmc$	1.10	1.10	0.75	0.75	-0.93	-0.93	-0.93	-0.93	0.07
75	$P6_3/mmc$	1.11	1.11	0.75	0.75	-0.93	-0.93	-0.93	-0.93	0.07
75	$P2_1$	0.90	0.90	0.90	0.90	-0.90	-0.90	-0.90	-0.90	0.10
135	$P2_1$	0.92	0.92	0.92	0.92	-0.92	-0.92	-0.92	-0.92	0.08
136	$P2_1/c$	0.92	0.92	0.92	0.92	-0.92	-0.92	-0.92	-0.92	0.08
150	$P2_1/c$	0.92	0.92	0.92	0.92	-0.92	-0.92	-0.92	-0.92	0.08
300	$P2_1/c$	0.94	0.94	0.94	0.94	-0.94	-0.94	-0.94	-0.94	0.06
500	$P2_1/c$	0.95	0.95	0.95	0.95	-0.95	-0.95	-0.95	-0.95	0.05

†Reference 10

*Reference 34

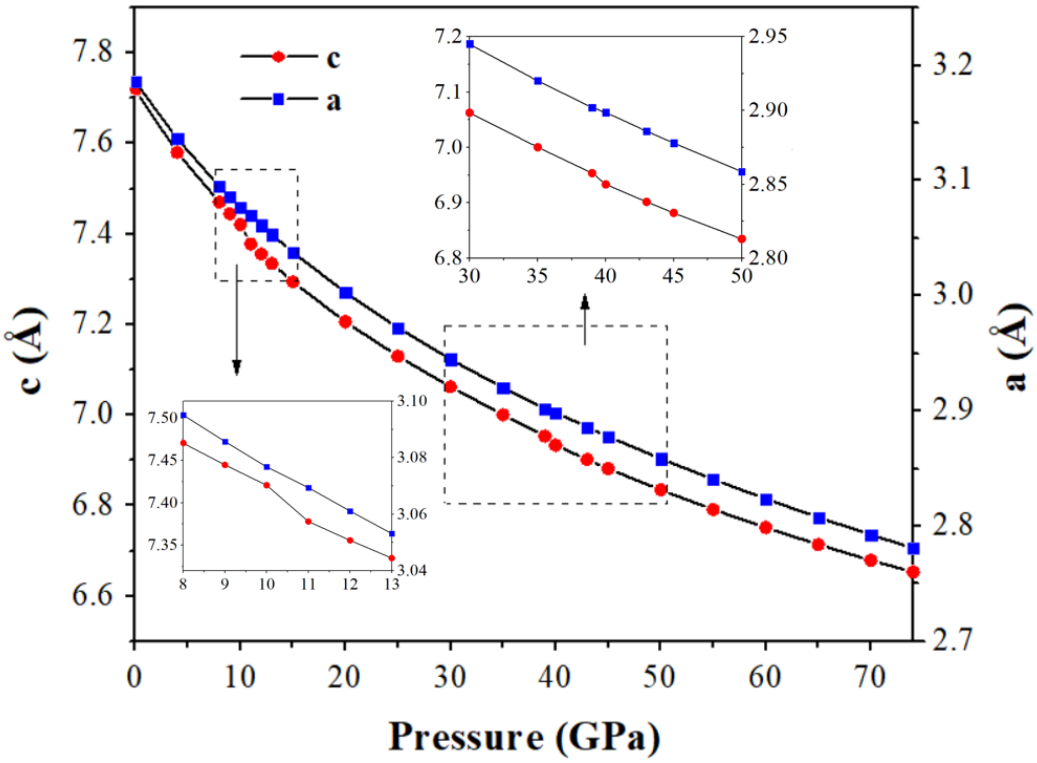

Figure S1. Plot of the lattice constants (*a* and *c*) *versus* pressure (0-74 GPa). Insets represent the enlargement in the rectangular dashed lines.

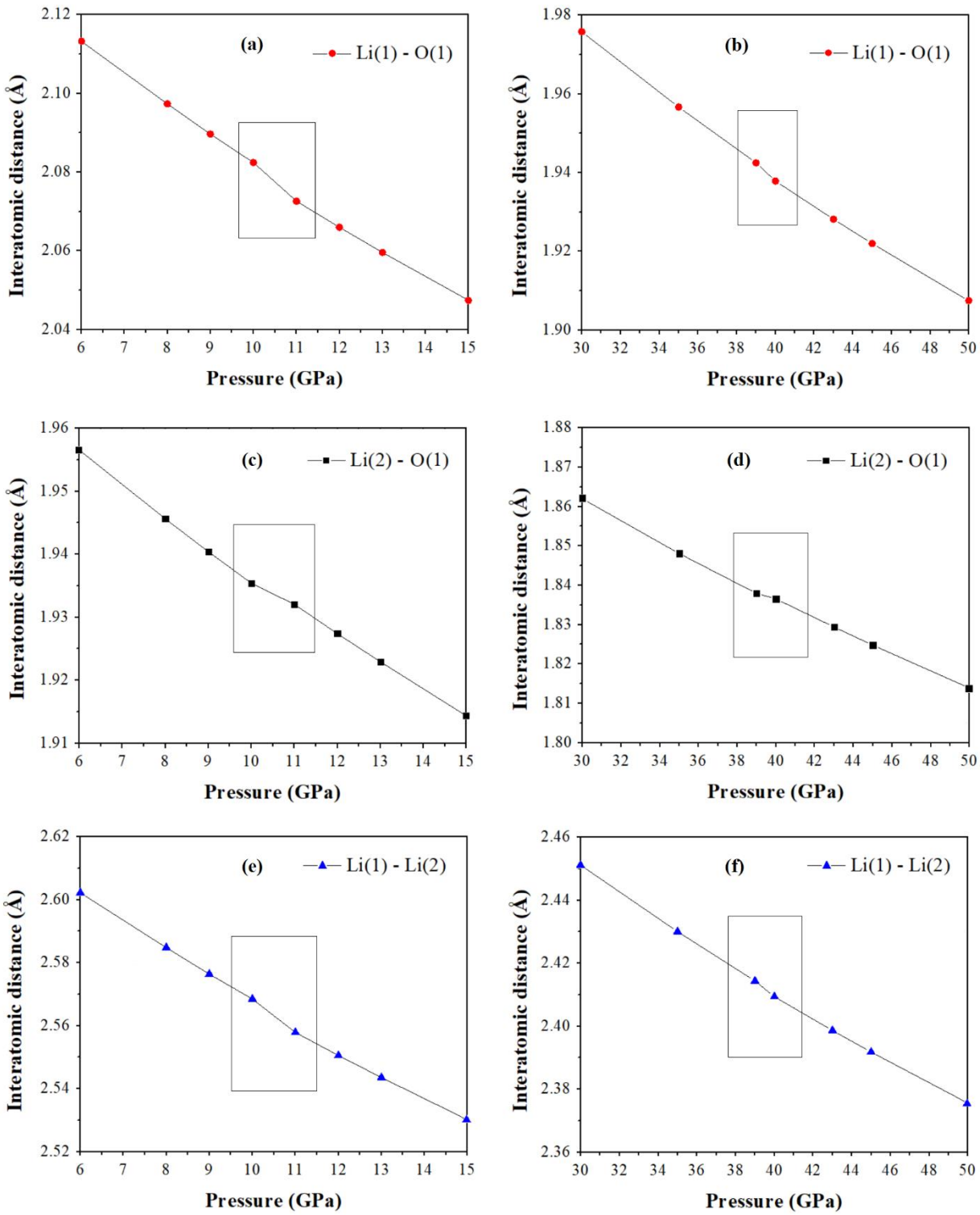

Figure S2. (a)-(b), (c)-(d), and (e)-(f) represent the interatomic distances of the Li(1)-O(1), Li(2)-O(1), and Li(1)-Li(2) in the pressure ranges of 6-15 GPa and 30-50 GPa, respectively. The rectangular solid lines mark the abnormal change of the interatomic distances in the pressure ranges of 10-11 GPa and 39-40 GPa.

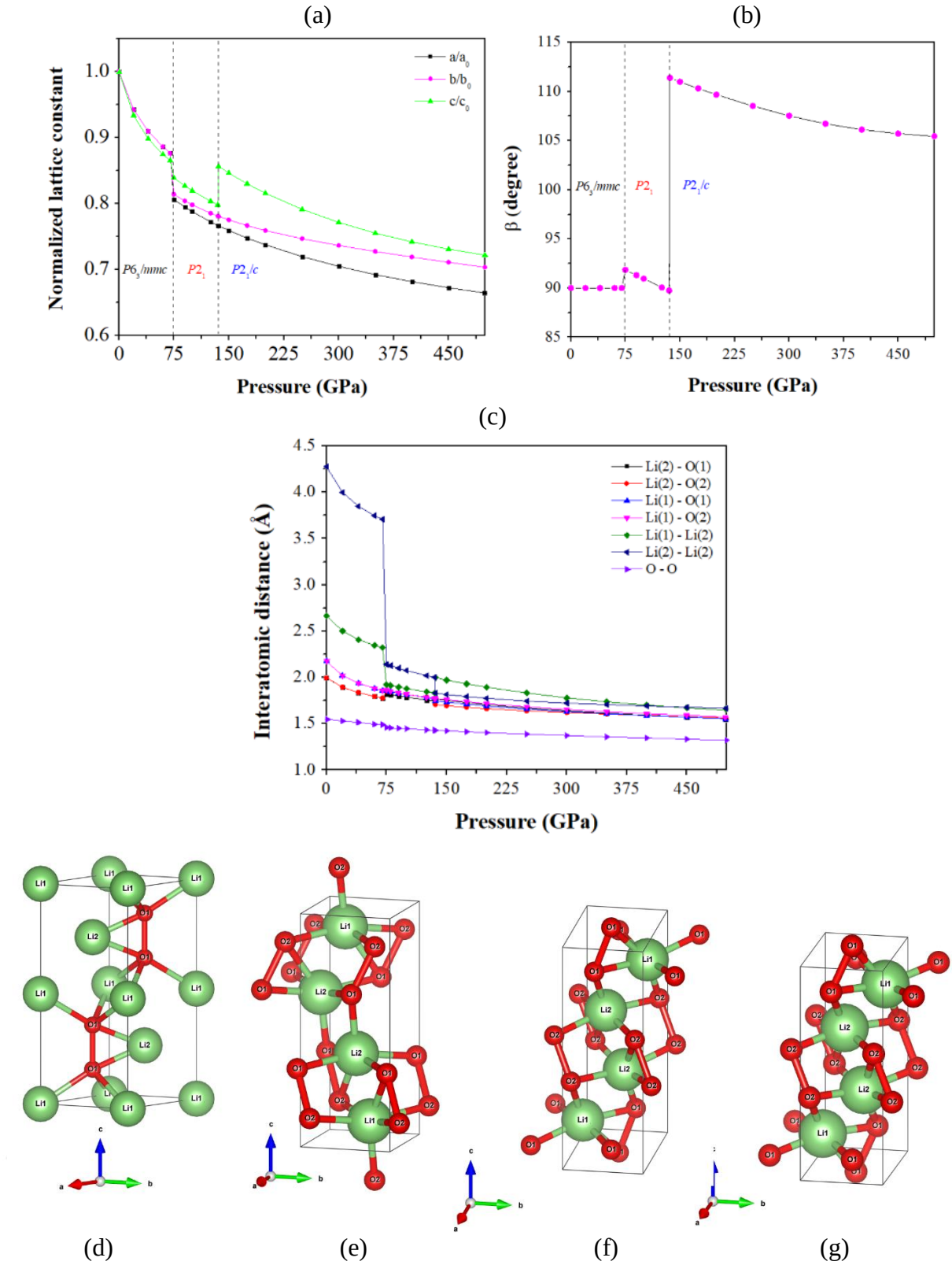

Figure S3. (a) Plot of the normalized lattice constants *versus* pressure, (b) Plot of the β *versus* pressure, (c) Plot of the interatomic distance *versus* pressure, (d) the $P6_3/mmc$ structure at 0 GPa, (e) the $P2_1$ structure at 75 GPa, (f) the $P2_1/c$ structure at 150 GPa, and (g) the $P2_1/c$ structure at 500 GPa.

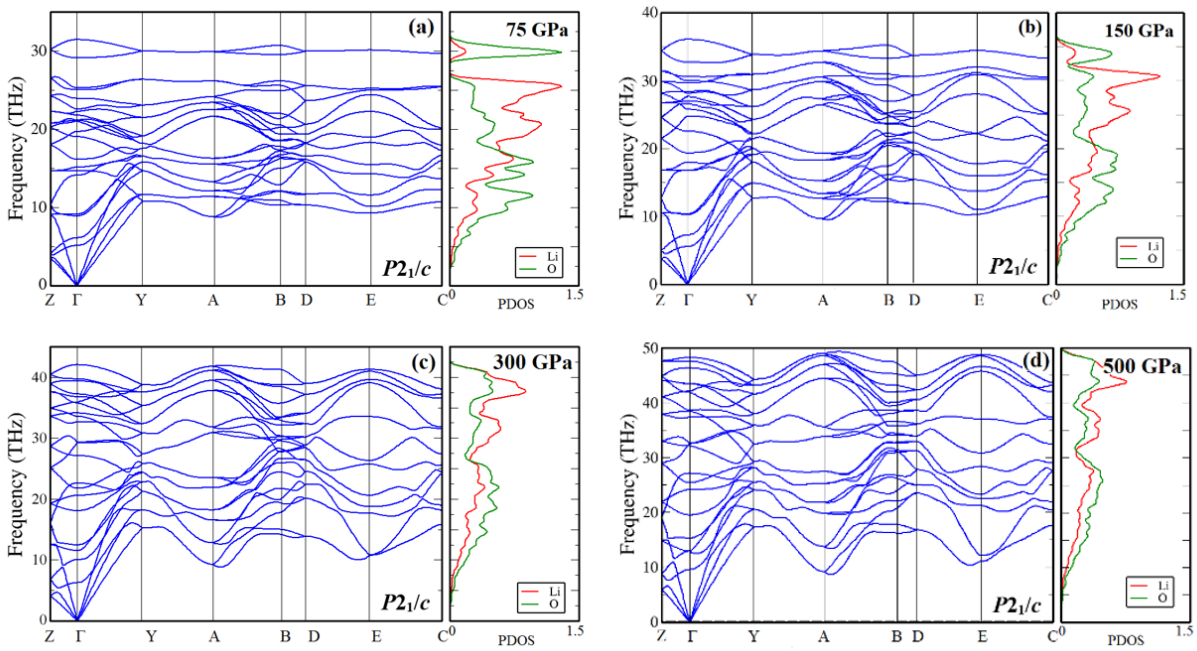

Figure S4. Phonon dispersion curves and partial phonon density of states (PDOSs) for the $P2_1/c$ structure at pressures of: (a)-(d) 75, 150, 300, and 500 GPa, respectively.

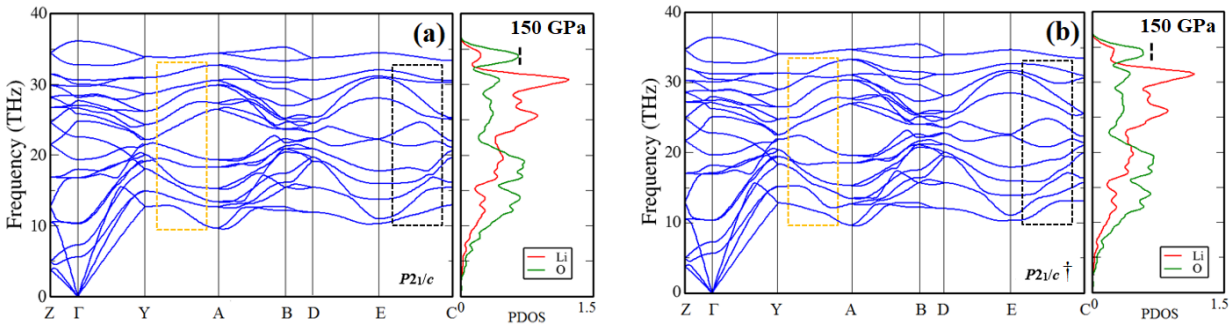

Figure S5. Phonon dispersion curves and partial phonon density of states (PDOSs) for two structures of Li_2O_2 at 150 GPa: (a) the $P2_1/c$ structure, and (b) the $P2_1/c^{\dagger}$ structure. The yellow and black rectangular dashed lines represent the differences between the $P2_1/c$ and $P2_1/c^{\dagger}$ structure in the Y-A and E-C paths, respectively. The vertical dashed lines mark the peak of the highest frequency phonon modes in the $P2_1/c$ structures.

Figure S6. Partial density of states (PDOSs) of Li and O for the $P6_3/mmc$ structure at 5, 8, 11, 14, 38, 39, 40, and 41 GPa: (a)-(e) for the s-states of Li, (f)-(j) for the s-states of O, and (k)-(r) for the p-states of O. The arrows represent the trends of changes with increasing pressure. The vertical dashed lines represent the Fermi level.

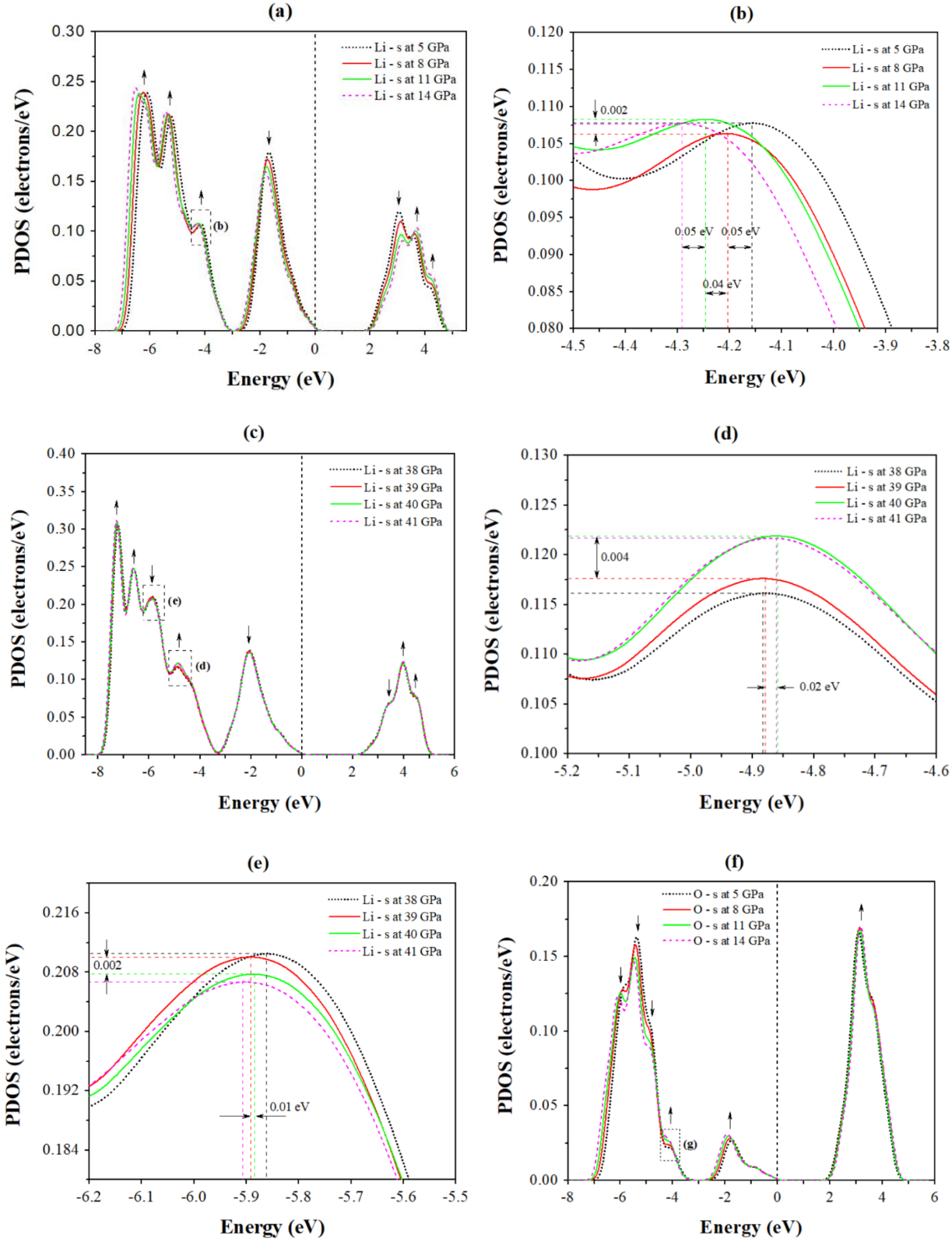

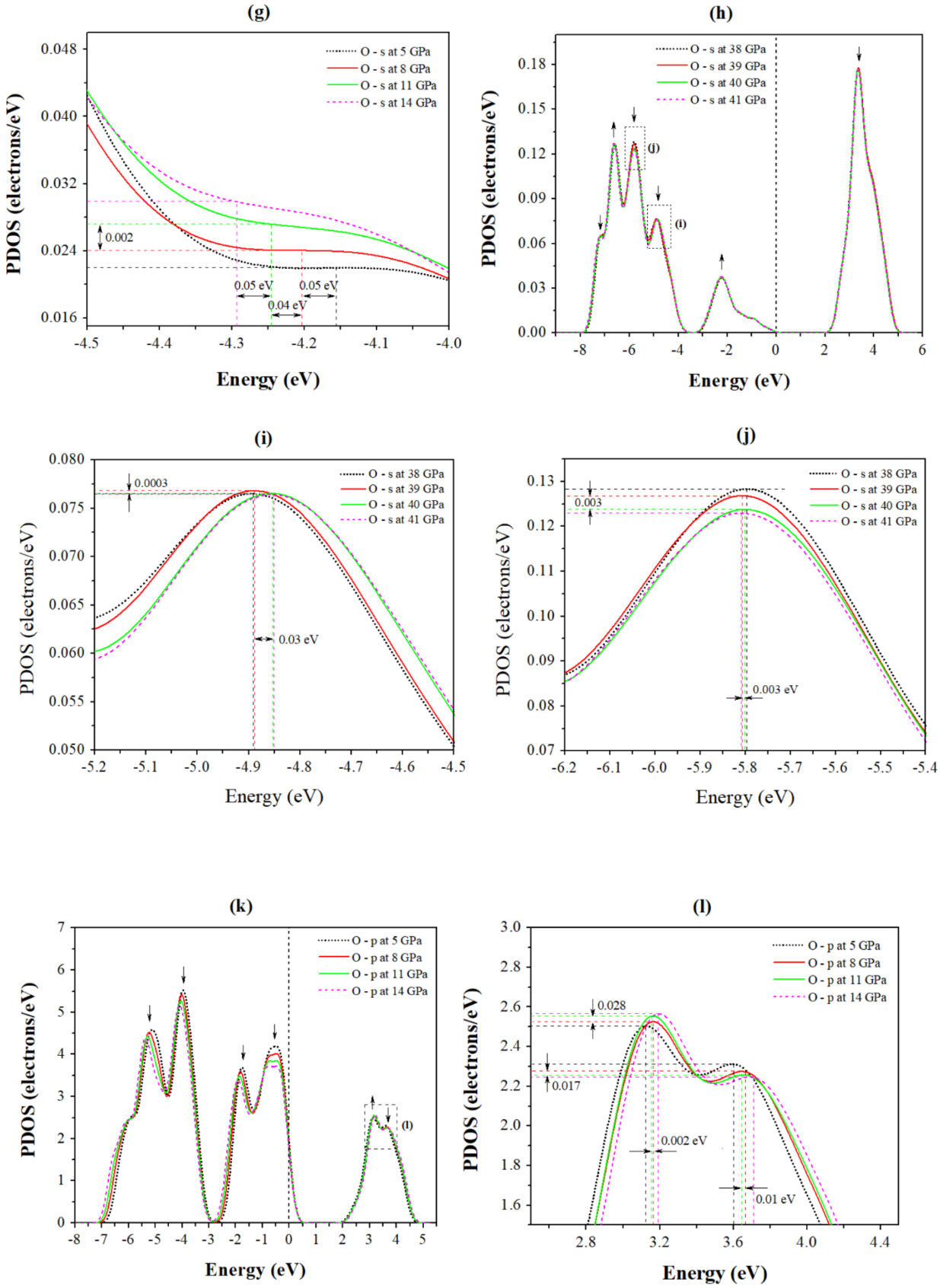
(g)
O - s at 5 GPa
O - s at 8 GPa
O - s at 11 GPa
O - s at 14 GPa
0.002
0.05 eV
0.05 eV
0.04 eV
PDOS (electrons/eV)
Energy (eV)
(h)
O - s at 38 GPa
O - s at 39 GPa
O - s at 40 GPa
O - s at 41 GPa
(j)
(i)
PDOS (electrons/eV)
Energy (eV)
(i)
O - s at 38 GPa
O - s at 39 GPa
O - s at 40 GPa
O - s at 41 GPa
0.0003
0.03 eV
PDOS (electrons/eV)
Energy (eV)
(j)
O - s at 38 GPa
O - s at 39 GPa
O - s at 40 GPa
O - s at 41 GPa
0.003
0.003 eV
PDOS (electrons/eV)
Energy (eV)
(k)
O - p at 5 GPa
O - p at 8 GPa
O - p at 11 GPa
O - p at 14 GPa
(l)
PDOS (electrons/eV)
Energy (eV)
(l)
O - p at 5 GPa
O - p at 8 GPa
O - p at 11 GPa
O - p at 14 GPa
0.028
0.017
0.002 eV
0.01 eV
PDOS (electrons/eV)
Energy (eV)

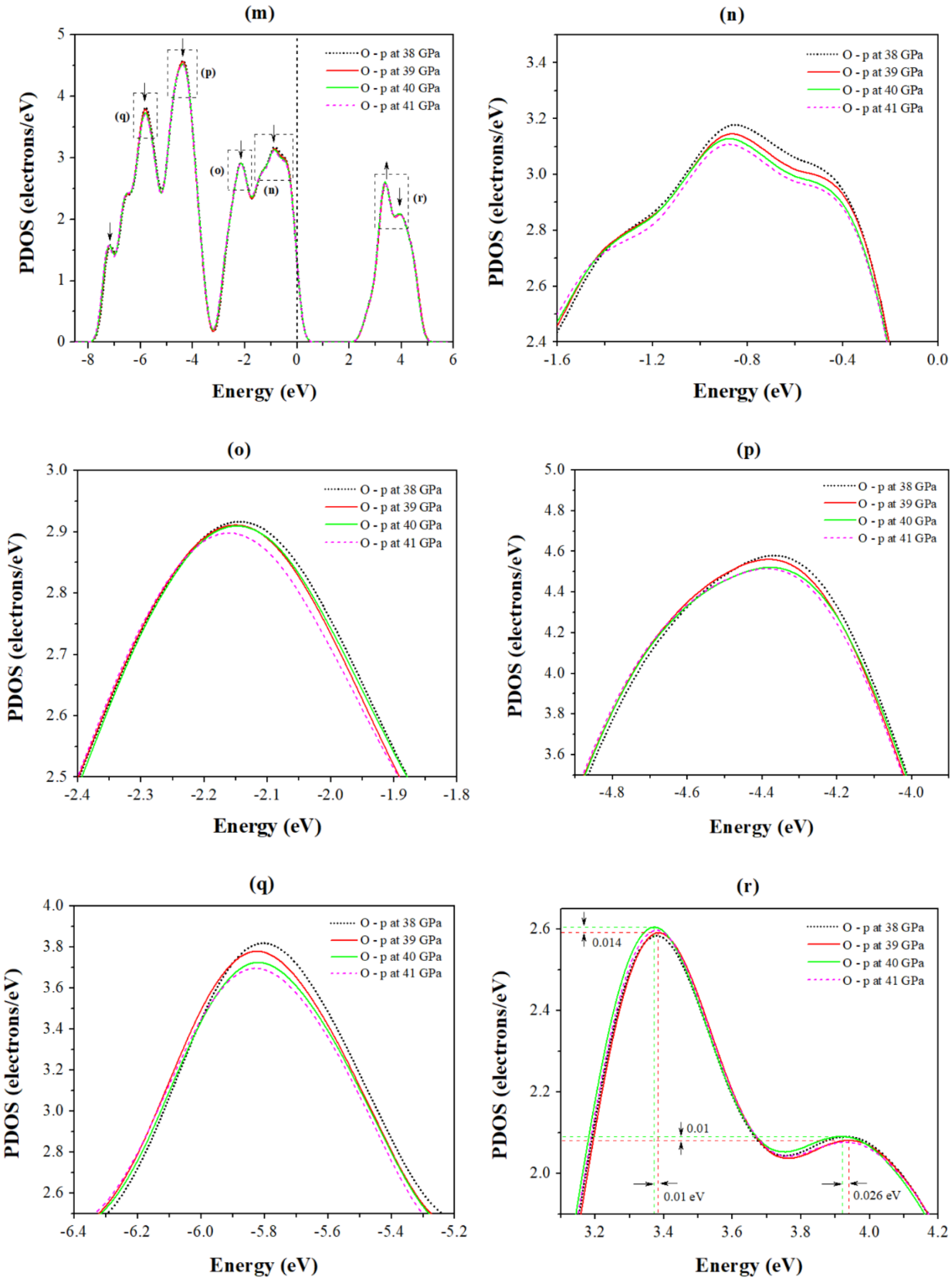
(m)
(n)
(o)
(p)
(q)
(r)
O - p at 38 GPa
O - p at 39 GPa
O - p at 40 GPa
O - p at 41 GPa
PDOS (electrons/eV)
Energy (eV)
0.014
0.01
0.01 eV
0.026 eV

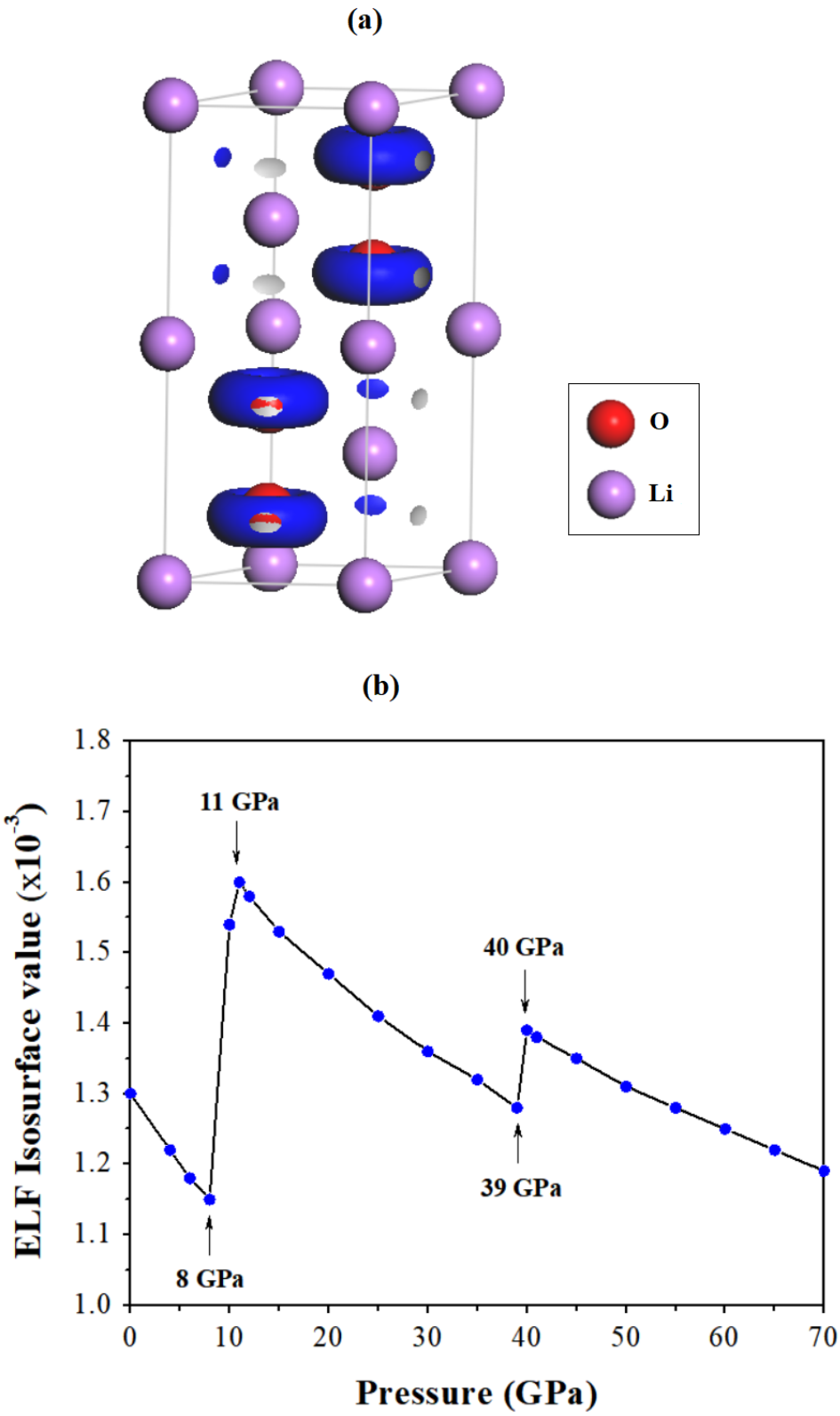

Figure S7. (a) Isosurface of the electron localization functions (ELF) in the $P6_3/mmc$ structure at 40 GPa. (b) Plot of the ELF isosurface value for the $P6_3/mmc$ structure in the pressure range of 0-70 GPa.

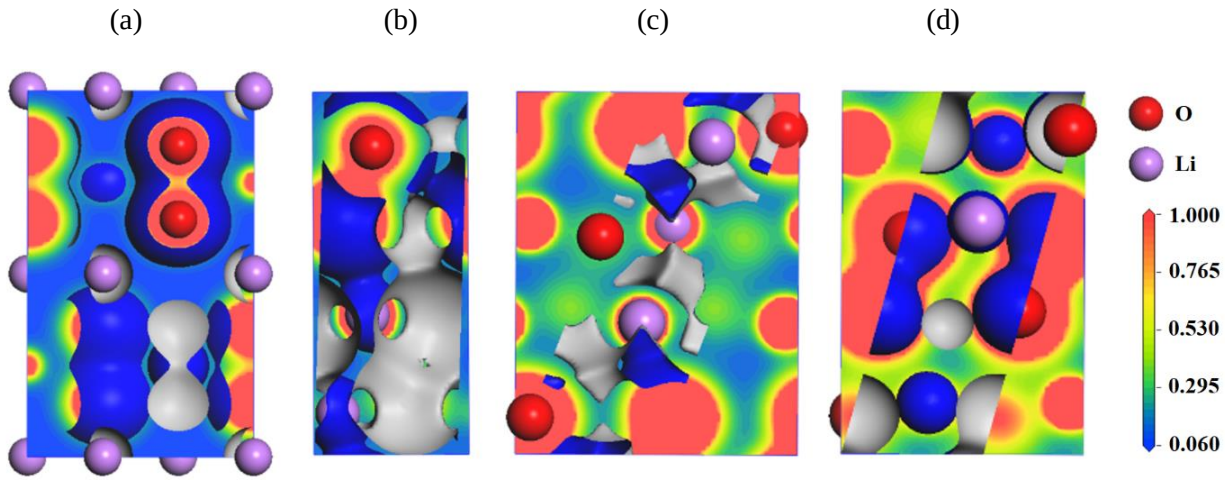

Figure S8. Electron density maps of various structures of Li_2O_2 projected onto (020) plane of: (a) the $P6_3/mmc$ structure at 0 GPa, (b) the $P2_1$ structure at 75 GPa, (c)-(d) the $P2_1/c$ structure at 150 and 500 GPa, respectively. The electron density isosurfaces values of 0.200 for (a, b, c) and 1.412 for (d).

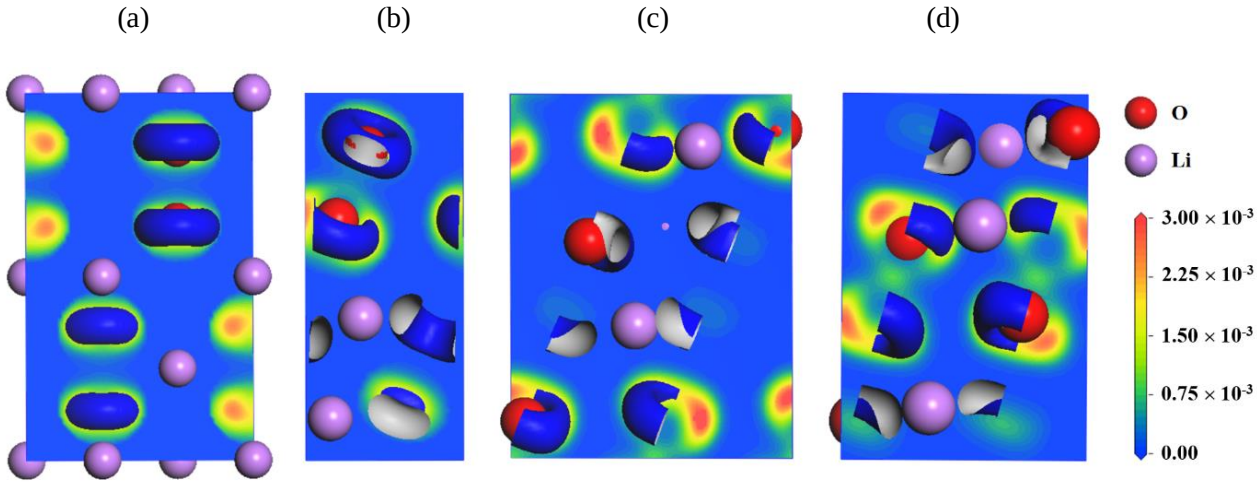

Figure S9. ELFs for various structures of Li_2O_2 projected onto (020) plane of: (a) the $P6_3/mmc$ structure at 0 GPa, (b) the $P2_1$ structure at 75 GPa, (c)-(d) the $P2_1/c$ structure at 150 and 500 GPa, respectively. The ELF isosurface values of 0.001 for (a) and 0.002 for (b, c, d).

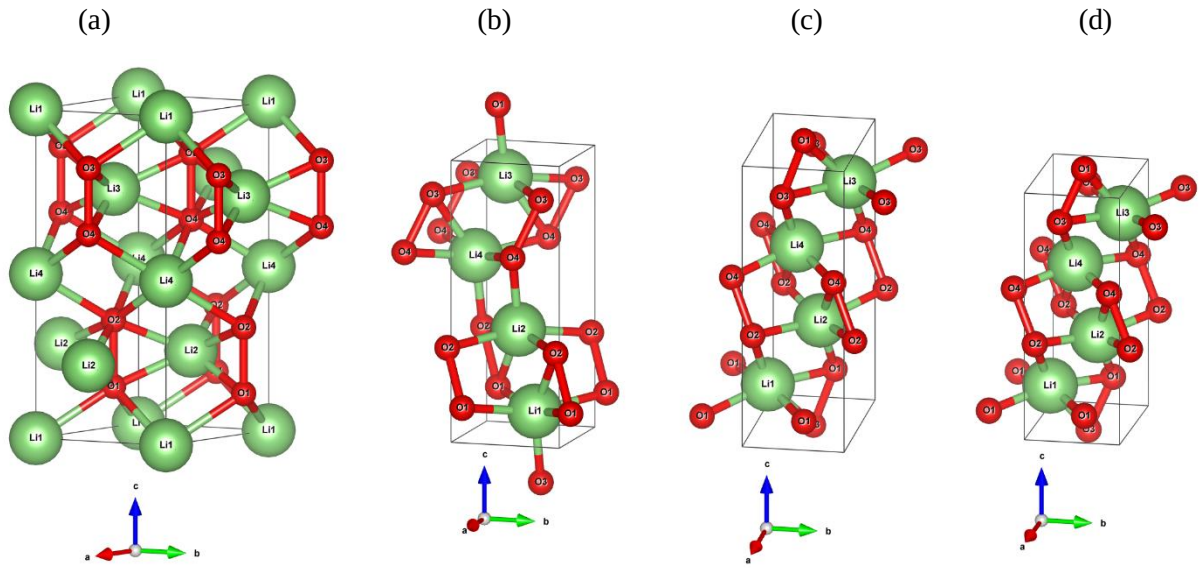

Figure S10. Crystal structures of Li_2O_2 for three phases at the different pressures: (a) the $P6_3/mmc$ structure at 0 GPa, (b) the $P2_1$ structure at 75 GPa, (c)-(d) the $P2_1/c$ structure at 150 and 500 GPa, respectively.